INFORMATION TO USERS

This manuscript has been reproduced from the microfilm master. UMI films the text directly from the original or copy submitted. Thus, some thesis and dissertation copies are in typewriter face, while others may be from any type of computer printer.

The quality of this reproduction is dependent upon the quality of the copy submitted. Broken or indistinct print, colored or poor quality illustrations and photographs, print bleedthrough, substandard margins, and improper alignment can adversely affect reproduction.

In the unlikely event that the author did not send UMI a complete manuscript and there are missing pages, these will be noted. Also, if unauthorized copyright material had to be removed, a note will indicate the deletion.

Oversize materials (e.g., maps, drawings, charts) are reproduced by sectioning the original, beginning at the upper left-hand corner and continuing from left to right in equal sections with small overlaps.

ProQuest Information and Learning
300 North Zeeb Road, Ann Arbor, MI 48106-1346 USA
800-521-0600

Measurement of Inclusive Production of Charmonium States at *BABAR*

Marko Milek

Department of Physics

McGill University, Montréal

March 2001

A Thesis submitted to the

Faculty of Graduate Studies and Research

in partial fulfillment of the requirements for the degree

Doctor of Philosophy

Abstract

This thesis presents a study of inclusive production of charmonium mesons at the $\Upsilon(4S)$ resonance ($\sqrt{s} = 10.58$ GeV) and in the continuum up to 50 MeV below the resonance. The full dataset of *BABAR* Run 1 (an integrated luminosity of 23.3 fb^{-1}) is used in the analysis.

The branching fractions of B mesons to J/ψ, $\psi(2S)$, χ_{c1} and χ_{c2} are measured: $\mathcal{B}_{B\to J/\psi X} = (1.044 \pm 0.013 \pm 0.035)\%$, $\mathcal{B}_{B\to\psi(2S)X} = (0.274 \pm 0.020 \pm 0.029)\%$, $\mathcal{B}_{B\to\chi_{c1}X} = (0.378 \pm 0.034 \pm 0.026)\%$ and $\mathcal{B}_{B\to\chi_{c2}X} < 0.21\%$. By equating the $\psi(2S)$ production rates calculated using the $\psi(2S) \to \ell^+\ell^-$ final state to those using $\psi(2S) \to \pi^+\pi^- J/\psi$, we obtain competitive measurements of the $\psi(2S) \to \ell^+\ell^-$ branching fractions: $\mathcal{B}_{\psi(2S)\to e^+e^-} = (0.815 \pm 0.090 \pm 0.090)\%$ and $\mathcal{B}_{\psi(2S)\to\mu^+\mu^-} = (0.700 \pm 0.083 \pm 0.093)\%$. The cross-section for J/ψ production in e^+e^- annihilation in the continuum is measured to be: $\sigma_{e^+e^-\to J/\psi X} = (2.47 \pm 0.21 \pm 0.20)$ pb. This cross-section excludes J/ψ mesons from B decays, two-photon or initial state radiation processes. An upper limit on the inclusive non-$B\overline{B}$ J/ψ decays of the $\Upsilon(4S)$ is set at $\mathcal{B}_{\Upsilon(4S)\to J/\psi X} < 5.1 \times 10^{-4}$, for J/ψ with the center of mass momentum above 2 GeV/c. The helicity, the center of mass production angle distribution and the center of mass momentum distribution of the reconstructed J/ψ mesons are presented.

Résumé

Cette thèse présente une étude de la production inclusive de mesons 'charmonium' à la résonance $\Upsilon(4S)$ ($\sqrt{s} = 10.58$ GeV) et dans le 'continuum' jusqu'á 50 MeV sous la résonance. Les données de la 'Run 1' de *BABAR* (une luminosité integrée de 23.3 fb^{-1}) sont utilisées pour cette analyse.

Les taux de branchement de meson B à J/ψ, $\psi(2S)$, χ_{c1} et χ_{c2} sont mesurés: $\mathcal{B}_{B\to J/\psi X} = (1.044 \pm 0.013 \pm 0.035)\%$, $\mathcal{B}_{B\to\psi(2S)X} = (0.274 \pm 0.020 \pm 0.029)\%$,

$\mathcal{B}_{B\to\chi_{c1}X} = (0.378 \pm 0.034 \pm 0.026)\%$ et $\mathcal{B}_{B\to\chi_{c2}X} < 0.21\%$. En égolisont les taux de productions de $\psi(2S)$ calculés avec l'état final de $\psi(2S)\to\ell^+\ell^-$aux taux calculés en utilisant la reaction $\psi(2S) \to \pi^+\pi^- J/\psi$, nous obtenons une mesure compétitive des taux de branchements: $\mathcal{B}_{\psi(2S)\to e^+e^-} = (0.815 \pm 0.090 \pm 0.090)\%$ et $\mathcal{B}_{\psi(2S)\to\mu^+\mu^-} = (0.700 \pm 0.083 \pm 0.093)\%$. La section efficace de production de particules J/ψ dans l'annihilation e^+e^- dans le 'continuum' est mesurée: $\sigma_{e^+e^-\to J/\psi X} =$ $(2.47 \pm 0.21 \pm 0.20)$ pb. Cette section efficace exclut les mesons J/ψ qui parviennent de la désintégration de mesons B, d'états á deux photons ou de processus de rayonnement de photon initial. Une limite supérieure sur la chaine de désintégration inclusive de la résonance $\Upsilon(4S)$ à J/ψ, en excluant les états $B\overline{B}$ intermédiats, est placée à $\mathcal{B}_{\Upsilon(4S)\to J/\psi X} < 5.1 \times 10^{-4}$, pour les J/ψ avec impulsion du centre de masse sur 2 GeV/c. L'hélicité, la distribution d'angle de production au centre de masse, et la distribution d'impulsion au centre de masse, des mesons J/ψ reconstruits sont présentées.

Contents

List of Figures

List of Tables

Acknowledgements

I would like to express my deepest gratitude to my supervisor, Popat Patel, for his help in finding a suitable research project and with the production of this thesis, to Chris Hearty of University of British Columbia, my collaborator on the inclusive Charmonium analysis, and to Riccardo Faccini, the coordinator of *BABAR* Charmonium group. Without their generous help this thesis would not be the same.

I am grateful for the efforts of all people involved in the *BABAR* experiment, as well as for the contributions of our PEP-II colleagues, in achieving the excellent conditions that have made this work possible. I would also like to thank SLAC for the support and kind hospitality.

This research was partially funded by the Natural Sciences and Engineering Research Council (NSERC) and by the Alexander McFee Foundation.

My friends: Miljana, Vladimir, Marko, my office mates: Claude, Kostas, Tiago, Declan, and colleagues from around the world, thank you for your love, help and constant encouragement.

Finally, my deepest appreciation to my family, and especially to Jelena, who have been so supportive and loving.

Chapter 1

Introduction

1.1 Elementary Particle Physics

The physics of elementary particles is a vast and ancient field, with a very ambitious goal: a fundamental description of the nature of both matter and energy. At this point, it is a very mature and well developed field, with a body of theory and a language that constitute what is probably the most accurate theory known to modern science. The language is called Quantum Field Theory. The theory is, some sceptics would say, a forced mixture of several ingredients:

- Quantum Mechanics - the laws that describe the processes at atomic distance scales, where the classical physics of Newton and his successors breaks down and where the traditional notions of reality are challenged.
- Special Relativity - Einstein's discovery and description of the relationships between space and time, and, matter and energy.
- Field Theory - originally developed by Faraday and Maxwell to describe electricity and magnetism is now used in describing the distribution of all

matter and energy in space and time.

- Symmetry Principles - the application of the mathematical Theory of Groups to describe a set of transformations that can be applied to physical systems and leave them unchanged. This is now being used to classify and enumerate those systems.

The importance of CP violation, especially in the early universe formation, can not be overestimated. If indeed all the matter and energy of the Universe were created out of the gravitational potential energy of the Big Bang, symmetries of physical processes would have ensured that equal amounts of matter and anti-matter were produced. But, this is clearly no longer the case, as the Universe we observe is constructed almost entirely of matter with very little antimatter. Back in 1967 Andrei Sakharov established that three requirements must be met in order to produce this matter-antimatter asymmetry [Sak67]:

- a stage in the evolution of the Universe which was far from equilibrium - this was certainly true in the first moments of Universe creation when the expansion was rapid.
- proton decay - modern Grand Unified Theories all predict that protons indeed do decay [GG74] (even though proton decay has yet not been observed, its lifetime is believed to be many orders of magnitude larger than the age of the Universe [G$^+$00]).
- CP violation - this was observed in the kaon system in 1964 [CCFT64], but the magnitude seems to be insufficient to produce the present magnitude of the asymmetry in the universe.

Bearing in mind the fact that CP symmetry violation in B mesons is a lot stronger than in K mesons, one would not be wrong in saying that the comprehensive

study of the *CP violation in B decays, performed at a B factory*, is one of the priorities for High Energy Physics in the following decade. This study is the primary physics goal of the *BABAR* experiment [Col95]. Since the detector also collects large amounts of data for many other interesting channels, the secondary physics goal is to study these processes with very high statistics.

1.2 Analysis Motivation

I chose the production of charmonium mesons as a thesis topic because of several reasons:

- It is an active area of interest for tests of a Non-relativistic quantum chromodynamics (NRQCD), a relatively new method of predicting properties of Quantum chromodynamics (QCD) processes. The production rate, meson momentum and polarization are all quantities that are calculable within this framework. Accurate measurements of these quantities for charmonium mesons produced in B decays and in the continuum below the $B\overline{B}$ threshold will provide interesting tests and constraints on this approach.

- The study of inclusive B decays is limited by systematics, thus presenting great opportunities for determining and cross-checking the performance of several detector components. This is crucial at the early stage of an experiment using a new detector.

- Understanding of inclusive production, properties of the charmonium mesons and efficient reconstruction is valuable for the exclusive charmonium analyses, where the statistics are limited. Some of these channels are crucial in the measurement of CP violation.

- J/ψ production in the continuum has not yet been experimentally measured, and with the high integrated luminosity of our data sample we are able to observe a clean signal and to study properties of those events.

1.3 Thesis Organization

The next chapter contains a short overview of the theoretical formalism relevant for major physics topics studied at *BABAR*, CP violation in the B system being the most important one. Several predictions for the inclusive charmonia branching fractions, polarizations and momentum distributions studied in this analysis are presented as well.

Chapter 3 describes the most important features of the experimental apparatus used, the PEP-II asymmetric e^+e^- collider located at the Stanford Linear Accelerator Center, and the *BABAR* detector. Due to the complexity of these devices, most details are beyond the scope of this thesis and they can be found in the comprehensive paper on the *BABAR* experiment [Col01b].

The study of the inclusive production of the charmonium mesons at *BABAR* is described in Chapter 4. After the discussion of the common analysis techniques, some space is devoted to the detailed study of lepton identification at *BABAR*. Finally, we present several physics results:

- branching fractions for the B meson decaying inclusively into J/ψ, $\psi(2S)$, χ_{c1} and χ_{c2} mesons, distinguishing direct production from the feed down,
- cross-section for the J/ψ production in the continuum below the $\Upsilon(4S)$ resonance,

- upper limit on the inclusive $\Upsilon(4S) \to J/\psi X$ production via a non-$B\overline{B}$ channel,
- measurements of the $\psi(2S) \to \ell^+\ell^-$ branching fractions, with precision exceeding that of currently available values,
- measurements of the polarization, production angle and momentum distributions of the J/ψ mesons, both coming from B decays and created below the $\Upsilon(4S)$ resonance,

The conclusions and a short summary of the analysis are presented in Chapter 5.

1.4 Analysis Organization in *BABAR*

Physics analysis in *BABAR* is centralized to facilitate communication between collaborators, allow for ample cross-checks among related analyses and avoid the duplication of efforts to complete a range of common tasks. This model is necessary for a group of over five hundred physicists.

Data quality management is the responsibility of the DQM group. Based on both the online data quality monitoring and the off-line cross-checks, this group compiles the list of runs usable for physics analysis.

Reliable Monte Carlo is crucial to most physics analyses done at *BABAR*. Both production of the generic Monte Carlo and of the analysis specific signal Monte Carlo is done centrally, under the management of the Simulation Production subgroup of the Computing Group. Several remote computing farms are used but data is collected at SLAC. *BABAR* conditions database contains the experimental conditions for any given running period, and it is constantly being updated. Particular care is taken to ensure that a proportionate number of simulated events

is created using a particular time 'snapshot' of the conditions database, generally corresponding to a given month of operation.

Physics analyses are organized through the Analysis Working Groups (AWG). The Charmonium AWG is charged with studying both inclusive and exclusive processes containing $c\bar{c}$ mesons. Skim[1] definitions and the production of common ntuples[2] are done within the AWG, using the SLAC infrastructure.

The internal review of all analyses scheduled for publication starts within the AWG. The formal approval process is led by a three member review committee assigned to each prospective paper. It includes a series of collaboration wide presentations and readings of supporting documentation, followed by a period when all collaborators are encouraged to comment on the final paper draft.

1.5 Personal and Original Contributions

I joined the *BABAR* collaboration upon my arrival at McGill, in September of 1996. After spending a year on graduate level courses I started working on the small scale prototype drift chamber for *BABAR*. The goal was to measure, using test beams at CERN (Geneva), the resolution of the specific ionization (dE/dx) of the Helium-Isobutane gas, used to facilitate particle identification in the drift chamber. My main contribution was simulating the prototype chamber using GEANT[3] and writing the charged track reconstruction software.

I spent about a year investigating alternative selection methods, such as neural networks and genetic algorithms, and the extent to which they would benefit our

[1] A subset of events containing a particular feature.

[2] A data structure containing the minimal set of information needed to perform a particular physics analysis.

[3] Detector description and simulation tool written at CERN, Switzerland.

experiment. To study generic event tagging, I developed a toy Monte Carlo with two classes of events, defined through four random variables. Simple neural networks with one or two hidden layers provided better discrimination than standard cuts, but the improvement was lost if the data used for network training significantly differed from the data being tagged. This work was published in *Nuclear Instruments & Methods in Physics Research A* [MP99a]. I performed a similar analysis on a realistic problem, using neural networks, a genetic algorithm and a nearest neighbor method to distinguish $B\overline{B}$, τ and continuum Monte Carlo events at *BABAR*. Results were presented at a conference in Ottawa and appeared in the proceedings [MP99b].

Through the particle identification group I contributed to the creation of pure particle samples used to study performance of the particle selectors. Using $K^0_s \to \pi^+\pi^-$ and $D^{*+} \to \pi^+ D^0 \to \pi^+\pi^+ K^-$, I helped define the selection of pure K^+ and π^+ samples.

Prior to commiting to the inclusive charmonium analysis I worked on the exclusive $B^{0,+} \to \psi(2S)K^{0,+}$ decays. The neutral B decay is a CP mode, but its branching fraction has never been measured, making this decay particularly interesting. I had a well defined selection and observed a clean signal when, due to the priorities within the Charmonium group, I decided to concentrate on the inclusive analysis.

The analysis of the inclusive charmonia presented in the remainder of this thesis significantly adds to our understanding of those decays. A uniquely large dataset allows us to extract the branching fractions to a precision superior to existing measurements. Consequently, the understanding of systematic errors is crucial. A considerable effort is made to calculate lepton efficiencies and systematic errors from the inclusive J/ψ data, a procedure which has become a standard in *BABAR*. It is used as well to quantify the differences between the amount of Bremsstrahlung observed in data and in the simulation. These quantities are valuable to

many analyses being conducted within the collaboration. Therefore it was decided to include in the thesis a rather detailed description of the methods and the results, as a record for my *BABAR* colleagues and for particle physicists at large to supplement the necessarily short publications in the journals and conference proceedings. Improved measurement of the $\psi(2S)\to\ell^+\ell^-$ branching fraction significantly reduces the systematic error in the exclusive $B \to \psi(2S)K$ branching fraction. Finally, the first observation of the J/ψ production in the non-resonant e^+e^- annihilations around $\sqrt{s} = 10.58$ GeV/c is inconsistent with Color Singlet Model predictions, strongly favoring the color octet mechanism.

Chapter 2

Theoretical Background

2.1 The Standard Model

Over the last few decades a theory has emerged that describes all of the known elementary particle interactions except gravity. As far as we can tell at present, gravity is far too weak to play an important role in elementary particle processes. In addition to the ingredients mentioned in the previous chapter, this theory incorporates quantum electrodynamics, the theory of electroweak processes and quantum chromodynamics. It has become known as *the Standard Model*. Even though no one pretends that the Standard Model is the definitive, ultimate description of nature, it has an attractive aesthetic feature: all of the fundamental interactions are derived from very few general principles. Those requirements on any candidate physical theory are the following [Bur97]:

- *unitarity* - ensures the conservation of probability;
- *micro-causality and locality* - physical observables must be measurable at different positions and equal times, and, amplitudes for spatially separated

(that is, no light signals can connect one point to the other) physical processes must factorize and be preserved under time evolution;

- *invariance under translations and Lorentz transformations* - Noether's Theorem implies the existence of the corresponding conserved charges (like four-momentum and angular momentum);
- *stability* - ensures existence of the lowest energy state;
- *renormalizability* - the maximum energy scale (Λ) of the theory appears in physical predictions only through a small number of parameters. Alternatively, if the physics at small energy scale is largely insensitive to the physics at high energy scale ($Q \ll \Lambda$) then contributions of order Q/Λ can be neglected;
- *local gauge invariance* - requiring the Lagrangian be invariant under local ($\psi \rightarrow e^{i\theta(x)}\psi$) gauge transformation introduces a new massless vector field, like the photon.

The strong, weak and electromagnetic interactions are understood as arising due to the exchange of various spin 1 bosons amongst spin 1/2 particles that make up matter. Their properties can be summarized as being particles that are associated with the generators of the algebra:

$$SU_c(3) \times SU_L(2) \times U_Y(1) \tag{2.1}$$

The eight spin 1 particles associated with the factor $SU_c(3)$ ('c' is meant to denote color, which is a quantum number carried by strongly interacting quarks) are called gluons and are thought to be massless. The four spin 1 bosons associated with the factor $SU_L(2) \times U_Y(1)$ ('L' is meant to indicate that only left-handed fermions are subject to this unitary symmetry, 'Y' distinguishes the group associated with the weak hypercharge) are related to the physical bosons $W^{\pm}$, Z^0 and the photon.

Table 2.1: The four fundamental forces and their mediators [G+00].

Force	Range [m]	Mediator	Mass [GeV/c^2]	Electric Charge [e]
Gravity	infinite	Graviton	0	0
Weak	$\leq 10^{-18}$	W^+	80.419	1
		W^-	80.419	-1
		Z^0	91.1882	0
Electromagnetism	infinite	Photon	$\leq 2 \times 10^{-25}$	$\leq 5 \times 10^{-30}$
Strong	$\leq 10^{-15}$	Gluons	0	0

Table 2.1 shows the four fundamental forces governing the interactions between both matter and energy. Masses of the gauge bosons are taken from The Review of Particle Physics [G+00]. Gravity, mediated by a, as yet, hypothetical graviton, is excluded from the Standard Model – partly because of the difficulty of describing gravitation even at the classical level.

Apart from spin 1 particles, there are a number of fundamental spin 1/2 particles, called fermions, and the character of their interactions can be summarized by giving their transformation properties with respect to the $SU_c(3) \times SU_L(2) \times U_Y(1)$ gauge group. Fermions transform in a fairly complicated way as there are, at present, three families of particles, with each family coupling identically to all gauge bosons. *Leptons* are, by definition, those spin 1/2 particles which do not take part in strong interactions. Six leptons are known to date. *Hadrons*, on the other hand, are defined as particles which do take part in strong interactions. The spectrum of presently known hadrons is rich but it can be accounted for as the bound states of five quarks (u, d, c, s and b). Table 2.2 is a summary of the Standard Model particle content. The masses were taken from [G+00]. Both

Table 2.2: Elementary particle content of the Standard Model [G+00].

Lepton	Mass [MeV/c^2]	Electric Charge	Quark	Mass [MeV/c^2]	Electric Charge [e]
ν_e	$\leq 3\ 10^{-6}$	0	u	1-5	2/3
e	0.510999	-1	d	3-9	-1/3
ν_μ	$\leq$0.19	0	c	1150-1350	2/3
μ	105.658	-1	s	75-170	-1/3
ν_τ	$\leq$18.2	0	t	174300	2/3
τ	1777.03	-1	b	4000-4400	-1/3

quarks and leptons are grouped into three families. Corresponding antiparticles are not shown. The ν masses are upper limits with a 90% confidence level. The u, d and s quark masses are estimates of "current-quark masses" in a mass independent subtraction scheme, the c and b quark masses are estimated from charmonium, bottomonium, D and B masses, the t quark mass is from the observation of top candidate events at Fermilab.

Once the most general renormalizable Lagrangian built out of the fields corresponding to the expected particle content is diagonalized, all the boson and fermion masses can be read off and are identically zero ! The vanishing of the masses is the consequence of the $SU_c(3) \times SU_L(2) \times U_Y(1)$ invariance of the theory and can be avoided only if this symmetry is spontaneously broken by the ground state. The simplest way to do so is to add to the theory a weakly-coupled spin 0 particle with a potential which is minimized for a non-zero field. This particle 'artificially' added to the Standard Model is the Higgs boson, which is yet to be experimentally observed, and its theoretical foundations are much weaker than the rest of the theory. In a way, the Higgs-doublet parameterizes most of our

ignorance of what lies at the root of the Standard Model. [Bur97]

2.2 The Quark Model

The notion of quarks found its origins in the early 1960s in the course of searches for an organizing principle to describe the proliferation of hadronic particles and resonances observed by the experiments. Gell-Mann [GM61] and Ne'eman [Ne'61] refined an application of the SU(3) representation to introduce an organizational framework of the known baryons and mesons.

Although the idea of quarks met with immediate success by explaining the observed particles and resonances, evidence of quarks as dynamical objects was to come from future experiments. Studies of the deep inelastic scattering of electrons by protons, where the incoming electron scatters off the target proton to produce a massive hadronic recoil system, were able to probe the structure of nucleons. Detailed measurements were made of the differential scattering cross-section as a function of the recoil hadronic invariant mass for different values of the four momentum transfer (q) between the electron and the proton. In the mass region beyond the resonances, the ratio of the observed cross-section to the cross-section expected for a point-like proton exhibited only a weak dependence on the momentum transfer. Proton structure functions depend mainly on a dimensionless variable $x = -q^2/2M\nu$, where $\nu = p \cdot q/M$ is the 'inelasticity'. This observation (called Bjorken scaling) gave support to quark parton models which predicted such scaling behavior.

Quantum chromodynamics (QCD) postulates that all observed particles are color SU(3) singlets. This result was largely motivated by the experimenters' inability to produce isolated quarks. Since gluons themselves are color sources they are

self interacting. This property makes the QCD coupling grow in strength as the separation between two color source increases. If two quarks are made to recede from each other in an energetic collision, the potential energy gained from the increased inter-quark separation will make it favorable for a quark-antiquark pair to be produced from the vacuum and to interact with the receding particles and with each other. This process continues until all quarks are again confined within hadrons. However, the emerging hadrons retain the 'memory' of the primary quark momentum, thus producing 'jets' of particles. Evidence of such jets resulting from energetic quarks was first reported in 1975 in e^+e^- annihilation studies [H$^+$75].

An explanation of the 1974 discovery of the J/ψ meson in the e^+e^- annihilation and $p-Be$ fixed target experiments [A$^+$74b] proved to be one of the quark parton model's great achievements. The unusually high mass and lifetime of the J/ψ meson indicated the presence of fundamentally new physics. The quark model established the observation as the manifestation of a fourth quark, charm (c), in a bound state with its antiquark to form the J/ψ meson. This interpretation was enforced by the discovery of the $\psi(2S)$ meson [A$^+$74a] in its e^+e^- decay channel, a resonance that was immediately identified as a radial excitation ($n = 2$) of the J/ψ ($n = 1$) state. QCD was able to predict the charmonium $c\bar{c}$ bound states and their narrow widths. The subsequent experimental observation of the decay channel $\psi(2S) \rightarrow \pi\pi J/\psi$ served to complement the dilepton channels in clarifying the spectroscopy of the charmonium system.

Evidence for the b quark, often referred to as the 'bottom' or 'beauty', was initially obtained in a manner similar to the one leading to the discovery of charmonium. In 1977, a significant excess in the rate of dimuon production was observed in collisions at a Fermilab fixed target experiment [H$^+$77]. The enhancement, observed near 9.5 GeV/c^2, was interpreted as arising due to decays of bottomonium, a $b\bar{b}$ bound state, and was rapidly confirmed and resolved into two resonances, $\Upsilon(1s)$

and $\Upsilon(2s)$ mesons. Comparisons of the calculated $\Gamma(\Upsilon \rightarrow e^+e^-)$ with the area under the observed Υ line shape suggested that the b quark would join its d and s quark counterparts in possessing a charge of -1/3.

Recent direct observations of the top quark by the two Fermilab experiments, CDF [A+98] and D0 [A+97a], further boosted the three generation quark model. Similar to u and c quarks, t carries electric charge of +2/3.

2.3 Discrete Symmetries

As we have seen, symmetries play a crucial role in the Standard Model as they give us the conserved quantities. Symmetries with respect to the gauge group ($SU_c(3) \times SU_L(2) \times U_Y(1)$) and electromagnetism ($U_{em}(1)$) are continuous, they represent invariance of the physical quantities under transformations governed by one or more continuous parameters (such as position in space or angular orientation). There are, in addition, symmetries associated with discrete parameters and three of them are particularly useful: *parity inversion (P)* - the inversion of the three spatial coordinates through an arbitrary origin converting a left-handed system into a right-handed one, *time reversal (T)* - technically the reversal of the temporal coordinate and *charge conjugation (C)* - a change in the sign of all internal degrees of freedom (electric charge, baryon number, lepton number, isospin, strangeness, charm, beauty, truth) of all particles in the system converting particles into antiparticles. It should be noted that discrete symmetries, even if not violated, do not imply conserved charges.

Until 1956 it was believed that the physical laws were ambidextrous, inverting parity in any physical process must result in another possible process. The evidence of parity violation in weak decays came from the experiment on aligned

Co^{60} beta decay, in which most of the electrons were emitted in the direction of the nuclear spin. [W+57] Among other evidence of P violation, the most noticeable is the fact that all neutrinos are left-handed and all antineutrinos are right-handed, as measured, for example, in $\pi^{\pm} \rightarrow \mu^{\pm} + \nu_{\mu}(\bar{\nu_{\mu}})$. Charge conjugation is, therefore, also not a symmetry of the weak interactions. Applying it to a left-handed neutrino produces a left-handed antineutrino, which doesn't exist! Time reversal is a lot harder to test as no particles are eigenstates of T so we cannot just look at whether a given reaction preserves the eigenvalues of the time reversal operator, or whether the rates of T *even* and T *odd* reactions are the same. A way to test the conservation of T is to measure the rates of a candidate reaction (such as $n+p \rightleftharpoons d+\gamma$) as we run it both ways under the same conditions. As stated by the 'principle of detailed balance' those rates should be the same if PT is conserved. No evidence of T violation was found in strong and electromagnetic interactions, which is hardly surprising considering that both C and P were violated exclusively in weak decays. Unfortunately, inverse-reaction experiments are hard to do in the weak interactions. Consider a typical weak decay $\Lambda \rightarrow p^{+} + \pi^{-}$. The inverse reaction is $p^{+} + \pi^{-} \rightarrow \Lambda$, but it is almost impossible to see such a reaction because a strong interaction of a proton and a pion will always dominate over the weak one [Gri87]. In practice the critical test of T invariance involves measurements of quantities which should be exactly equal to zero if T is a perfect symmetry. The best known experiment to date is the upper limit (no direct evidence of T violation) on the electric dipole moment of a neutron [Ram82]. This experiment tests the P and T invariance.

Nevertheless, there is a compelling answer as to why time reversal cannot be a perfect symmetry of nature. Based on the most general assumptions - Lorentz invariance, quantum mechanics and the idea that interactions are carried by fields - the *TCP Theorem* states that the combined operation of time reversal, charge conjugation and parity inversion, in any order, is an exact symmetry of any in-

teraction. [Lue57] It is not possible to construct a quantum field theory in which TCP is violated. If, as will be presented soon, CP is violated then there must be a compensating violation of T.

2.4 CP Violation

Some temporary relief to the 'problem' of C and P violation was provided by the discovery that the Universe is made of only left-handed particles and right-handed antiparticles. This means that the combined CP symmetry connects the real physical states. With the discovery of the CP violation in the kaon system the sanctity of discrete symmetries was pushed back again. There are three possible manifestations of CP violation:

- CP violation in decay, which occurs for both charged and neutral particles, when the amplitude for a decay and its CP conjugate process have different magnitudes. It is often called direct CP violation;
- CP violation in mixing, which occurs when the two mass eigenstates cannot be chosen as CP eigenstates. It is often referred to as the indirect CP violation;
- CP violation in the interference between decays with and without mixing, which occurs in decays into final states that are common to mesons X^0 and $\bar{X}^0$. Here the interference between $X^0 \to f$ and $X^0 \to \bar{X}^0 \to f$ gives rise to CP violation;

If for a process we have $M = M_1 + e^{i\phi}M_2$ then for a rate and a CP conjugate rate

$$\begin{aligned} P \equiv MM^* &= M_1M_1^* + M_2M_2^* + M_1M_2^*e^{-i\phi} + M_2M_1^*e^{i\phi} \\ P_{CP} \equiv MM_{CP}^* &= M_1M_1^* + M_2M_2^* + M_1M_2^*e^{i\phi} + M_2M_1^*e^{-i\phi} \end{aligned} \tag{2.2}$$

we get $P - P_{CP} \neq 0$, if $\phi \neq 0$. The three family Standard Model does provide the necessary *CP* violating phase through the *CKM matrix*.

Experimentally, the long lived neutral kaon is not a perfect eigenstate of *CP*. Violation in $K_S^0 - K_L^0$ system can come from either mixing or decay. The following quantities are observed in non-leptonic decays:

$$\begin{aligned} \eta_{+-} &= \frac{A(K_L^0 \to \pi^+\pi^-)}{A(K_S^0 \to \pi^+\pi^-)}. \\ \eta_{00} &= \frac{A(K_L^0 \to \pi^0\pi^0)}{A(K_S^0 \to \pi^0\pi^0)}. \end{aligned} \tag{2.3}$$

which are usually expressed in terms of $\epsilon_K = (2\eta_{+-} + \eta_{00})/3$ and $\epsilon'_K = (\eta_{+-} - \eta_{00})/3$. Non-zero value of $\epsilon_K = (2.271 \pm 0.017) \times 10^{-3}$ [G$^+$00] demonstrated *CP* violation. A non-zero value of $\epsilon'_K/\epsilon_K = (2.1 \pm 0.5) \times 10^{-3}$ [G$^+$00] is evidence of violation in decay.

CP violation in the semi-leptonic kaon decays (violation in mixing) has also been observed. It is parameterized by the following quantity (charge asymmetry in leptonic decays):

$$\delta = \frac{\Gamma(K_L^0 \to \pi^- l^+ \nu) - \Gamma(K_L^0 \to \pi^+ l^- \nu)}{\Gamma(K_L^0 \to \pi^- l^+ \nu) + \Gamma(K_L^0 \to \pi^+ l^- \nu)} \tag{2.4}$$

The experimentally measured value of δ (averaged from electron and muon channels) is: $\delta = (0.333 \pm 0.014)\%$ [G$^+$00]. This asymmetry provides an absolute distinction between matter and antimatter and an unambiguous, convention free definition of positive charge as the charge of a lepton preferentially produced in the decay of a long-lived neutral kaon.

A Lagrangian is *CP* conserving if all the coupling and mass terms can be made real by an appropriate set of field redefinitions. The most general theory with only two quark generations and a single Higgs multiplet is of that type. However, when a third quark generation is added, the most general quark mass matrix does allow *CP* violation. The three generation Standard Model with a single Higgs

multiplet has only a single non-zero phase and it appears in the matrix which relates weak eigenstates to mass eigenstates. This is commonly known as the CKM (Cabibbo-Kobayashi-Maskawa) matrix [KM73], which is a generalization of the two generation quark mixing matrix parameterized by a single (Cabibbo) angle [Cab63].

2.4.1 The Cabibbo-Kobayashi-Maskawa Matrix and the Unitarity Triangle

By convention, the three charge 2/3 quarks (u, c and t) are unmixed, and all the mixing is expressed in terms of a 3 × 3 unitary matrix V operating on the charge -1/3 quarks (d, s and b):

$$\begin{pmatrix} d' \\ s' \\ b' \end{pmatrix} = \begin{pmatrix} V_{ud} & V_{us} & V_{ub} \\ V_{cd} & V_{cs} & V_{cb} \\ V_{td} & V_{ts} & V_{tb} \end{pmatrix} \begin{pmatrix} d \\ s \\ b \end{pmatrix}$$

The values of individual matrix elements can in principle all be determined from weak decays of relevant quarks or from deep inelastic neutrino scattering. Using the unitarity constraint and assuming only three quark generations, present 90% confidence limits on the magnitudes of the elements of the CKM matrix are [G+00]:

$$V = \begin{pmatrix} 0.9742 - 0.9757 & 0.219 - 0.226 & 0.002 - 0.005 \\ 0.219 - 0.225 & 0.9734 - 0.9749 & 0.037 - 0.043 \\ 0.004 - 0.014 & 0.035 - 0.043 & 0.9990 - 0.9993 \end{pmatrix}$$

A useful parameterization of the CKM matrix elements, up to the fourth power in λ, where λ is the sine of the Cabibbo angle ($\lambda \approx 0.22$, A and $\eta^2 + \rho^2$ are of

$O(1)$) is due to Wolfenstein: [Wol83]

$$V = \begin{pmatrix} 1-\frac{1}{2}\lambda^2 & \lambda & A\lambda^3(\rho - i\eta) \\ -\lambda & 1-\frac{1}{2}\lambda^2 & A\lambda^2 \\ A\lambda^3(1-\rho-i\eta) & -A\lambda^2 & 1 \end{pmatrix}$$

The unitarity of the *CKM* matrix leads to relations such as:

$$V_{tb}V_{td}^* + V_{cb}V_{cd}^* + V_{ub}V_{ud}^* = 0 \tag{2.5}$$

The *unitarity triangle* [CK84] is a geometrical representation of this relation in the complex plane: the three complex quantities, $V_{tb}V_{td}^*$, $V_{cb}V_{cd}^*$ and $V_{ub}V_{ud}^*$ should form a triangle, as shown in Figure 2.1. The rescaled unitarity triangle is derived

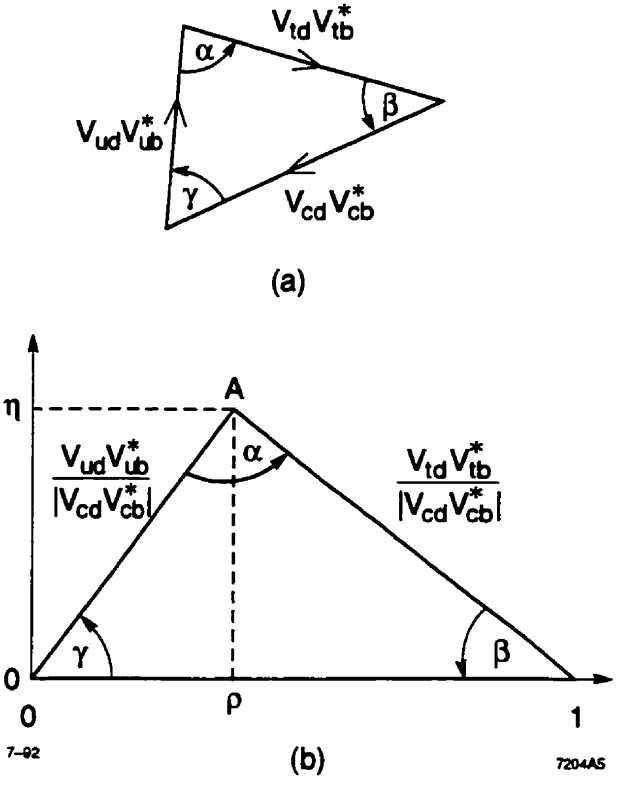

Figure 2.1: The unitarity triangle (a) and the rescaled unitarity triangle (b).

by choosing a phase convention such that $V_{cd}V_{cb}^*$ is real and dividing the lengths of all sides by $|V_{cd}V_{cb}^*|$.

The unitarity triangle gives a relationship between the two most poorly determined entries of the *CKM* matrix, V_{ub} and V_{td}. It is thus convenient to present constraints on the *CKM* parameters as bounds on the coordinates of the vertex A of the unitarity triangle. Figure 2.2 [Col01a] shows the unitarity triangle in the ($\bar{\rho} = \rho(1 - \lambda^2/2), \bar{\eta} = \eta(1 - \lambda^2/2)$) plane, with *BABAR*'s measured central value of sin2β shown as two straight lines. There is a two-fold ambiguity in deriving a

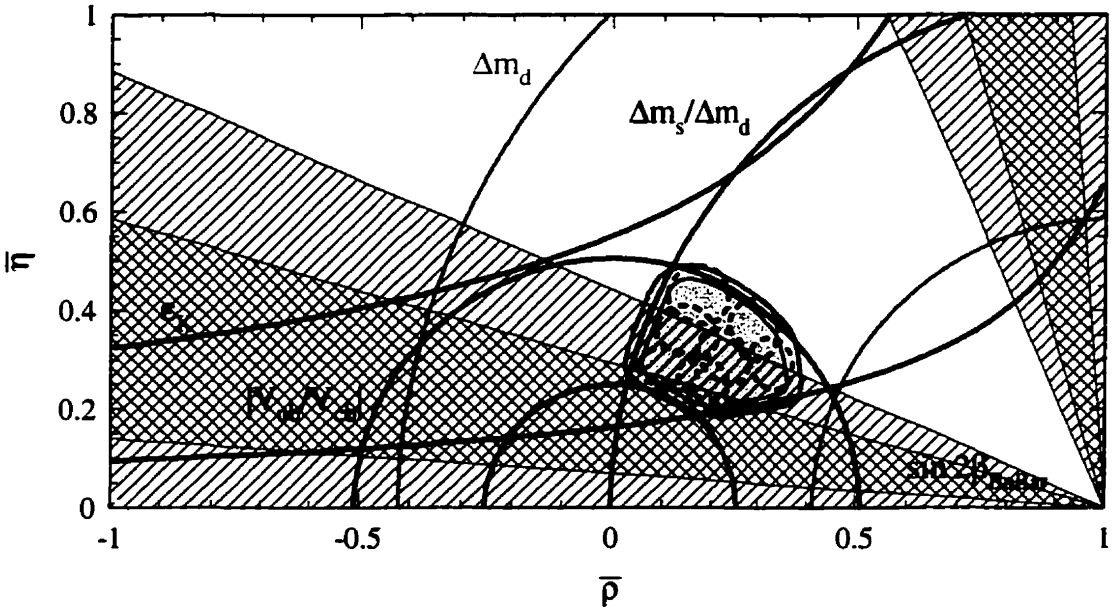

Figure 2.2: Standard Model constraints in the $\bar{\rho}\bar{\eta}$ plane. 1 and 2σ ranges of *BABAR* measurement of $\sin 2\beta$ are shown.

value of β from a measurement of sin2β. Both choices are shown with cross-hatched regions corresponding to one and two times the one-standard-deviation experimental uncertainty. The ellipses correspond to the regions allowed by all other measurements that constrain the unitarity triangle. The following set of measurements is used in determining these allowed solutions: $|V_{cb}| = 0.0402 \pm$

0.017, $|V_{ub}/V_{cb}| = \langle |V_{ub}/V_{cb}| \rangle \pm 0.0079$, Δm_d[1] $= 0.472 \pm 0.017\,\hbar\,\mathrm{ps}^{-1}$ and $|\epsilon_K| = (2.271 \pm 0.017) \times 10^{-3}$, and for Δm_s[2] the set of amplitudes corresponding to a 95%CL limit of $14.6\,\hbar\,\mathrm{ps}^{-1}$. The parameters: $\langle |V_{ub}/V_{cb}| \rangle$, B_K[3], $f_{B_d}\sqrt{B_{B_d}}$[4] and $\xi_s = f_{B_s}\sqrt{B_{B_s}}/f_{B_d}\sqrt{B_{B_d}}$, are scanned in the range [0.070, 0.100], [0.720, 0.980], [185, 255] MeV and [1.07, 1.21], respectively.

In addition, the predictions for the *CP* asymmetries in neutral B decays to certain *CP* eigenstates are fully determined by the values of the three angles, α, β and γ, of the unitarity triangle.

2.4.2 *CP* Violation in the $B^0 - \bar{B}^0$ System

In the neutral B system, the two mass eigenstates (heavy and light) are given as $|B_{H,L}> = p|B^0> \pm q|\bar{B}^0>$. The time-dependent *CP* asymmetry in the B decays is defined as:

$$\begin{aligned} a_{f_{cp}}(t) &\equiv \frac{\Gamma(B^0_{\mathrm{phys}}(t) \to f_{CP}) - \Gamma(\bar{B}^0_{\mathrm{phys}}(t) \to f_{CP})}{\Gamma(B^0_{\mathrm{phys}}(t) \to f_{CP}) + \Gamma(\bar{B}^0_{\mathrm{phys}}(t) \to f_{CP})} \\ &= \frac{(1 - |\lambda|^2)\cos(\Delta M t) - 2\mathrm{Im}\lambda \sin(\Delta M t)}{1 + |\lambda|^2}, \end{aligned} \tag{2.6}$$

where Γ are time-dependent rates for initially pure B^0 or $\bar{B}^0$ states to decay into a *CP* eigenstate f_{CP}, $\lambda \equiv \frac{q}{p}\frac{\bar{A}}{A}$ ($A(\bar{A})$ is the amplitude for a $B^0(\bar{B}^0)$ to decay into f_{CP}), ΔM is the mass difference of heavy and light B mesons, and t is the time elapsed since the physical states were pure B^0 and $\bar{B}^0$. If all amplitudes that contribute to the direct decay have the same *CKM* phase, such that $\bar{A}/A = e^{-2i\phi_D}$

[1] Difference of the two B_d mass eigenstates: $m(B^0_H) - m(B^0_L)$.

[2] Difference of the two B_s mass eigenstates: $m(B^0_H) - m(B^0_L)$.

[3] A scale independent parameter, represents the ignorance of a particular hadronic matrix element in the K system. Obtained in QCD lattice calculation.

[4] $f_{B_{d,s}}$ and $B_{B_{d,s}}$ parameterize the hadronic uncertainty in the B_d and B_s systems, similar to B_K.

and if $q/p = e^{2i\phi_M}$, where ϕ_M is the *CKM* phase in the $B - \bar{B}$ mixing (relevant Feynman diagrams are shown in Figure 2.3), then CP asymmetry simplifies considerably:

$$a_{f_{cp}}(t) = -\mathrm{Im}\lambda \sin(\Delta M t)$$
$$\lambda = e^{2i(\phi_M - \phi_D)} \Rightarrow \mathrm{Im}\lambda = \sin 2(\phi_M - \phi_D). \tag{2.7}$$

Note that the time integrated asymmetry vanishes. To measure Imλ one must

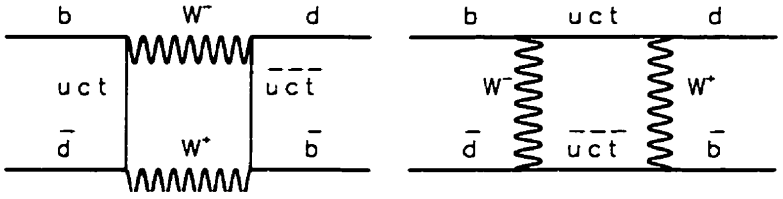

Figure 2.3: Feynman diagrams responsible for $B^0 - \bar{B}^0$ mixing.

know the difference between decay times of the two B mesons. This point is instrumental for the experimental setup described in Chapter 3.

Finally, the aim is to 'overdetermine' the unitarity triangle, to make enough independent measurements of the sides and the angles and thus check the validity of the Standard Model.

A neutral B meson decaying into charmonium and a kaon (Figure 2.4) belongs to a specific class of decays for which the CP asymmetry can be related to $\sin 2\beta$. For these modes

$$\lambda(B^0 \to \psi K_s^0) = -\left(\frac{V_{tb}^* V_{td}}{V_{tb} V_{td}^*}\right)\left(\frac{V_{cs}^* V_{cb}}{V_{cs} V_{cb}^*}\right)\left(\frac{V_{cd}^* V_{cs}}{V_{cd} V_{cs}^*}\right), \tag{2.8}$$

where the first term comes from the $B^0 - \bar{B}^0$ mixing, the second from the ratio of decay amplitudes and the third from the $K^0 - \bar{K}^0$ mixing. Hence,

$$\mathrm{Im}\lambda(B^0 \to \psi K_s^0) = \sin 2\beta \ . \tag{2.9}$$

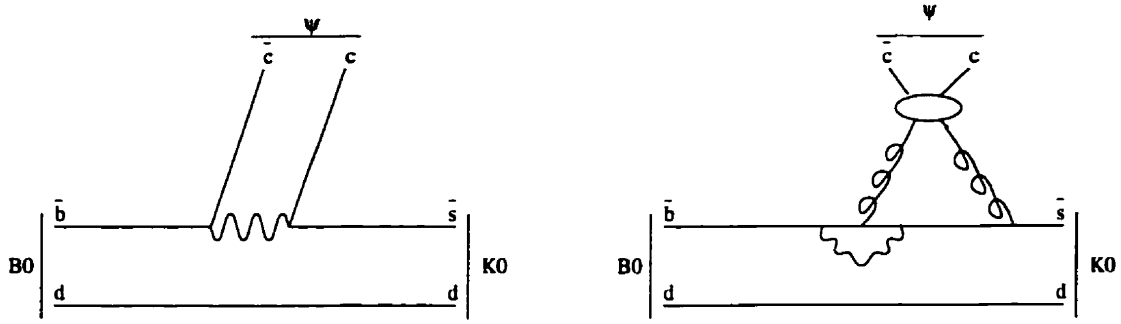

Figure 2.4: Feynman diagrams for the color-suppressed decay $B^0 \rightarrow$ charmonium + K^0, tree (left) and penguin (right).

For decays of this type, the tree amplitudes are color-suppressed because of the topology. The decay only occurs when the $\bar{c}s$ pair, itself a color singlet, conspires with the c quark and the $\bar{d}$ quark to form color singlet $c\bar{c}$ and $s\bar{d}$ mesons. In this mechanism, the $\bar{d}$ quark is assumed to be a 'spectator' of the weak process.

The dominant penguin contribution has the same weak phase as the tree contribution. The only term with a different phase comes from a Cabbibo suppressed ($\mathcal{O}(\lambda^2)$ where λ is the Wolfenstein parameter) penguin decay. Thus, to good accuracy and independent of any assumptions about factorization, color suppression, or the role of final state interactions, $|\lambda| = |\frac{q}{p}\frac{\bar{A}}{A}| = 1$. The simple relationship between the CP asymmetry and the $\sin 2\beta$ has negligible theoretical uncertainty [Col98]. For these reasons decays of the neutral B into charmonium mesons and a kaon are called the 'golden modes' for studying CP violation in the B system. Dominant contribution to the *BABAR* measurement of $\sin 2\beta$ comes from $B \rightarrow J/\psi K_s^0$ decays.

2.4.3 Beyond the Standard Model

The above discussion assumes that the only source of *CP* violation is the phase of the *CKM* matrix. Models beyond the Standard Model involve other phases and, consequently, the measurements of the *CP* asymmetries may violate the constraints of the unitarity triangle. Even in the absence of new *CP* violating phases, the sides of the triangle may be affected by new contributions. In certain models, such as four-generation model and models involving Z-mediated flavor-changing neutral currents, the unitarity triangle turns into a quadrangle.

Through a measurement of the *CP* asymmetries, the presence of new physics can be detected in several ways: *(i)* the relation $\alpha + \beta + \gamma = \pi$ is violated, *(ii)* even if $\alpha + \beta + \gamma = \pi$, the value for the *CP* phase can be outside of the Standard Model predictions, *(iii)* the CP angles are consistent with the Standard Model predictions but are inconsistent with the measured sides of the unitarity triangle.

2.5 Inclusive Charmonium Production

When studying charmonium production in e^+e^- annihilation, we draw a distinction between two fundamentally different mechanisms: subsequent decays of the B mesons produced through a decay of the $\Upsilon(4S)$ resonance (as in Figure 2.4), and charmonium production in the continuum events. At our energies, $\sqrt{s} = M_{\Upsilon(4S)}$, the effective e^+e^- cross-section is 1.05 nb for $b\bar{b}$ events and 1.30 nb for $c\bar{c}$ events [Col98].

Most theoretical predictions have been based on the 'color singlet model' (CSM) which assumes $c\bar{c}$ is produced in a color singlet state by a parton collision whose cross-section can be calculated using perturbation theory. The latest developments in both theory and experiment have challenged the simple assumption that a $c\bar{c}$

production in the color-octet state is negligible. The CDF experiment measured the cross-section for prompt production of J/ψ at high p_T and found it to be more than an order of magnitude larger than the predictions of the color-singlet model [A+92]. Similarly, Z^0 data from LEP [Dc+94, col99] are about a factor of 3 above the CSM prediction.

The Non-relativistic QCD (NRQCD) factorization approach gives quarkonium production cross-sections as a finite sum of short-distance coefficients multiplying the long-distance matrix elements (MEs). For the factorization to hold, the latter have to be process-independent. The values of the matrix elements have to be extracted from the fits to various experimental results. Current accuracy of ME values extracted from e^+e^- annihilation and Z^0 decays is limited by statistics. In contrast, constraints from the Υ and B decays are currently limited by theory. Presently, the uncertainties in the ME values are generally above 100%.

The NRQCD approach implies that color-octet processes must contribute to the cross-section. A factorization formalism for calculating inclusive charmonium cross-sections to any order in α_s and v^2, where v is the typical relative velocity of the charm quark, has been developed [BBL95].

2.5.1 B Decays to Charmonium Mesons

Branching fractions of the inclusive B meson decays into J/ψ, $\psi(2S)$ and χ_{c1} have been measured by other experiments. Only an upper limit on the $B \to \chi_{c2}X$ branching fraction is known.

Theoretical calculations are difficult because of possible large corrections to factorization since there is not a lot of energy in the decay products. Using expansion in Λ_{QCD}/m_b, B →charmonium branching fractions can be calculated perturba-

tively. Leading order calculations assuming color singlet production are uncertain up to a factor of 10. For instance, a leading order CSM calculation of the direct $B \to J/\psi X$ branching fraction yields $\mathcal{B}(B \to J/\psi X) = (0.09 - 0.84)\%$ [BMR99], a result consistent with experimental observations. This uncertainty is expected to reduce to a factor of 2-3 if next to leading order is included. Color singlet predictions for P wave Charmonium mesons ($\mathcal{B}(B \to \chi_{c1\&2} X)$) are still below the observed production rate but next to leading order corrections to the color octet channels are positive [Sch99].

2.5.2 J/ψ Production in the Continuum

The production of charmonium requires the creation of a $c\bar{c}$ pair with energy greater than twice the charm mass (m_c). Initial theoretical predictions were based on the assumption that the quark and antiquark must be in a color singlet state. Since QCD coupling is small at m_c scale, theoretical analysis is performed using perturbation theory in α_s [Bra96].

Color singlet model calculations predict the cross-section for the direct J/ψ production to be $\sqrt{s} = 10.58$ GeV of 0.81 pb. The dominant process is gluon emission, with a quark process contribution at the 10 % level [CL96]. Leading order Feynman diagrams are shown in Figure 2.5.

Full NRQCD calculations yield a significant color-octet contribution at this energy, increasing the cross-section to 2.9 pb [Sch99].

The signal for the color-octet contributions is a change in the angular distribution of the produced J/ψ, which has a form $1 + A\cos^2\theta$, where θ is the angle between the J/ψ direction and the beam axis measured in the center of mass frame. At the upper end of the center of mass energy spectrum ($E^*_{J/\psi} > 4.75$ GeV) the color-

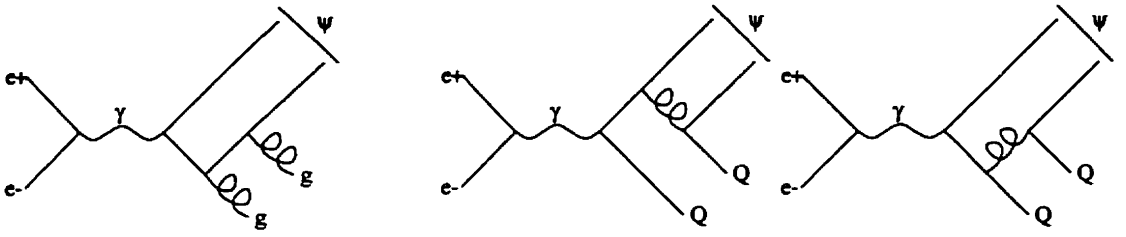

Figure 2.5: Leading order Feynman diagrams which mediate $e^+e^- \rightarrow \psi X + gg$ production (left) and $e^+e^- \rightarrow \psi X + Q\bar{Q}$ production (middle and right).

singlet model predicts $A \approx -0.84$. Adding the color-octet production changes the calculated value to $A \geq +0.62$ [Bra96].

Chapter 3

The Experimental Setup

The following chapter is a brief summary of the *BABAR* Technical Design Report [Col95], the *BABAR* Physics Book [Col98], a summary article on the first year of the experiment [Col00] and the *BABAR* detector paper that will shortly be published in *Nuclear Instruments and Methods in Physics Research* [Col01b]. Other references are quoted where necessary.

3.1 Motivation

While it has been understood for several years that the measurement of *CP* violating asymmetries in B^0 decays could lead to important tests of the *CKM* matrix, the experiments seemed beyond reach. The discovery of a surprisingly long b quark lifetime (first observed at SLAC [F$^+$83]) together with a large generic $B^0 - \bar{B}^0$ mixing (first observed by UA1 [A$^+$87a]) and a large specific $B^0_d - \bar{B}^0_d$ mixing (first observed by ARGUS [A$^+$87b]) made it possible to contemplate such experiments. Long lifetimes of B mesons allow for the extraction of difference in decay times by measuring the decay vertices. Large mixing makes Imλ observable (see Equa-

tion 2.7). It soon became clear that the most straightforward approach involved experiments at a variety of e^+e^- machines, either in the $\Upsilon(4S)$ region (10.58 GeV), in the PEP/PETRA continuum region, or at the Z^0 pole (91.19 GeV).

The most favorable e^+e^- experimental situation, which is the one producing the smallest statistical error with the least integrated luminosity, is the asymmetric storage ring first proposed by Oddone. [Odd87] This machine boosts the decaying B^0 mesons in the laboratory frame (as illustrated in Figure 3.1), allowing existing vertex measuring technology to measure the time order of $B^0 - \bar{B}^0$ decay pairs (remember that in order to extract the CP violating parameter Imλ from the measured asymmetry, see Eq. 2.7, one needs to know the time t between the two B^0 decays) even with the short B meson flight distance.

3.2 The PEP-II Collider

The PEP-II colliding beam storage ring, at Stanford Linear Accelerator Center (SLAC), in Stanford, California, has delivered the required luminosity of 3×10^{33} cm^{-2}s^{-1}, and ultimately promises luminosities as high as 10^{34}, with asymmetric $\Upsilon(4S)$ production at $\beta\gamma = 0.56$. Such a boost results in an average displacement between B vertices of 260 μm, which is crucial for studying the cleanest and most promising CP violating modes. The $B\overline{B}$ production rate is 3 Hz at the design luminosity, rising to 10 Hz at 10^{34} cm^{-2}s^{-1}.

At PEP-II, 9.0 GeV electrons in a High Energy Ring (HER) collide with 3.1 GeV positrons in a Low Energy Ring (LER), resulting in total center of momentum energy of 10.58 GeV. Some beam parameters are listed in Table 3.1.

Electrons and positrons are produced by the SLAC Linac. Its high intensity makes it optimal to refresh the colliding beams when the luminosity drops to about 90%

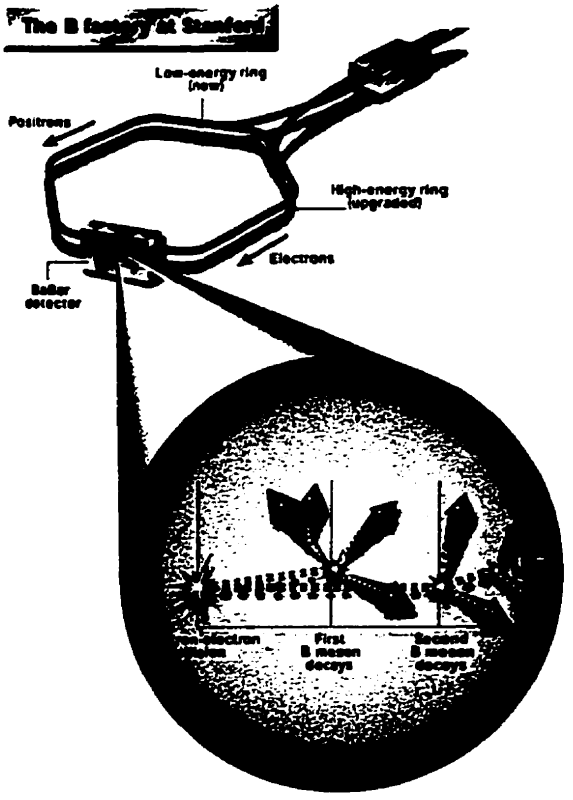

Figure 3.1: Schematics of an e^+e^- collision at the SLAC B factory and the subsequent decay of the B mesons. Because of the asymmetric energies of the e^+ and e^- beams, B mesons are moving in the lab frame.

of the peak value.

The rings are housed in the 2.2 km former PEP tunnel (Figure 3.2) but with distinct vacuum and accelerating structures. The High Energy Ring (HER) reuses the magnets of the old PEP machine whereas the Low Energy Ring (LER) is new and is put in place on top of the HER. The PEP-II design has 1658 bunches, each containing 2.1×10^{10} electrons (HER) and 5.9×10^{10} positrons (LER), spaced at 4.2 ns. The RF system provides a total power of 5.1 MW from seven klystron stations driving 24 conventional copper 476 MHz RF cavities. Bunches are brought into a common vacuum chamber (pressure of a few nTorr) and into head-on colli-

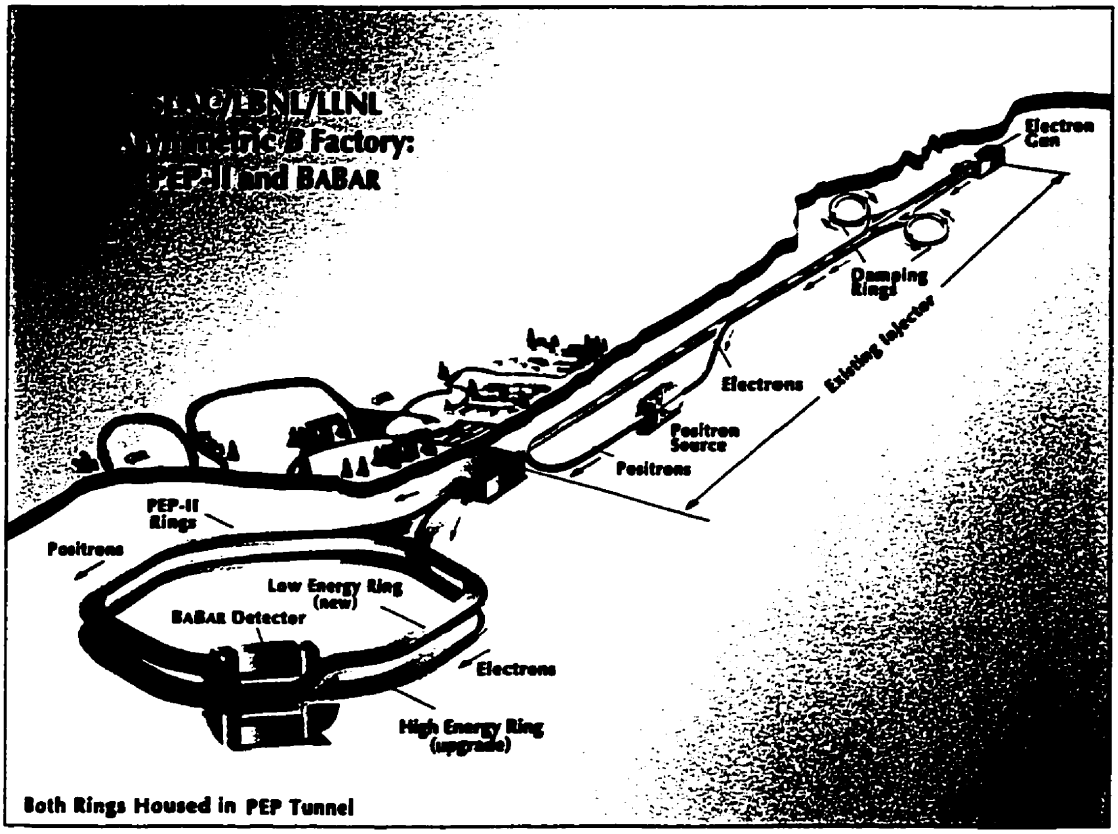

Figure 3.2: Schematic view of the PEP-II Collider at Stanford Linear Accelerator Center.

sions in an interaction region within a 2.5 cm-radius beryllium beam-pipe around which *BABAR* is located.

The PEP-II e^+e^- collider became operational in July 1998 with the completion of the LER. The first collisions were seen shortly thereafter. Fall and winter 1998 PEP-II runs concentrated on raising the beam currents and increasing the luminosity. In February 1999, the peak luminosity reached $5.2 \times 10^{32}\,\mathrm{cm}^{-2}\mathrm{s}^{-1}$. In a two month spring down time, the *BABAR* detector was installed. PEP-II turned on May 10^{th} and *BABAR* saw its first hadronic event on May 26^{th} 1999. In August 1999, PEP-II passed the world record for luminosity, achieving $8.1 \times 10^{32}\,\mathrm{cm}^{-2}\mathrm{s}^{-1}$. In June 2000, PEP-II delivered an integrated luminosity of $174\,\mathrm{pb}^{-1}$ per day, above

Table 3.1: PEP-II LER and HER design parameters and typical performance during the first year of running.

	HER		LER	
Parameter	Design	Typical	Design	Typical
Energy (GeV)	9.0	9.0	3.1	3.1
Number of Bunches	1658	553-829	1658	553-829
Total Beam Current (A)	1.0 (0.7)	0.7	2.14	1.10
Beam Lifetime	4hrs	9hrs	4hrs	3hrs
	@ 1.0A	@ 0.70A	@ 2.0A	@1.1A

the design goal for daily integrated luminosity of $135\,\mathrm{pb}^{-1}$. A peak luminosity of $3.1 \times 10^{33}\,\mathrm{cm}^{-2}\mathrm{s}^{-1}$, above the 3.0 design peak luminosity, was achieved with a 1.55 A positron current, 0.80 A electron current and 692 bunches. During Run 1 PEP-II has delivered 23.9 fb^{-1} of luminosity, and 22.3 fb^{-1} were recorded by *BABAR*. Luminosity summary plots for *BABAR* Run 1 are shown in Figure 3.3.

Operationally, the acceptable level of background is determined primarily by the radiation hardness of the Silicon Vertex Tracker (SVT) and Electromagnetic Calorimeter (EMC) detectors, and by requiring that the current in Drift Chamber (DCH) wires is within acceptable limits. The Level-1 (L1) trigger rate and the occupancy in the other detector systems also constitute occasional limitations. Careful measurement, analysis and simulation of the background sources and their impact have led to a detailed understanding of their effects and execution of effective remedies. The primary causes of steady-state backgrounds in PEP-II are. in order of increasing importance:

- Synchrotron radiation generated in the bending magnets and final focusing quadrupoles in the incoming HER and LER beam lines. Careful layout of

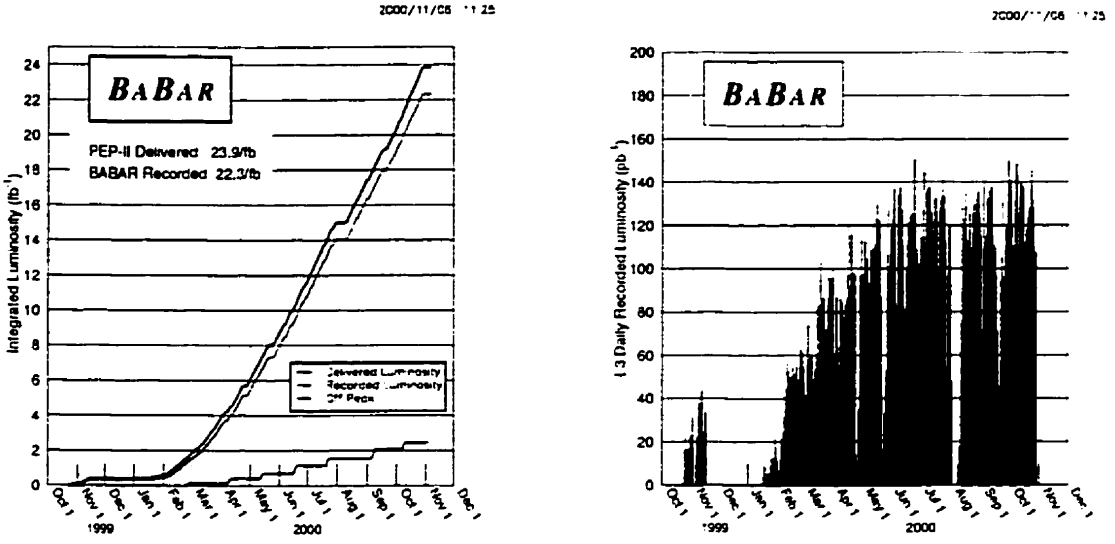

Figure 3.3: Integrated luminosity. on-resonance and off-resonance. delivered by PEP-II (left) and daily integrated luminosity (right) for 1999 and 2000 running period.

the interaction-region area and a conservative synchrotron radiation masking scheme have proven very effective against these sources.

- The interaction of beam particles with residual gas around the rings (beam-gas). which constitutes the primary source of radiation damage and has had. averaged over this first run. the largest impact on operational efficiency.

- Collision-related electromagnetic shower debris. dominated by energy-degraded $e^{\pm}$ from radiative-Bhabha scattering which strike vacuum components within a few meters of the interaction point (IP). This background. directly proportional to the instantaneous luminosity. was barely detectable in early running: it now noticeably affects all detectors except the SVT.

The experimental challenge is then to provide high efficiency. high resolution exclusive state reconstruction in a situation new to the e^+e^- collider world: a center of mass in motion in the laboratory.

3.3 The *BABAR* Detector

The primary goal of the *BABAR* experiment is the systematic study of *CP* violation in neutral B decays, as discussed in the previous chapter. The secondary goals are to explore the wide range of other B physics, charm physics, τ physics, two-photon physics and Υ physics that becomes available with the high luminosity of PEP-II.

The critical experimental objectives to achieve the required sensitivity for *CP* measurements are: [Col95]

- To reconstruct the decays of B^0 mesons into a wide variety of exclusive final states with high efficiency and low background.
- To tag the flavor of the other B meson in the event with high efficiency and purity.
- To measure the relative decay time of the two B mesons.

In order to achieve these physics goals and to function optimally, the detector needs:

- The maximum possible acceptance in the center-of-mass system. The asymmetry of the beams causes the decay products to be boosted forward in the laboratory frame. This puts the solid angle in the forward direction at a premium. Although the boost is not great (a 90^o polar angle in the center of mass frame translates into a 60^o polar angle in the lab frame), optimizing the detector acceptance leads to an asymmetric detector.
- To accommodate machine components close to the interaction region. The high luminosities needed to achieve the physics goals at *BABAR* necessitate

unusual beam optics with machine elements coming very close to the interaction region.

- Excellent vertex resolution. The B mesons travel almost parallel to the z-axis, so that their decay time difference is measured via a difference in the z-components of their decay positions. This stresses the z-component of vertex resolution. The experiment needs the best possible vertex resolution in order to help in the discrimination of beauty, charm and light quark vertices. Vertex resolution also stresses the importance of minimizing multiple scattering.

- To do tracking over the range ~ 60 MeV/$c < p_t <\sim 4$ GeV/c.

- Discrimination between e, μ, π, K and p over a wide kinematic range. Tagging of the flavor of B-meson decays is needed in many analyses, and this can be done with high efficiency and purity only if electrons, muons and kaons can be well-identified. In addition, π-K discrimination at high momenta (2–4 GeV) is essential in order to distinguish between the decay channels $B^0 \to \pi^+\pi^-$ and $B^0 \to K^\pm\pi^\mp$, $B^0 \to \pi^\pm\rho^\mp$ and $B^0 \to K\rho$ and $B^0 \to K^*\pi$.

- To detect photons and π^0's over the wide energy range ~ 20 MeV $< E <\sim 5$ GeV.

- To have neutral hadron identification capability.

The *BABAR* detector was designed to provide all the above features. A schematic of the detector is shown in Figure 3.4. Major subsystems of the detector include:

1. A Silicon Vertex Tracker (SVT). This provides precise position information on charged tracks, and also is the sole tracking device for very low energy charged particles.

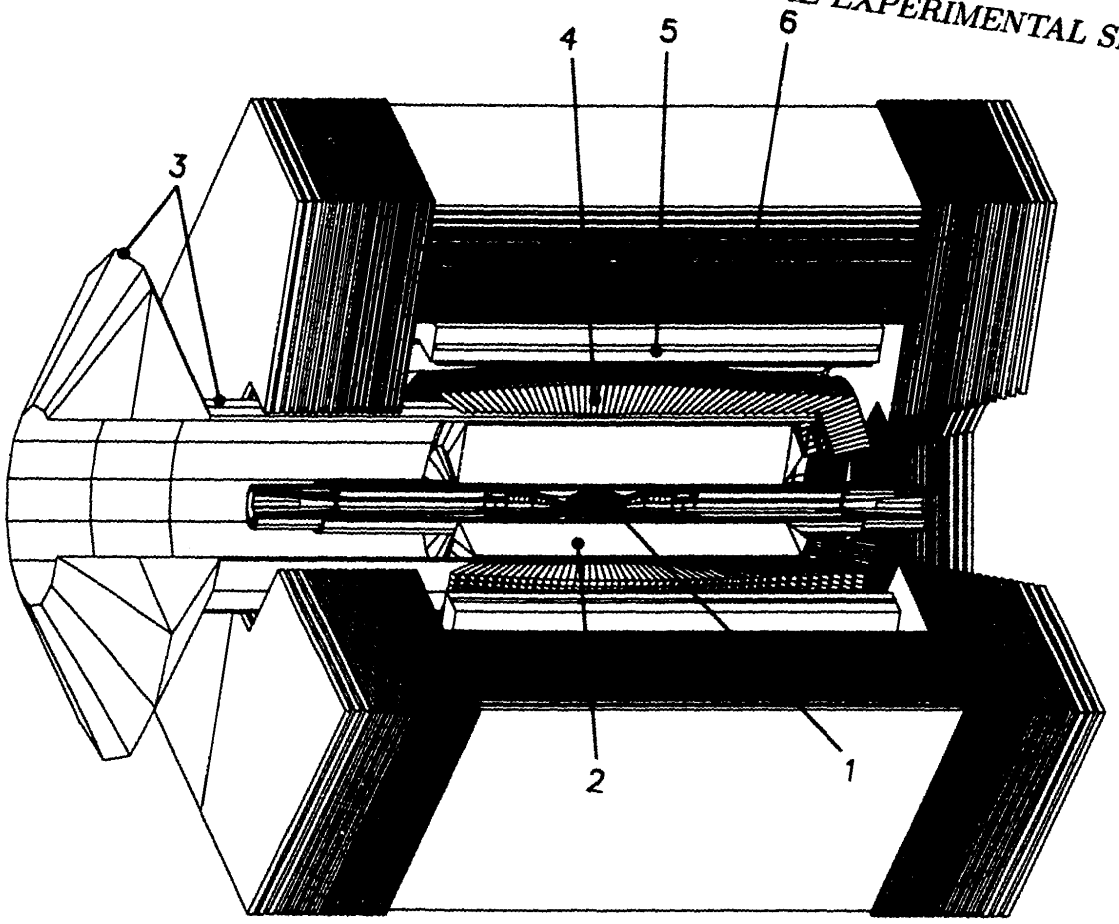

Figure 3.4: Three dimensional view of the *BABAR* detector.

2. A Drift Chamber (DCH) filled with a helium-based gas (80% Helium and 20% Isobutane), in order to try to minimize multiple scattering. This provides the main momentum measurement for charged particles and helps in particle identification through energy loss measurements.

3. A Detector of Internally Reflected Čerenkov light (DIRC). It is designed and optimized for charged hadron particle identification.

4. A Cesium Iodide Electromagnetic Calorimeter (EMC). In addition to the barrel (the central portion of the of the detector, radially beyond the DCH)

component, the EMC has a forward endcap covering small polar angles and thus increasing total acceptance. There is no endcap in the backward direction, for reasons of economy, as it was found that the boost prevents a good fraction of particles from going in the extreme backward direction. In addition to energy measurements of photons and electrons, the calorimeter provides good electron identification down to about 0.5 GeV. It also contributes information for neutral hadron identification.

5. A superconducting coil, which provides a 1.5 T solenoidal magnetic field.

6. An Instrumented Flux Return (IFR) for muon identification down to about 0.6 GeV and neutral hadron identification. The latter is of particular interest in the CP-violating time-dependent asymmetries in $B^0 \to J/\Psi K_L^0$ as a cross-check to the result in the $B^0 \to J/\Psi K_s^0$ channel. The IFR also serves as a coarse hadron calorimeter.

All of those detectors operate with good performance for laboratory polar angle between 17^0 and 150^0, corresponding to the asymmetric range $-0.95 < \cos\theta_{cm} < 0.87$ due to the Lorentz boost. A summary of the individual detector components is given in Table 3.2.

The detector coordinate system is defined with $+z$ in the boost (high energy beam) direction. The origin is the nominal collision point, which is offset by 34 cm in the $-z$ direction from the geometrical center of the detector magnet. The tracking system in *BABAR* consists of the vertex detector and a drift chamber. The vertex detector is used to precisely measure the two impact parameters for charged tracks (z and $r-\phi$). These measurements are used to determine the difference in decay times of two B^0 mesons. Charged particles with transverse momentum (p_t) between $\sim$ 40 MeV/c and $\sim$ 100 MeV/c are tracked only with the vertex detector, which must therefore provide good pattern recognition as a

Table 3.2: The *BABAR* detector - parameter summary.

Detector	Technology	Dimensions	Performance
SVT	Double-sided Silicon Strip	5 Layers $r = 3.2 - 14.4$cm $-0.87 < \cos\theta < 0.96$	$\sigma_z = \sigma_{xy} =$ $= 50\mu\text{m}/p_t \oplus 15\mu\text{m}$ $\sigma_\phi = \sigma_\theta = 1.6\text{mr}/p_t$
DC	Small Cell Drift Chamber	40 Layers $r = 22.5 - 80.0$cm $-111 < z < 166$cm	$\sigma(p_t)/p_t =$ $= 0.21\% + 0.14\% \times p_t$ $\sigma_{\text{spatial}} \approx 140\ \mu$m
PID	DIRC	$1.75 \times 3.5\text{cm}^2$ quartz $-0.84 < \cos\theta < 0.90$	$N_{pe} = 20 - 50$ $\geq 4\sigma$ K/π separation
CAL	CsI(Ti)	$16 - 17.5\ X_0$ $\sim 4.8 \times 4.8$cm crystals	$\sigma_E/E = 1\%/E^{\frac{1}{4}} \oplus 1.2\%$ $\sigma_\theta = 3\text{mr}/\sqrt{E} \oplus 2\text{mr}$
MAG	Superconducting Segmented Iron	$IR = 1.40$m $L = 3.85$m	$B = 1.5$T
IFR	RPC	16-17 Layers	$\epsilon_\mu > 90\%$ for $p_\mu > 0.8\text{GeV}/c$

stand alone device.

The drift chamber (extending from 22.5 cm in radius to 80 cm) is used primarily to achieve excellent momentum resolution and pattern recognition for charged particles with $p_t > 100$ MeV/c. It also supplies information for the charged track trigger and a measurement of dE/dx for particle identification. The optimum resolution is achieved by having a continuous tracking volume with a minimum amount of material to minimize multiple scattering. By using helium-based gas mixture with low mass wires and a magnetic field of 1.5 T, very good momentum

resolution can be obtained. The chamber is designed to minimize the amount of material in front of the particle identification and calorimeter systems in the heavily populated forward direction. Hence the readout electronics are mounted only on the backward end of the chamber.

Two primary goals for the particle identification system are to identify kaons for tagging beyond the range well separated by dE/dx, and to identify pions from few body decays such as $B^0 \to \pi^+\pi^-$ and $B^0 \to \rho\pi$. A new detector technology is needed to meet these goals and in the barrel region a DIRC (Detector of Internally Reflected Čerenkov radiation) is used. Čerenkov light produced in quartz bars (and the resulting ring pattern) is transferred by total internal reflection to a large water tank outside of the backward end of the magnet. The light is observed by an array of photomultiplier tubes immersed in water, where images governed by the Čerenkov angle are formed. Pattern recognition algorithm associates PMT pulses with a DCH track and a particle type determination is made. This arrangement provides at least 4 standard deviation π/K separation up to almost the kinematic limit for particles from B decays (roughly 4.5 GeV/c).

The electromagnetic calorimeter must have superb energy resolution down to very low photon energies. This is provided by a fully projective CsI(Ti) crystal calorimeter. The barrel calorimeter contains 5880 trapezoidal crystals: the endcap calorimeter contains 900 crystals. The crystal length varies from $17.5X_0$ (X_0 is the radiation length) in the forward endcap to $16X_0$ in the backward part of the barrel. Electronic noise and beam related backgrounds dominate the resolution at low photon energies, while shower leakage from the rear of the crystals dominates at higher energies.

To achieve very good momentum resolution without increasing the tracking volume, and therefore the calorimeter cost, it is necessary to have a large field of 1.5 T. The magnet is therefore of superconducting design. The magnet is similar

to many operating detector magnets, so the engineering and fabrication were relatively straightforward. The nonstandard features were the segmentation of the iron for an Instrumented Flux Return (IFR), and the complications caused by the DIRC readout in the backward region.

The IFR is designed to identify muons with momentum around 0.5 GeV/c and to detect neutral hadrons (such as K_L^0s). The magnet flux return is divided into layers between which are gaps with Resistive Plate Chambers (RPC), which serve as active detectors. The RPCs represent a proven technology which adapts well to the *BABAR* geometry.

The high data rate at PEP-II requires a data acquisition system which is more advanced than those used at previous e^+e^- experiments. The rate of all processes that are recorded at the design luminosity of 3×10^{33} cm^{-2}s^{-1} is about 100 Hz. The acceptance rate of the level 1 trigger is roughly 1.5 kHz. The bunch crossing period is 4.2 ns. Simulations of machine backgrounds show hit rates of about 100 kHz per layer in the drift chamber and about 140 MHz in the first silicon layer. The goal was to operate with negligible dead time even if the backgrounds are 10 times higher than present estimates, which did happen early in the life of the experiment.

Chapter 4

Inclusive Charmonium Production

As discussed in the overview, a comprehensive study of the inclusive production of charmonium mesons, J/ψ, $\psi(2S)$, χ_{c1} and χ_{c2}, in the *BABAR* Run 1 will be discussed in the remainder of the thesis. In an inclusive study, as opposed to an exclusive one, only the charmonium meson is reconstructed. Because of large statistics, one is able to make precise measurements of the inclusive branching fractions, such as how often a B meson decays to a channel containing a J/ψ meson, and of the properties of the reconstructed mesons. However, no information is gained about the parent B meson, or about the decay products other than the reconstructed charmonium meson.

4.1 Data Set

This analysis uses all usable data from *BABAR* Run 1. Total integrated luminosity collected on the $\Upsilon(4S)$ resonance ($\sqrt{s} = 10.58$ GeV/c) is 20.34 fb^{-1}. A fraction

of data is collected in the continuum, 50 MeV below the resonance. Integrated luminosity of the off-resonance sample is 2.61 fb^{-1}. According to the analysis of the number of produced $\Upsilon(4S)$ mesons [Hea00], the on-resonance sample has 21.26 million $B\overline{B}$ events. Systematic error on the B counting is 1.1 %.

Monte Carlo data is used to extract event and reconstruction efficiencies of the signal modes and to study various background sources. Different Monte Carlo data sets used in the analysis, and their sizes are:

- generic $B^0\bar{B}^0$, 8.6 fb^{-1}; generic B^+B^-, 9.1 fb^{-1};
- generic uds quark production, 7.5 fb^{-1};
- generic $c\bar{c}$, 7.3 fb^{-1};
- inclusive J/ψ, where the J/ψ meson is forced to decay to an electron or muon pair, 32 fb^{-1};
- inclusive $\psi(2S) \to \ell^+\ell^-$, 199 fb^{-1};
- inclusive $\psi(2S) \to \pi^+\pi^- J/\psi$, 242 fb^{-1}, generated in the same MC job as the $\ell\ell$ final state;
- inclusive χ_{c1} (51,000 events) and χ_{c2} (41,000 events), the χ_c decaying 100% to $\gamma J/\psi$, with the J/ψ decaying to an electron or muon pair;
- 42,000 single J/ψ decaying into a lepton pair, generated with a flat distribution in the cosine of the polar angle and flat center of mass momentum distribution between 0 and 4 GeV/c.

Only centrally produced [1] Monte Carlo is used and changes in experimental conditions during the run, such as the increase of drift chamber voltage and change

[1] A collaboration wide Monte Carlo production ensures the quality and consistency of the simulated data used in all analyses.

in the IFR gas mixture, are accounted for.

Lepton identification is crucial for reconstruction of charmonium states. To successfully reproduce the performance of the lepton identification selectors in data, Monte Carlo events have been processed with a standard set of particle identification tables. As a consequence, the behavior of a particle selector (a probability of accepting either a true lepton track or a fake track) is probabilistically determined based on the values obtained from very pure *control samples*. A difference in selector performance between hadronic events and generally much cleaner events in the control samples has been observed. Therefore, we use particle identification efficiencies, and systematic errors, explicitly measured in the inclusive J/ψ events. This method is discussed in detail in Section 4.5.

For the purposes of studying different signal and background contributions, Monte Carlo events are divided on the basis of generator-level information into ten different signal categories and two background categories:

- $J/\psi \rightarrow e^+e^-$ or $J/\psi \rightarrow \mu^+\mu^-$;
- $\psi(2S) \rightarrow e^+e^-$ or $\psi(2S) \rightarrow \mu^+\mu^-$;
- $\psi(2S) \rightarrow \pi^+\pi^- J/\psi$ with $J/\psi \rightarrow e^+e^-$ or $J/\psi \rightarrow \mu^+\mu^-$;
- χ_{c1} with $J/\psi \rightarrow e^+e^-$ or $J/\psi \rightarrow \mu^+\mu^-$;
- χ_{c2} with $J/\psi \rightarrow e^+e^-$ or $J/\psi \rightarrow \mu^+\mu^-$;
- $B\overline{B}$ event background;
- continuum event background.

An event may fall into more than one signal category but only one background.

As the event type is transparent to the *BABAR* event database and common analysis software, data and Monte Carlo events are processed in identical manner. Full dataset is centrally skimmed[2] and candidate events for different processes are tagged. The charmonium skim requires the B counting bit (further discussed in Section 4.2) and either an electron pair with invariant mass between 2.5 and 4.0 GeV or a muon pair with mass between 2.8 and 4.0 GeV/c. Particle identification applied at initial processing is much looser than the criteria used later in the analysis, hence there is no loss of signal due to skimming. The invariant mass is calculated after the two tracks are vertexed, using the proper particle type assignment. If the vertex fit doesn't converge, the candidate is retained but the mass is calculated from the sum of the four vectors evaluated at the origin of the detector. Candidates passing the pre-processing are stored into ntuples and further analyzed using routines to book histograms, to fit and to present the results.

4.2 Event Selection

For the most part, this analysis uses the standard *BABAR* hadronic event selection, optimized to accept $B\overline{B}$ events and reject continuum background. The exception is the analysis of J/ψ production in the continuum, where the event selection is loosened. Briefly, the requirements on the event are:

- Level 3 trigger accept: DCH [3] or EMC [4];

[2]A process by which events containing a particular feature are pre-selected.

[3]Requires a pair of short back-to-back tracks *and* either 3 long tracks *or* 1 long track and 1 high momentum track.

[4]Requires 2 energetic clusters *or* 1 energetic cluster and two back-to-back minimum ionizing clusters *or* two back-to-back intermediate energy clusters *or* 4 minimum ionizing clusters *or* 3 minimum ionizing clusters, 2 of which are back-to-back.

- at least 3 good tracks [5] in fiducial volume, $0.41 < \theta < 2.54$, where θ is the polar angle of the track [6];
- ratio, R2, of the second Fox-Wolfram moment to the zeroth, calculated from a list of charged and neutral candidates in the fiducial volume, $R2All < 0.5$;
- Total energy, charged + neutral, in the fiducial volume $ETotFid > 4.5$ GeV/c;
- Transverse distance between primary vertex and measured beam spot: $\sqrt{\Delta_x^2 + \Delta_y^2} <$ 0.5 cm;
- Longitudinal distance between primary vertex and measured beam spot: $|\Delta_z| < 6$ cm.

The vertex is calculated from the charged tracks in the fiducial region. The selection is highly efficient for $B\overline{B}$ events: $\epsilon_{BB} = 0.954$.

In addition, all events containing a $\psi \rightarrow e^+e^-$ in the final state are required to have at least 5 charged tracks in the fiducial volume. This cut greatly reduces radiative Bhabha events in which a photon has converted and thus produced a final state with 4 charged tracks, including high energy electrons.

Branching fraction calculations other than $\mathcal{B}(\psi(2S) \rightarrow \ell^+\ell^-)$ include the ratio of the number of produced signal events to the number of $B\overline{B}$ events. Thus, we calculate either the event efficiency for a final state or the ratio of $B\overline{B}$ event efficiency to the event efficiency of a given signal mode. Calculations are done using generic $B\overline{B}$ and inclusive signal Monte Carlo events, separately for electron and muon final states. The results are presented in Table 4.1. A systematic error of 1.1%, common to all on-resonance final states, is obtained from the efficiency

[5] Good tracks have momentum < 10 GeV/c, transverse momentum > 0.1 GeV/c, at least 12 DCH wires hit, distance of closest approach to the origin < 1.5 cm in xy and < 10.0 cm in z.

[6] This angular region corresponds to the acceptance of the electro-magnetic calorimeter.

Table 4.1: Summary of the event selection efficiencies for all signal modes. Either signal event efficiency itself or the ratio of $B\overline{B}$ efficiency to signal efficiency is shown, as appropriate.

Final State	Efficiency	Electrons	Muons
$J/\psi \to \ell\ell$	$\epsilon_{B\overline{B}}/\epsilon_{\rm charmonium}$	1.023	0.993
$J/\psi \to \ell\ell$, continuum	$\epsilon_{\rm charmonium}$	0.892	0.892
$\psi(2S) \to \ell^+\ell^-$	$\epsilon_{\rm charmonium}$	0.912	0.945
$\psi(2S) \to \ell^+\ell^-$	$\epsilon_{B\overline{B}}/\epsilon_{\rm charmonium}$	1.047	1.010
$\psi(2S) \to \pi^+\pi^- J/\psi$	$\epsilon_{\rm charmonium}$	0.967	0.972
$\psi(2S) \to \pi^+\pi^- J/\psi$	$\epsilon_{B\overline{B}}/\epsilon_{\rm charmonium}$	0.987	0.982
$\chi_{c1} \to \gamma J/\psi$	$\epsilon_{B\overline{B}}/\epsilon_{\rm charmonium}$	1.041	1.000
$\chi_{c2} \to \gamma J/\psi$	$\epsilon_{B\overline{B}}/\epsilon_{\rm charmonium}$	1.035	0.997

variation with different Monte Carlo conditions and by varying the requirement on the number of good tracks in the fiducial volume. As discussed in Section 4.10, a 7.2% systematic is assigned to the looser event efficiency of the inclusive J/ψ events produced in the continuum.

4.3 Meson Reconstruction

Some reconstruction features are common to all final states. The following charged tracks and photon selection is used in meson reconstruction:

- lepton candidates are good tracks in the fiducial volume;
- photon candidates must pass initial good photon selection [7] and lie in the

[7] Good photons are EMC clusters not matched to a charged track, with at least 30 MeV of

fiducial volume;

- pions are charged tracks in a slightly wider angular region, $0.41 < \theta < 2.54$.

A Bremsstrahlung recovery algorithm is used to add radiated photons to the electron tracks and obtain a more accurate measure of their momentum and energy. It provides increased efficiency in the final states involving $\psi \to e^+e^-$. This is particularly important for modes with limited statistics, such as χ_c production or J/ψ production in the continuum. Furthermore, it allows us to improve signal to background ratio by using a tighter J/ψ invariant mass window when reconstructing $\psi(2S)$ and χ_c mesons. A complete study of the Bremsstrahlung recovery algorithm is presented in Section 4.4.3.

4.3.1 $J/\psi \to \ell\ell$ Reconstruction

J/ψ candidates are selected from pairs of leptons satisfying the following criteria:

- One track must satisfy 'very tight' electron identification criteria while the other track must satisfy 'tight' electron criteria, or one track must satisfy 'tight' muon identification criteria and the other must satisfy 'loose' muon criteria. Discussion of lepton identification at *BABAR*, including definitions of standard selection criteria, is deferred to Section 4.5.1. Our lepton selection was optimized by minimizing the relative statistical error in the on-resonance Monte Carlo cocktail. The cocktail includes generic $B\overline{B}$ events, continuum events and inclusive signal events mixed in the appropriate ratios.

- Candidate mass must fall in one of the following regions: $2.5 < m(J/\psi \to e^+e^-) < 3.3$ GeV/c, $2.8 < m(J/\psi \to \mu^+\mu^-) < 3.3$ GeV/c. The tracks are

measured energy and the lateral [D$^+$85] shower shape parameter less than 0.8.

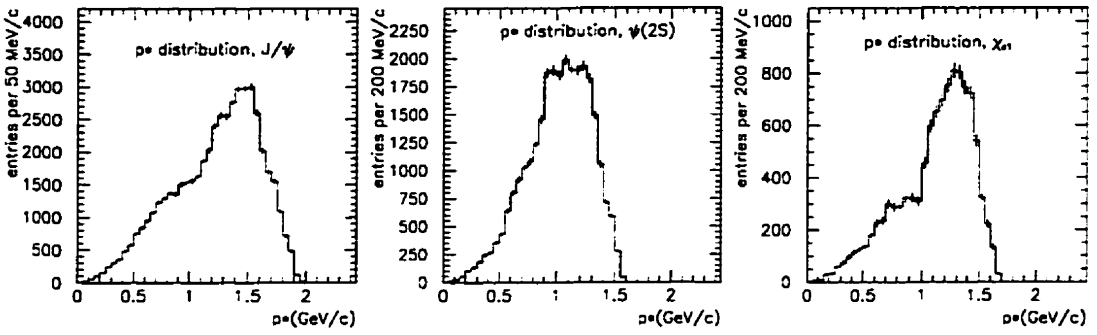

Figure 4.1: Reconstructed Monte Carlo p^* distributions for (a) J/ψ, (b) $\psi(2S)$ and (c) χ_{c1} mesons.

vertexed using only a geometric constraint and the fitted mass is used. If the fit fails to converge, the candidate mass is calculated from the sum of four-vectors.

- The magnitude of the center of mass momentum of the candidate is limited to a region kinematically allowed for the J/ψ mesons from B decays: $p^* < 2.0$ GeV/c. The cut rejects the continuum events and the combinatoric background. A negligible fraction of Monte Carlo J/ψ candidates (0.03%) fails this cut because of the wrong assignment of the Bremsstrahlung photon (Figure 4.1). Clearly, this restriction is lifted when studying J/ψ production in the continuum.

- J/ψ candidates used for reconstructing $\psi(2S) \to \pi^+\pi^- J/\psi$ and $\chi_c \to \gamma J/\psi$ decays are selected from a tighter mass window: $3.05 < m(J/\psi \to e^+e^-) < 3.12$ GeV/c^2, $3.07 < m(J/\psi \to \mu^+\mu^-) < 3.12$ GeV/c^2. The values are selected by minimizing the relative statistical error on the number of reconstructed J/ψ mesons in B decays, after continuum subtraction. As our continuum Monte Carlo generator does not include proper J/ψ production mechanisms, this optimization is performed on data. The optimization curves are smooth, with wide minima, indicating that we are not introducing

a bias due to statistical fluctuations in the data sample.

4.3.2 $\psi(2S) \to \ell^+\ell^-$ Reconstruction

$\psi(2S) \to \ell^+\ell^-$ candidates are selected in a manner similar to $J/\psi \to \ell\ell$. The differences are:

- The mass window is the same for electron and muon modes: $3.4 < m(\psi(2S) \to \ell^+\ell^-) < 4.0$ GeV/c^2.
- Kinematically allowed region for center of mass momentum is reduced to $p^* < 1.6$ GeV/c. Again, the cut is virtually 100% efficient while eliminating a considerable background.

4.3.3 $\psi(2S) \to \pi^+\pi^- J/\psi$ Reconstruction

$\psi(2S) \to \pi^+\pi^- J/\psi$ candidates are selected according to the following:

- A J/ψ candidate is taken from the tight mass window.
- A pair of oppositely charged pion candidates must have an invariant mass, calculated using the two momenta, in the $0.45 < m(\pi^+\pi^-) < 0.6$ GeV/c^2 range (Figure 4.2). This value was optimized on Monte Carlo and cross-checked against the distribution measured by the BES experiment [B+01].
- The probability of the χ^2 of the vertex fit (geometric constraints only) to the four charged tracks must be larger than 1%.
- $p^* < 1.6$ GeV/c, as for the lepton modes.

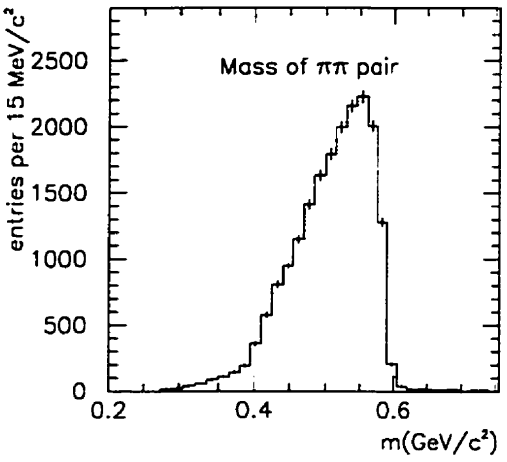

Figure 4.2: Mass of the pion pair in $\psi(2S) \rightarrow \pi^+\pi^- J/\psi$ decays in Monte Carlo.

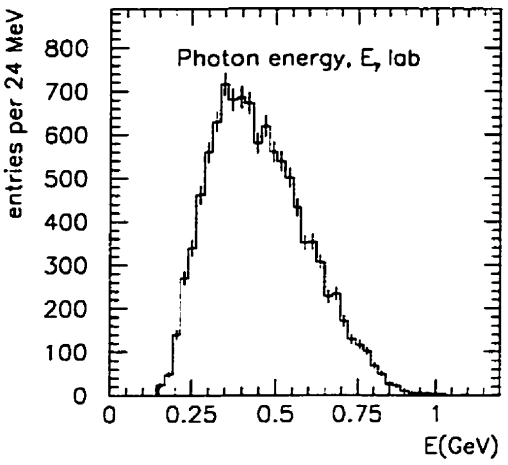

Figure 4.3: Energy (lab) of the photon in Monte Carlo $\chi_{c1} \rightarrow \gamma J/\psi$ decays.

The effect of the mass resolution, particularly due to Bremsstrahlung in the electron final state, is reduced by plotting the mass difference between $\psi(2S)$ and its J/ψ daughter rather than the $\psi(2S)$ invariant mass distribution.

4.3.4 $\chi_c \rightarrow \gamma J/\psi$ Reconstruction

A χ_c candidate is formed by vertexing a J/ψ candidate from a tight mass window with a photon candidate. This procedure reevaluates the photon four-momentum assuming it originated from the J/ψ vertex rather than from the origin, thus improving its energy and three-momentum measurement. In addition to standard good photon selection, we impose the following conditions:

- The Zernike moment, A_{42} [8] [SV97] must be less than 0.15. This value is selected to give high efficiency in Monte Carlo.

[8] Provides a shower shape description independent of the local coordinate system. A_{42} is the lowest moment reflecting the angular variation of the shower shape.

- The photon cannot come from a π^0 candidate with a mass in the $0.117 < m(\pi^0) < 0.147$ GeV/c^2 region, corresponding to $(-3\sigma, 2\sigma)$ range. These values are deemed reasonable and were not optimized.

- Photon energy must be between 0.15 and 1.0 GeV (Figure 4.3). The values are selected to be highly efficient for Monte Carlo signal and have not been optimized.

- Hadronic split-offs are reduced by requiring a minimal angular displacement of 9° between the photon and the closest charged track, at the face of the EMC. This value roughly corresponds to the spatial separation of three times the Moliere radius for Cesium Iodide.

Again, we plot the mass difference between a χ_c candidate and its J/ψ daughter.

4.4 Signal Extraction

The branching fraction for a B meson to decay into a charmonium meson ψ is related to the number of reconstructed ψ mesons by:

$$\mathcal{B} = \frac{N_\psi}{\epsilon_R^\psi \cdot 2 \cdot N_{BB}} \cdot \frac{\epsilon_{BB}}{\epsilon_E^\psi}, \tag{4.1}$$

where:

- N_ψ is the number of reconstructed charmonium mesons extracted from a fit to a mass or a mass difference plot.

- ϵ_R^ψ is the reconstruction efficiency, the fraction of the charmonium mesons in the events passing the event selection that are measured by the fit. It includes both cut efficiencies and secondary branching fractions to the final states involved.

- $N_{B\overline{B}}$ is the number of $B\overline{B}$ events in *BABAR* Run 1 passing the B counting selection.
- ϵ_E^{ψ} is the efficiency for a $B\overline{B}$ event containing a charmonium meson to pass the event selection.
- $\epsilon_{B\overline{B}}$ is the efficiency for a generic $B\overline{B}$ event to pass the event selection.

Each of these items is discussed in the remainder of the thesis.

4.4.1 Fitting Procedure

Histogram fitting is done using MINUIT[9] with the likelihood option. All fits converge and have an accurate error matrix.

The number of charmonium mesons is extracted by fitting a mass or a mass difference plot to a signal shape probability density function (PDF) derived from Monte Carlo. The background is modeled by a third order Chebychev polynomial. To account for energy scale and resolution differences between Monte Carlo and data an additional offset (δ) and a Gaussian smearing (σ) are convoluted with the PDF. This is done within the fitting procedure so that values of δ and σ can be extracted from the fit.

The PDFs are created by applying the selection criteria to Monte Carlo events and, in addition, requiring that a reconstructed candidate be matched to a generator level 'truth' information. This ensures that the PDF is defined by signal shape only. The PDFs (Figures 4.4 to 4.7) are stored in histograms with a 1 MeV bin width.

[9]Function minimization and error analysis software written at CERN, Switzerland.

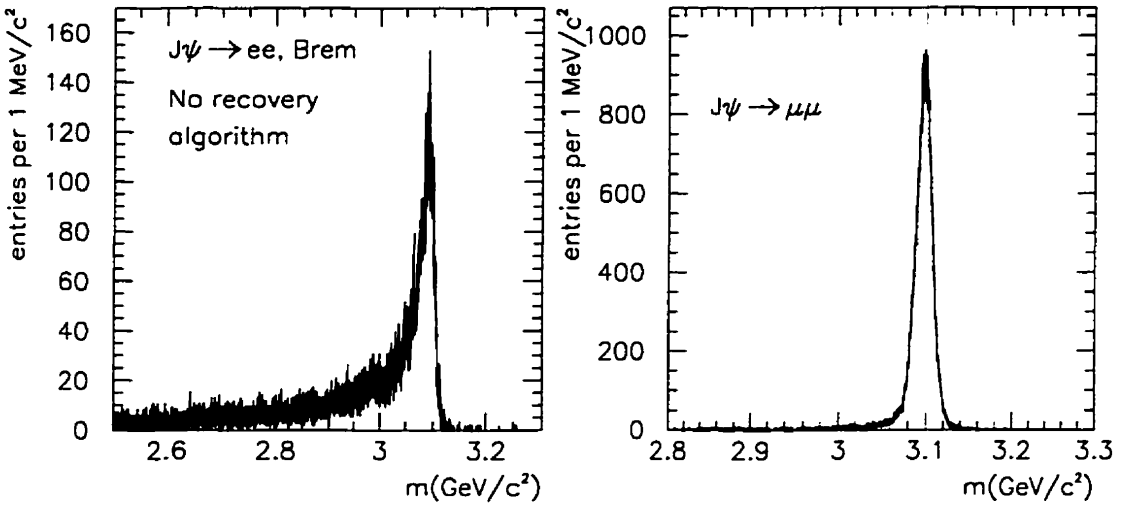

Figure 4.4: PDFs for measured mass in $J/\psi \to e^+e^-$, undergoing Bremsstrahlung (left) and $J/\psi \to \mu^+\mu^-$ (right), without the Bremsstrahlung recovery algorithm applied.

At the time of fitting, the offset and smearing are convoluted and the resulting PDF is rebinned to have bin width identical to the mass (or mass difference) histogram being fit. This is typically 5 or 10 MeV. The PDF is normalized to unit area. The number of signal events in the histogram bin j is:

$$N_j = \text{NsigHist} \times e_j / \sum_j e_j. \tag{4.2}$$

where NsigHist is the total signal yield in the histogram range and e_j is the value of the normalized PDF after the offset (δ) and the smearing (σ) have been incorporated. It is obtained from the original 1 MeV binned distribution as:

$$e_j = \sum_i 0.5 \cdot a_i \left[\text{erf}\left((x_{j+1} - x_i - \delta)/\sqrt{2}\sigma\right) - \text{erf}\left((x_j - x_i - \delta)/\sqrt{2}\sigma\right) \right]. \tag{4.3}$$

where x_i is the central value of the i-th bin and a_i is the corresponding number of entries.

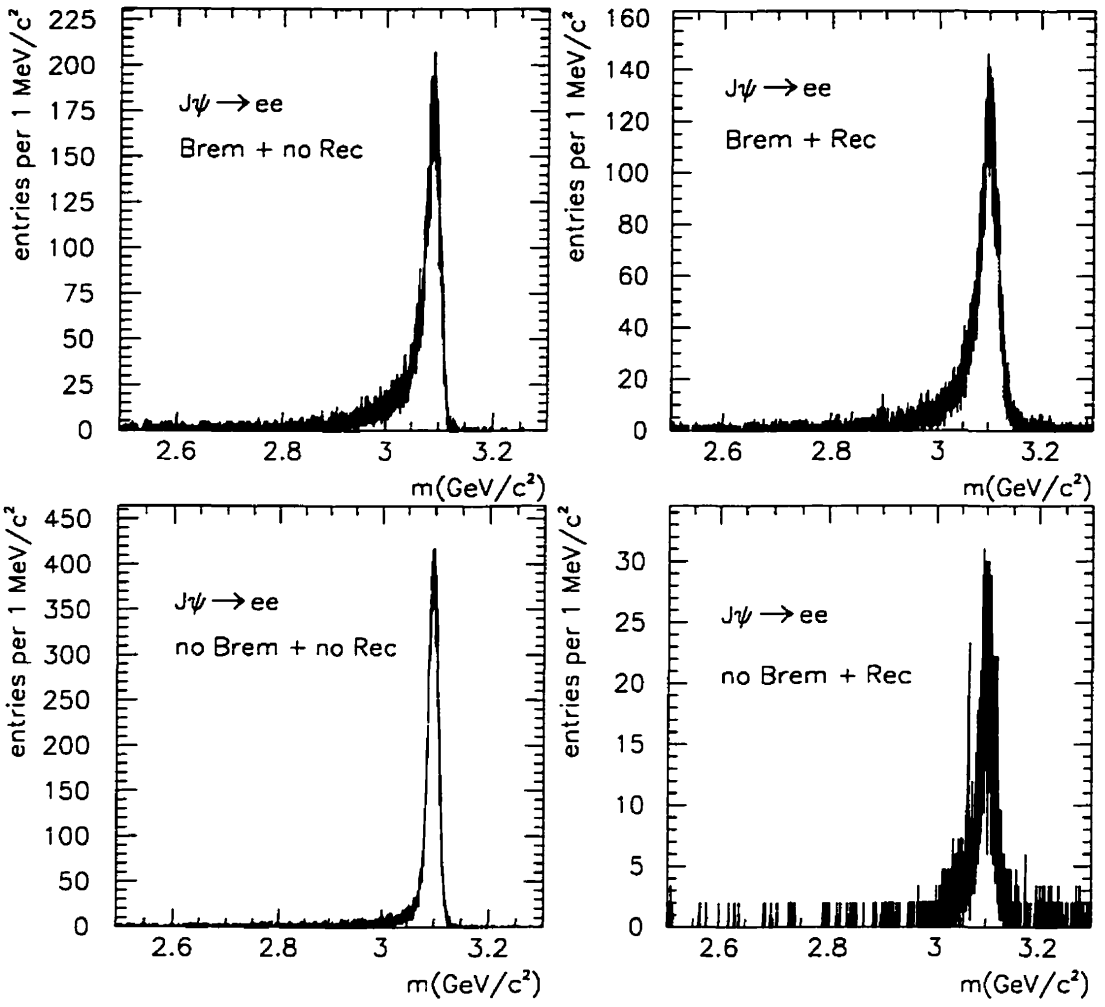

Figure 4.5: PDFs for measured mass in $J/\psi \rightarrow e^+e^-$ decays when Bremsstrahlung recovery algorithm is used. (a) $J/\psi \rightarrow e^+e^-$ in which an electron undergoes Bremsstrahlung but no photon is recovered; (b) $J/\psi \rightarrow e^+e^-$ in which an electron undergoes Bremsstrahlung and a photon is recovered; (c) $J/\psi \rightarrow e^+e^-$ in which no electron undergoes Bremsstrahlung and no photon is recovered; and (d) $J/\psi \rightarrow e^+e^-$ in which no electron undergoes Bremsstrahlung but a photon is recovered.

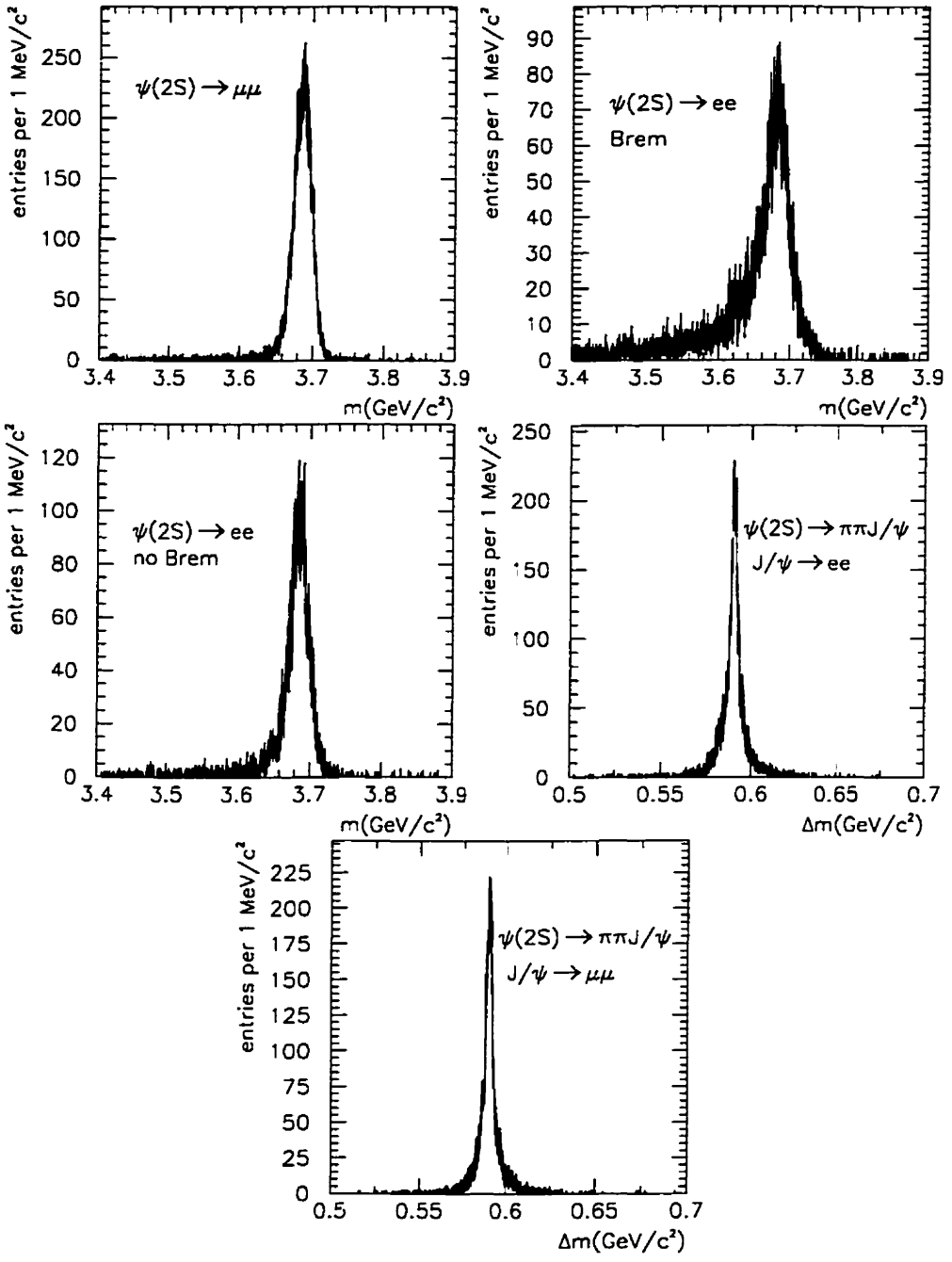

Figure 4.6: PDFs for measured mass in $\psi(2S)$ decays for (a) $\psi(2S) \to \mu^+\mu^-$; (b) $\psi(2S) \to e^+e^-$, electron undergoes Bremsstrahlung; (c) $\psi(2S) \to e^+e^-$, no Bremsstrahlung. Mass differences in $\psi(2S) \to \pi^+\pi^- J/\psi$ candidates for (d) $J/\psi \to e^+e^-$; (e) $J/\psi \to \mu^+\mu^-$.

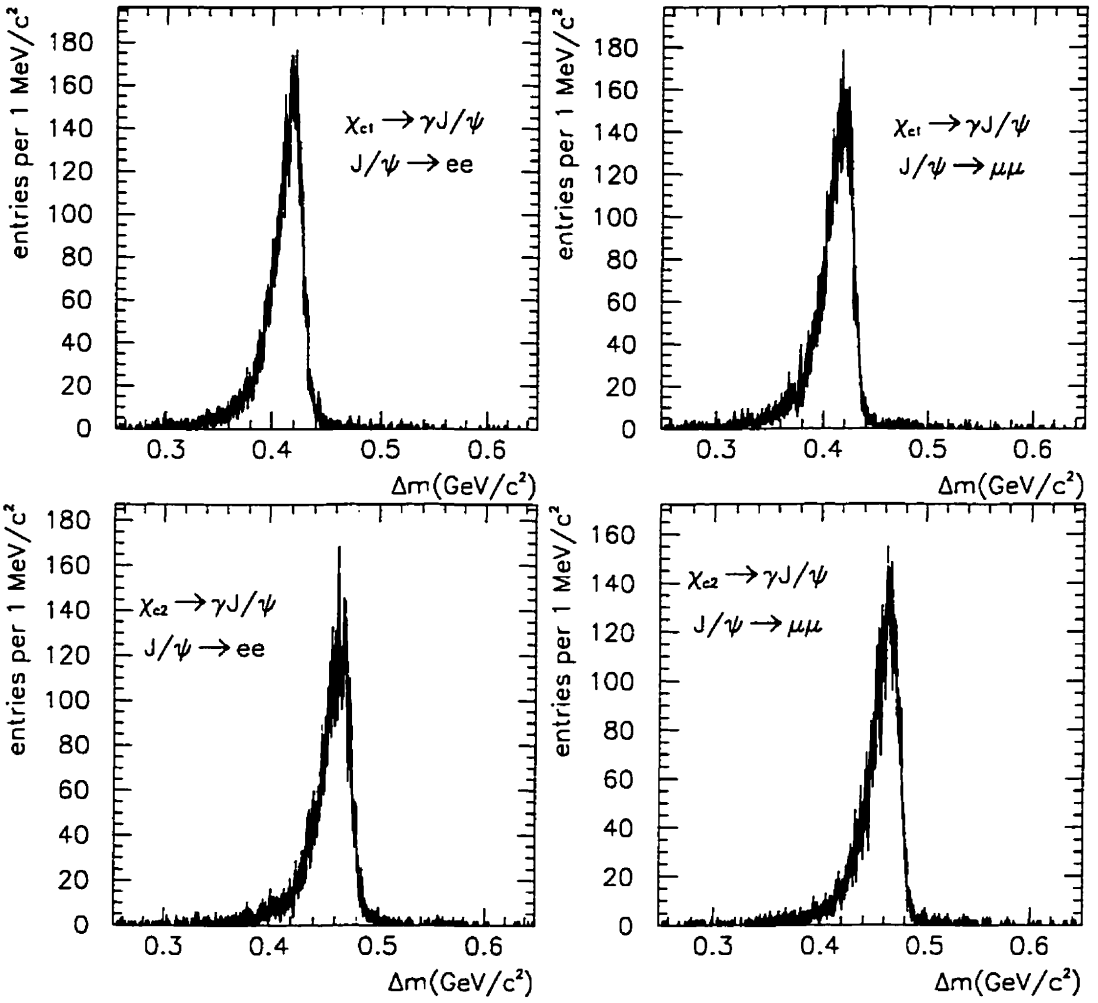

Figure 4.7: PDFs for measured mass difference between χ_c and J/ψ for (a) χ_{c1}, $J/\psi \to e^+e^-$; (b) χ_{c1}, $J/\psi \to \mu^+\mu^-$; (c) χ_{c2}, $J/\psi \to e^+e^-$; (d) χ_{c2}, $J/\psi \to \mu^+\mu^-$.

4.4.2 Fit Parameters

The number of signal events and four background parameters (for the third order Chebychev polynomial) are allowed to float in all fits. Fits to the χ_c distributions are slightly distinct as, due to experimental resolution, χ_{c1} and χ_{c2} signal region overlap. Thus, yields for both mesons are extracted from a single mass difference histogram. Electron and muon decay modes of the intermediate J/ψ are still kept separate. There is no constraint on the ratio of χ_{c1} to χ_{c2} yields. To minimize the statistical error we constrain other fit parameters in the following way:

Offset and smearing extracted from the on-resonance $J/\psi \to \mu^+\mu^-$ fit, $\delta = -3.00 \pm 0.15$ MeV/c^2 and $\sigma = 7.79 \pm 0.22$ MeV/c^2, are used for all other $\psi \to \ell^+\ell^-$ fits, both on and off-resonance. As these quantities reflect tracking differences between data and Monte Carlo, they should be comparable for the two lepton modes. Effect of Bremsstrahlung on the difference in mass resolution between data and Monte Carlo is not significant. Observed degradation of the photon energy resolution by 1.5% does not affect the J/ψ mass resolution.

Offset and smearing in the off-resonance $\psi(2S) \to \pi^+\pi^- J/\psi$ fits are fixed to the values obtained in the on-resonance fits.

Offset and smearing in the χ_{c1} and χ_{c2} fits, both on-resonance and off-resonance are fixed to the values obtained from the fit to a mass difference (χ_{c1}-J/ψ) distribution of fully reconstructed $B^+ \to \chi_{c1} K^+$ decays (Figure 4.8)

The inclusive χ_{c1} sample is five times larger than the fully reconstructed $B^+ \to \chi_c K^+$. So, to a good approximation, it can be treated as statistically independent. The same parameters, $\delta = 2.9 \pm 2.0$ MeV/c^2 and $\sigma = 9.2 \pm 2.5$ MeV/c^2, are relevant for all four final states because, in this case, resolution is dominated by the photon. This is seen by comparing the resolution to $\psi(2S) \to \pi^+\pi^- J/\psi$ which also uses

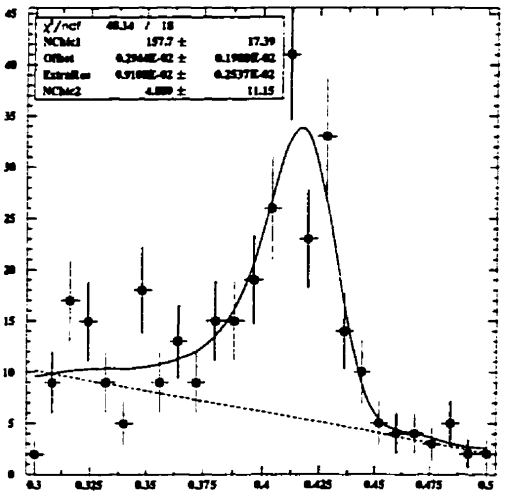

Figure 4.8: Fit to mass difference in reconstructed $B^+ \to \chi_c K^+$ candidates (e^+e^- and $\mu^+\mu^-$ combined) using the fit method described.

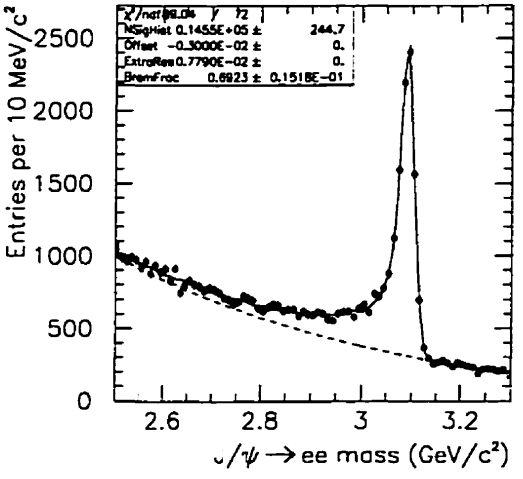

Figure 4.9: Fit to $J/\psi \to e^+e^-$, reconstructed without using Bremsstrahlung recovery algorithm. This information is used to extract the true fraction of J/ψ mesons accompanied by Bremsstrahlung.

the mass difference with the J/ψ daughter.

Bremsstrahlung related parameters are the topic of the following section.

4.4.3 Bremsstrahlung

The amounts of Bremsstrahlung observed in data and in Monte Carlo are significantly different. The difference results from the detector model used in Monte Carlo. The model underestimates the amount of material in the inner layers of *BABAR*. For instance, SVT electronics are not present in the model. We resolve the problem by explicitly including the amount of Bremsstrahlung into the $\psi \rightarrow e^+e^-$ fits.

The Bremsstrahlung fraction (B) is extracted by fitting the mass distribution of $J/\psi \rightarrow e^+e^-$ candidates reconstructed *without* using the Bremsstrahlung recovery algorithm. (Figure 4.9.) Studies show this fit is most sensitive to the true amount of Bremsstrahlung. This is the only instance in which the recovery algorithm is turned off. The PDF is a combination of the two components, one for electrons undergoing Bremsstrahlung and the other for the electrons not undergoing Bremsstrahlung, explicitly writen as:

$$f(m) = B \cdot f_B(m) + (1 - B) \cdot f_{\overline{B}}(m), \tag{4.4}$$

where B is the fraction of J/ψ in the mass window with at least one daughter electron undergoing Bremsstrahlung, $f_B(m)$ and $f_{\overline{B}}(m)$ are the PDFs for the Bremsstrahlung (Figure 4.4) and no-Bremsstrahlung (Figure 4.5) component respectively, and $f(m)$ is the combined $J/\psi \rightarrow e^+e^-$ PDF.

The true fraction of J/ψ mesons with an electron daughter undergoing Brems-

strahlung, B^0, is related to B by:

$$B^0 = \frac{\frac{B}{\epsilon_{M,B}}}{\frac{B}{\epsilon_{M,B}} + \frac{(1-B)}{\epsilon_{M,\overline{B}}}}, \tag{4.5}$$

where $\epsilon_{M,B} = 0.812 \pm 0.003$ ($\epsilon_{M,\overline{B}} = 0.949 \pm 0.002$) is the probability that a Bremsstrahlung (no-Bremsstrahlung) J/ψ [10] has invariant mass in the histogram window.

The fit to $J/\psi \rightarrow e^+e^-$ (Figure 4.9) on-resonance data yields $B = 0.692 \pm 0.015$, corresponding to $B^0 = 0.724 \pm 0.016$. Monte Carlo studies yield $B^0 = 0.580 \pm 0.003$, demonstrating that the model of *BABAR* used in the Monte Carlo does underestimate the amount of detector material. If Bremsstrahlung recovery is not used, the fraction of $J/\psi \rightarrow e^+e^-$ in the histogram window is:

$$\epsilon_M = B^0 \cdot \epsilon_{M,B} + (1 - B^0) \cdot \epsilon_{M,\overline{B}} = 0.850 \pm 0.002. \tag{4.6}$$

When a J/ψ daughter emits a photon, which usually occurs before the DCH, measurement of the momentum by the tracking system is lower than the true electron momentum, thus creating a long radiative tail in the $J/\psi \rightarrow e^+e^-$ invariant mass distribution. A Bremsstrahlung recovery algorithm is used to associate the photon with the electron track and obtain a better measurement of the particle momentum. At emission, direction of Bremsstrahlung photons is close to the direction of the parent track but the strong DCH magnetic field produces sufficient azimuthal separation between photon's and electron's showers in the EMC. Moreover, $e^{\pm}$ tracks are deflected in opposite directions with respect to the radiated photon. Using track direction at the origin, (θ_0^e, ϕ_0^e), angular position of the centroid of the associated EMC shower, (θ_c^e, ϕ_c^e), and angular position of the photon shower centroid, $(\theta_0^\gamma, \phi_0^\gamma)$, Bremsstrahlung photons are selected in the following way:

[10] A Bremsstrahlung J/ψ is one with at least one daughter electron undergoing Bremsstrahlung.

- $|\theta_0^\gamma - \theta_0^e| < 35$ mrad. There is no expected polar displacement between Bremsstrahlung photons and the track. This cut is very efficient for Bremsstrahlung photons and reduces the effect of fake photons.

- $(\phi_0^{e^-} - 50)$ mrad $< \phi_0^\gamma < \phi_c^{e^-}$ *or* $\phi_c^{e^+} < \phi_0^\gamma < (\phi_0^{e^+} + 50)$ mrad. The allowed ϕ window is momentum dependent and it is optimized to reduce sensitivity to fake Bremsstrahlung photons.

All photons passing the above selection are added to the electron tracks and the four-momentum of the candidate is recalculated. Full description of the recovery algorithm is presented in [F+01].

With the Bremsstrahlung recovery algorithm turned on, it is insufficient to consider only two PDFs. We divide the signal into four categories depending on whether either of the J/ψ electrons undergoes Bremsstrahlung and whether the recovery algorithm associates a photon with either of the electrons. Note that, because of random background, recovery algorithm can add a photon to a electron that did not radiate. The PDF is constructed from four components as:

$$\begin{aligned} f(m) &= B' \cdot B_R \cdot f_{BR}(m) + B' \cdot (1 - B_R) \cdot f_{B\overline{R}}(m) \\ &\quad + (1 - B') \cdot (1 - B_E) \cdot f_{\overline{BE}}(m) + (1 - B') \cdot B_E \cdot f_{\overline{B}E}(m), \end{aligned} \quad (4.7)$$

where the four PDFs are: $f_{BR}(m)$ - Bremsstrahlung J/ψ with a recovered photon, $f_{B\overline{R}}(m)$ - Bremsstrahlung J/ψ without a recovered photon, $f_{\overline{B}E}(m)$ - non-Bremsstrahlung J/ψ with a recovered photon, and $f_{\overline{BE}}(m)$ - non-Bremsstrahlung J/ψ without a recovered photon. Probabilities for J/ψ candidates in the four categories to be in the mass window are calculated from Monte Carlo: $\epsilon_{M,BR} = 0.948 \pm 0.002$, $\epsilon_{M,B\overline{R}} = 0.922 \pm 0.003$, $\epsilon_{M,\overline{BE}} = 0.969 \pm 0.002$ and $\epsilon_{M,\overline{B}E} = 0.929 \pm 0.007$. The parameters used to combine the PDFs are:

- B_E is the error rate. It is the probability that a photon is added to a non-

Bremsstrahlung J/ψ. As it depends purely on distribution of background photons, which is well simulated, this parameter is fixed to the Monte Carlo value of 0.093.

- B_R is the recovery fraction. It is the fraction of Bremsstrahlung J/ψ which have an associated photon. We do not distinguish whether the correct photon is added. The on-resonance $J/\psi \to e^+e^-$ fit returns $B_R = 0.395 \pm 0.027$, compared to the Monte Carlo value of 0.464 ± 0.005. The value is fixed for all further $\psi \to e^+e^-$ fits.

- B' is the fraction of Bremsstrahlung $J/\psi \to e^+e^-$ in the mass window. It is related to true Bremsstrahlung fraction, B^0, by:

$$B^0 = \frac{\frac{B' \cdot B_R}{\epsilon_{M,BR}} + \frac{B' \cdot (1-B_R)}{\epsilon_{M,B\overline{R}}}}{\frac{B' \cdot B_R}{\epsilon_{M,BR}} + \frac{B' \cdot (1-B_R)}{\epsilon_{M,B\overline{R}}} + \frac{(1-B') \cdot (1-B_E)}{\epsilon_{M,\overline{BE}}} + \frac{(1-B') \cdot B_E}{\epsilon_{M,\overline{B}E}}}. \tag{4.8}$$

  In the fit to Bremsstrahlung recovered $J/\psi \to e^+e^-$ mass distribution B^0 is fixed to the value found by the no-recovery fit. In each iteration B' is calculated using current values of B_E and B_R.

The overall efficiency for a Bremsstrahlung recovered J/ψ to be reconstructed in the mass window is:

$$\begin{aligned} \epsilon_m &= B^0 \cdot B_R \cdot \epsilon_{M,BR} + B^0 \cdot (1 - B_R) \cdot \epsilon_{M,B\overline{R}} \\ &\quad + \left(1 - B^0\right) \cdot (1 - B_E) \cdot \epsilon_{M,\overline{BE}} + \left(1 - B^0\right) \cdot B_E \cdot \epsilon_{M,\overline{B}E} \\ &= 0.941 \pm 0.002. \end{aligned} \tag{4.9}$$

The corresponding Monte Carlo value, without any corrections, is 0.955 ± 0.001.

The Bremsstrahlung recovery algorithm increases the number of $J/\psi \to e^+e^-$ events reconstructed in the mass window by 8.2%. Narrower mass distribution allows us to decrease the mass range for J/ψ used in $\psi(2S)$ and χ_c reconstruction without a signal loss. The primary benefit, however, is the reduction in statistical

uncertainty resulting from continuum subtraction. The effects of the recovery algorithm can be clearly observed by comparing $J/\psi \to e^+e^-$ mass distributions without (Figure 4.9) and with (Figure 4.10 (a)) the algorithm turned on. The yields (NsigHist, as in Equation 4.2) corrected for mass efficiency are consistent for the two cases: NsigHist$/\epsilon_M = 16,773 \pm 330$ with Bremsstrahlung recovery, $17,124 \pm 743$ without.

Recovery is also used for $\psi(2S) \to e^+e^-$ decays. Because of significantly lower statistics in that mode it is sufficient to consider only two PDFs: $\psi(2S)$accompanied by Bremsstrahlung and $\psi(2S)$not accompanied by Bremsstrahlung.

4.4.4 Fit Results

Fits are performed for all eight final states in both on and off-resonance data. The number of reconstructed charmonium mesons coming from B decays is the number in on-resonance data events minus the number in off-resonance data events rescaled to the same luminosity. Because of slightly different selection, separate fits are done to extract J/ψ signal yield in the continuum, as discussed in Section 4.10.

Fits to the on-resonance sample are shown in Figures 4.10 to 4.12. Fit parameters and yields are summarized in Tables 4.2 and 4.3.

4.4.5 Fit Systematics

Several contributions to the fit systematic error are discussed in this section. The most important test is the verification of the signal yield in the Monte Carlo sample. It has been performed for all final states. Other, less significant components have been studied in $J/\psi \to \ell^+\ell^-$ modes only. This is reasonable as inclusive J/ψ signal has much larger statistics and the measurement is systematics dominated.

Table 4.2: Fit parameters for the inclusive modes. "On" and "Off" refer to on or off-resonance. Offset and smearing are in MeV. Parameters without uncertainties are fixed in the fit. B^0 is the fraction of all $J/\psi \to e^+e^-$ mesons with Bremsstrahlung; the actual fit parameter is the fraction in the histogram mass window, $B = 0.692 \pm 0.015$. B_R is the Bremsstrahlung-recovery fraction; the Bremsstrahlung fake rate, B_E is fixed to 0.093 for all e^+e^- fits with Bremsstrahlung-recovery.

Mode		*Offset*	*Smearing*	B^0	B_R
$J/\psi(p^* < 2.0)$					
$\mu^+\mu^-$	on	-3.00±0.15	7.79±0.22		
$\mu^+\mu^-$	off	-3.00	7.79		
e^+e^-(no B.R.)	on	-3.00	7.79	0.724±0.016	
e^+e^-	on	-3.00	7.79	0.724	0.395±0.027
e^+e^-	off	-3.00	7.79	0.724	0.395
$\psi(2S)(p^* < 1.6)$					
$\mu^+\mu^-$	on	-3.00	7.79		
$\mu^+\mu^-$	off	-3.00	7.79		
e^+e^-	on	-3.00	7.79	0.724	0.395
e^+e^-	off	-3.00	7.79	0.724	0.395
$\mu^+\mu^-\pi^+\pi^-$	on	-1.64±0.36	1.70±0.51		
$\mu^+\mu^-\pi^+\pi^-$	off	-1.64	1.70		
$e^+e^-\pi^+\pi^-$	on	-2.16±0.46	2.13±0.70		
$e^+e^-\pi^+\pi^-$	off	-2.16	2.13		
$\chi_{c1}(p^* < 1.7)$					
$\mu^+\mu^-\gamma$	on	2.9	9.1		
$\mu^+\mu^-\gamma$	off	2.9	9.1		
$e^+e^-\gamma$	on	2.9	9.1		
$e^+e^-\gamma$	off	2.9	9.1		
$\chi_{c2}(p^* < 1.7)$					
$\mu^+\mu^-\gamma$	on	2.9	9.1		
$\mu^+\mu^-\gamma$	off	2.9	9.1		
$e^+e^-\gamma$	on	2.9	9.1		
$e^+e^-\gamma$	off	2.9	9.1		
J/ψ Continuum					
$\mu^+\mu^-$	off	-3.00	7.79		
e^+e^-	off	-3.00	7.79	0.724	0.395
$\mu^+\mu^-$, $p^* > 2$	on	-3.00	7.79		
e^+e^-, $p^* > 2$	on	-3.00	7.79	0.724	0.395

Table 4.3: Yields for the inclusive modes. "On" and "Off" refer to on or off-resonance. The uncertainty on the continuum-subtracted yield for $J/\psi \to e^+e^-$ includes an additional 1.2% found by varying fit parameters.

Mode		*Yield*	*Cont. Sub.*
$J/\psi\,(p^* < 2.0)$			
$\mu^+\mu^-$	on	13683±154	13161±208
$\mu^+\mu^-$	off	67± 18	
e^+e^-(no B.R.)	on	14553±245	
e^+e^-	on	15739±171	15575±293
e^+e^-	off	21± 16	
$\psi(2S)(p^* < 1.6)$			
$\mu^+\mu^-$	on	437±44	398±96
$\mu^+\mu^-$	off	5±11	
e^+e^-	on	552±50	552±59
e^+e^-	off	0± 4	
$\mu^+\mu^-\pi^+\pi^-$	on	400±34	392±41
$\mu^+\mu^-\pi^+\pi^-$	off	1± 3	
$e^+e^-\pi^+\pi^-$	on	405±37	405±40
$e^+e^-\pi^+\pi^-$	off	0± 2	
$\chi_{c1}(p^* < 1.7)$			
$\mu^+\mu^-\gamma$	on	545±58	545±60
$\mu^+\mu^-\gamma$	off	0± 2	
$e^+e^-\gamma$	on	471±54	471±71
$e^+e^-\gamma$	off	0± 6	
$\chi_{c2}(p^* < 1.7)$			
$\mu^+\mu^-\gamma$	on	135±46	104±56
$\mu^+\mu^-\gamma$	off	4± 4	
$e^+e^-\gamma$	on	86±44	86±59
$e^+e^-\gamma$	off	0± 5	
J/ψ Continuum			
$\mu^+\mu^-$	off	156 ± 25	
e^+e^-	off	121 ± 26	
$\mu^+\mu^-$, $p^* > 2$	on	879 ± 52	
e^+e^-, $p^* > 2$	on	799 ± 62	

Therefore one requires a more detailed study of the fit performance in these modes.

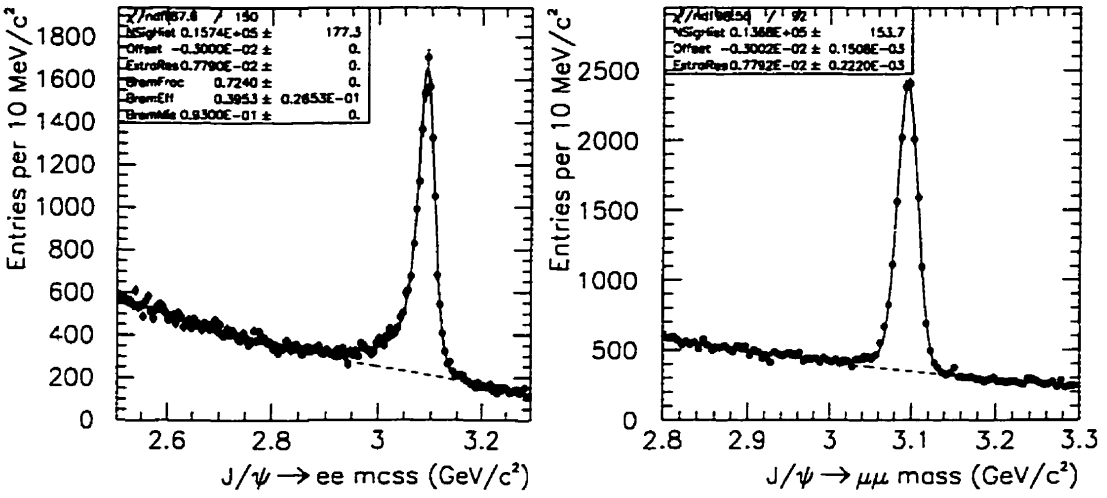

Figure 4.10: Fits to invariant mass distributions of candidates in (a) $J/\psi \to e^+e^-$ and (b) $J/\psi \to \mu^+\mu^-$.

Signal Yield in Monte Carlo

A Monte Carlo cocktail is constructed by combining the inclusive signal events, generic $B\overline{B}$ events, generic $c\bar{c}$ and *uds* events, all weighted to the on-resonance luminosity of the *BABAR* Run 1 data sample. Mass or mass difference histograms with a known number of signal events are created. To more closely mimic distributions observed in data, additional smearing (σ) and offset (δ) are added to Monte Carlo samples. Different values are used for $\psi \to \ell^+\ell^-$ events ($\sigma = 7$ MeV/c^2, $\delta = -3$ MeV/c^2) and for $\psi(2S) \to \pi^+\pi^- J/\psi$, $\chi_c \to \gamma J/\psi$ events ($\sigma = 2$ MeV/c^2, $\delta = -3$ MeV/c^2). The signal shapes agree very well in data and Monte (Figure 4.13) but the backgrounds to $\ell^+\ell^-$ distributions are underestimated. This background is due to the incorrectly identified leptons and the discrepancy has been traced to the way particle misidentification is handled in Monte Carlo. As the misidentification *levels* (a probability that a pion is identified as a muon, for instance) are not well simulated, we use the values extracted from clean data samples. These events do not cover the full kinematic range (momentum, polar

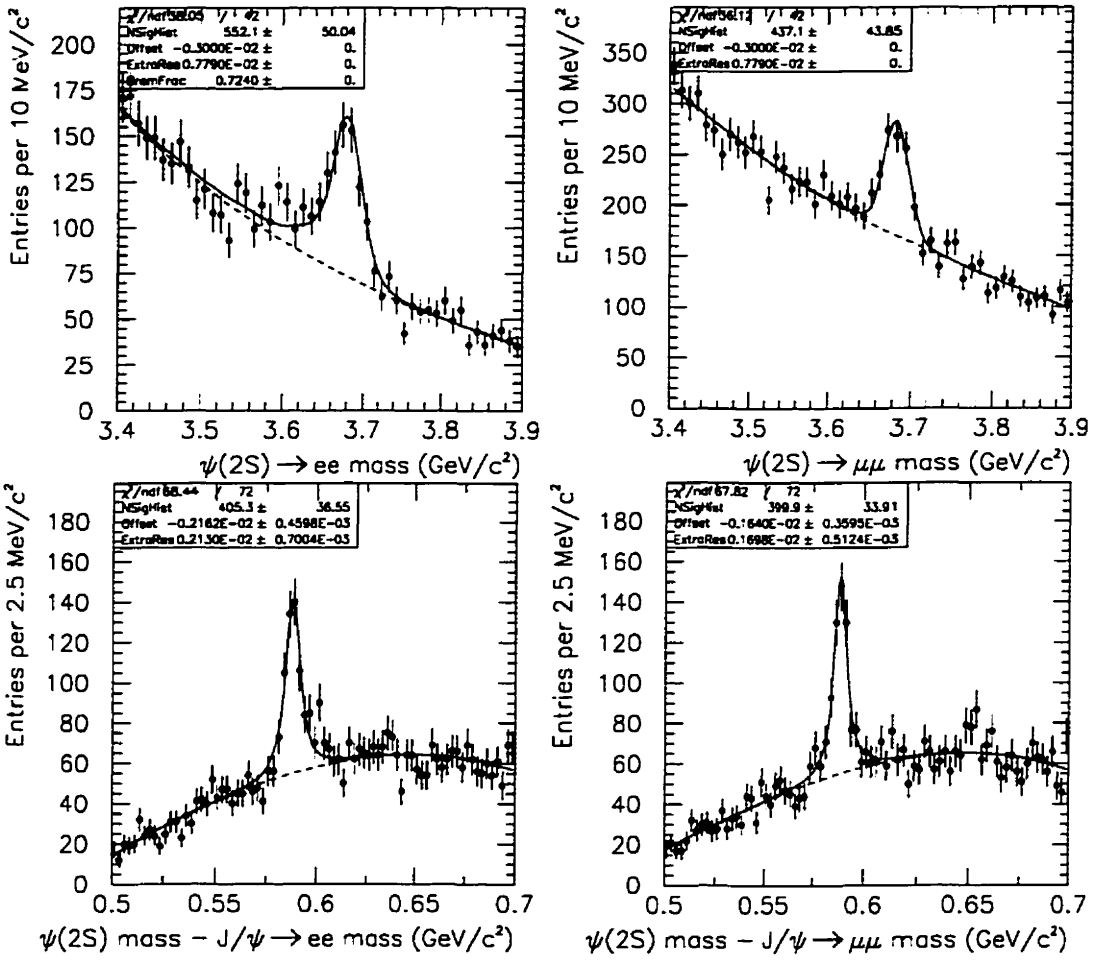

Figure 4.11: Fits to invariant mass distributions of (a) $\psi(2S) \rightarrow e^+e^-$ and (b) $\psi(2S) \rightarrow \mu^+\mu^-$, and to mass difference distributions of $\psi(2S) \rightarrow \pi^+\pi^- J/\psi$ candidates with (c) $J/\psi \rightarrow e^+e^-$ and (d) $J/\psi \rightarrow \mu^+\mu^-$.

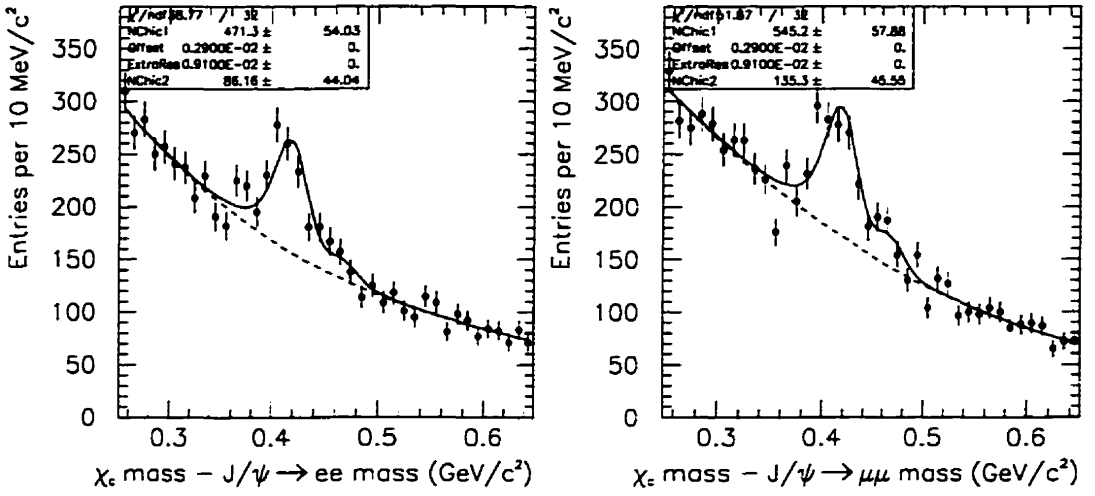

Figure 4.12: Fits to mass difference distributions of $\chi_c \rightarrow \gamma J/\psi$ candidates with (a) $J/\psi \rightarrow e^+e^-$ and (b) $J/\psi \rightarrow \mu^+\mu^-$.

and azimuthal angle) of the tracks used in our analysis. However, this does not pose a problem as we verified that fit yields are robust with respect to background scaling.

The fitting is performed in a manner identical to fitting the data. σ and δ are extracted from the $J/\psi \rightarrow \mu^+\mu^-$ fit, Bremsstrahlung parameters are extracted from the Monte Carlo sample created without the Bremsstrahlung recovery algorithm. Fit results are compared to the true values in Table 4.4. Note that a non-Bremsstrahlung recovery sample is slightly larger, hence the difference in the yields.

Both J/ψ fits return values that are 0.3% higher than the Monte Carlo number of events. This is well within the statistical errors of the fits (about 1%) so we do not correct the data yields based on this discrepancy. 0.3% error is added to the J/ψ fit systematic. Identical procedure is applied to other inclusive charmonium final states. Five of six deviations are consistent, within one standard deviation of the statistical error, with the true Monte Carlo number of events. The sixth deviation

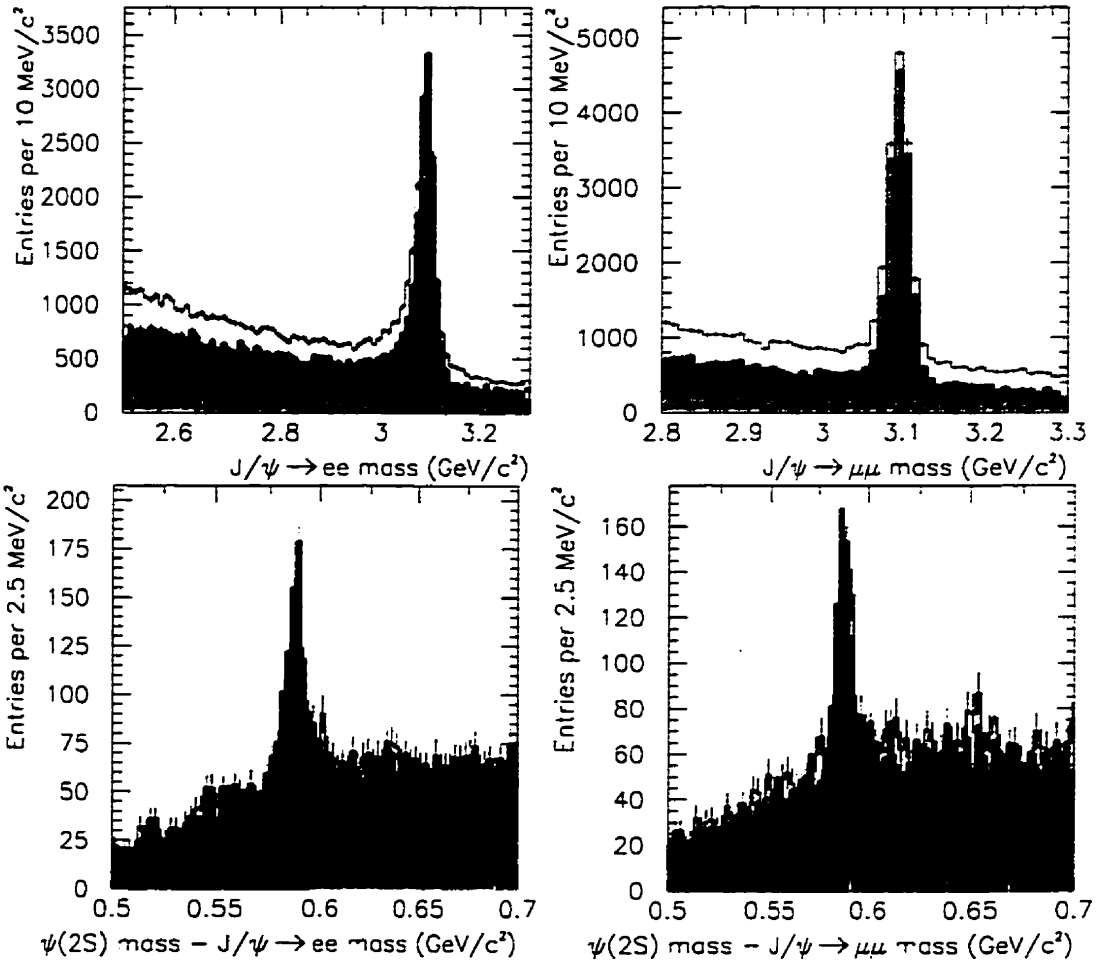

Figure 4.13: Observed mass or mass difference distributions superimposed with (cumulative bottom to top) generic uds, $c\bar{c}$, $B\overline{B}$ and inclusive signal Monte Carlo events. Plots are for: (a) $J/\psi \to e^+e^-$. (b) $J/\psi \to \mu^+\mu^-$. (c) $\psi(2S) \to \pi^+\pi^- e^+e^-$ and (d) $\psi(2S) \to \pi^+\pi^-\mu^+\mu^-$.

Table 4.4: Summary of fits to MC generated mass distributions. As for data, the $\mu^+\mu^-$ final state is used to measure the resolution parameters and the no-Brem-recovery e^+e^- sample is used to measure the fraction of events that undergo Bremsstrahlung.

Parameter	*MC Truth*	*Fit Result*
Offset	-3 MeV/c^2	-2.66 ± 0.14
Smearing	7 MeV/c^2	7.13 ± 0.21
N $J/\psi \rightarrow \mu^+\mu^-$	13,479	$13,515 \pm 141$
BremFrac B	0.573	0.568 ± 0.008
N $J/\psi \rightarrow e^+e^-$ no Brem-recovery	18,878	$18,636 \pm 178$
Brem Recovery Fraction B_R	0.464	0.483 ± 0.031
N $J/\psi \rightarrow e^+e^-$	15,304	$15,345 \pm 164$

is 1.5σ away. Again, we take the magnitude of the deviation as the systematic error but no correction is applied. The errors range from 2.8% to 8.2%. We do expect that additional Monte Carlo would reduce these errors significantly.

Functional Form of the Background

The fits are repeated with different background parameterization. Instead of the usual third order Chebychev polynomial, we use second and fourth order Chebychev, and the decaying exponential function. Fits with χ^2 probability less than 0.5% are not used. This excludes second order polynomial and the exponential backgrounds in the $J/\psi \rightarrow e^+e^-$ mode. The systematic error is calculated from the fit yields as one half of the maximal difference, divided by the yield of the nominal (third order Chebychev) yield. The value of 0.2% is obtained for both $J/\psi \rightarrow e^+e^-$ and $J/\psi \rightarrow \mu^+\mu^-$ modes.

Table 4.5: Total systematic errors (%) on the yields extracted from fits to mass or mass difference distributions.

Decay	e^+e^-	$\mu^+\mu^-$
$J/\psi \rightarrow \ell\ell$	0.8	1.0
$\psi(2S) \rightarrow \ell^+\ell^-$	3.6	8.2
$\psi(2S) \rightarrow \pi^+\pi^- J/\psi$	2.8	5.4
$\chi_c \rightarrow \gamma J/\psi$	3.3	3.5

Mass Window Range

Nominal histogram ranges used in $J/\psi \rightarrow \ell^+\ell^-$ fits are 2.8 to 3.3 GeV/c^2 for the muon mode and 2.5 to 3.3 GeV/c^2 for the electron mode. Both upper and lower bounds varied up to 100 MeV/c^2 in several steps and combinations. As above, the error is half the maximum yield deviation, divided by the nominal value. Values obtained, 0.7% for electrons and 0.9% for muons, are slight overestimates of the systematic error because they are not corrected for the fact that a small number of true J/ψ mesons exists in the mass range over which the boundaries are varied.

Total Systematic Errors

Combining the components described in previous sections yields total systematic errors listed in Table 4.5. These errors are used for branching fraction and cross section calculations.

Table 4.6: Deviation in $J/\psi \rightarrow e^+e^-$ yields from variation of the fit parameters. Corresponding systematic errors are displayed in the last column.

Fit Parameter	*Nominal Value*	*Range*	*Sys Err (%)*
Offset	-3.00 MeV/c^2	-3.23 – -2.83	< 0.1
Smearing	7.79 MeV/c^2	7.35 – 8.15	0.3
B^0	0.724	0.692 – 0.756	1.1
B_R	0.395	0.17 – 0.57	0.3
B_E	0.093	0.072 – 0.102	0.3
Total			1.2

4.4.6 Parameters of the $J/\psi \rightarrow e^+e^-$ Fit

Fit to the Bremsstrahlung recovered $J/\psi \rightarrow e^+e^-$ mass distribution is performed with smearing and offset fixed to the values returned by the $J/\psi \rightarrow \mu^+\mu^-$ fit, Bremsstrahlung fraction (B^0) extracted from the no-Bremsstrahlung fit and Bremsstrahlung fake rate B_E set to the Monte Carlo value. A contribution to the error on the extracted yields due to the uncertainty of these parameters must be calculated. Nominal values of the parameters are varied within a reasonable range and the errors are calculated by dividing a half of the maximal yield deviation by the nominal yield. Results are tabulated in Table 4.6. The Bremsstrahlung efficiency parameter, B_R, is varied by ± 0.2, much more than its fit uncertainty. The Bremsstrahlung fake parameter is varied by roughly 10% and only a weak effect on the yield is observed. All other parameters are varied within one standard deviation, as returned by the appropriate fits.

All variations are added in quadrature and the resulting 1.2% error is added (in quadrature) to the statistical error on $J/\psi \rightarrow e^+e^-$ yields. Main contribution is

from the uncertainty of the true Bremsstrahlung fraction.

4.4.7 Mass Resolution

Resolution of the measured J/ψ mass is a good diagnostic of the drift chamber (DCH) performance. *BABAR* data is divided into two blocks, corresponding to the low DCH voltage (1900 V) running period, block 1, and the high DCH voltage (1960 V) period, block 2. Each block is divided into several periods based on other conditions, such as the gas mixture in the IFR or the software release used for event reconstruction. We extract the mass resolution by adding (in quadrature) the resolution observed in Monte Carlo to the smearing obtained from the fits to data. Monte Carlo resolution is the same for e^+e^- and $\mu^+\mu^-$ final states: 9.45 ± 0.20 MeV/c^2. Inclusive $J/\psi \to \mu^+\mu^-$ data are divided into 13 run periods and mass peaks are fit, allowing the smearing and offset parameters to float. Better average resolution is obtained for the high DCH voltage period, 11.4 ± 0.3 MeV/c^2 versus 13.0 ± 0.3 MeV/c^2 for the low DCH voltage. The results are consistent for e^+e^- and $\mu^+\mu^-$ modes.

4.4.8 Variation of Yields With the Run Period

We check for possible systematic effects introduced by different conditions in the run periods by extracting normalized J/ψ yields per produced B meson, $\left(N_{J/\psi}/N_B\right) / \left(\sum N_{J/\psi} / \sum N_B\right)$, in each data subset. Results presented in Figure 4.14 are scaled by efficiency but are not corrected for differences between data and Monte Carlo (mass acceptance, tracking effects or particle identification).

A more complete analysis is done for the two run blocks. A set of tracking and particle identification corrections (fully discussed in Section 4.5) is calculated

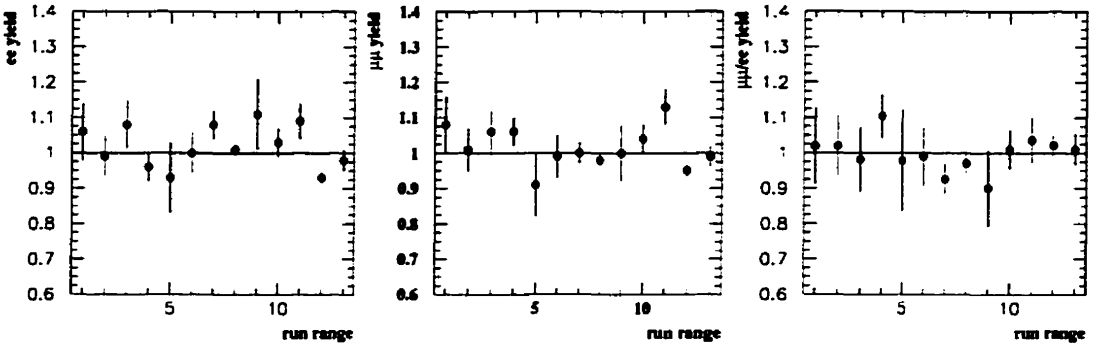

Figure 4.14: Normalized number of J/ψ mesons per B meson as a function of data subset for $J/\psi \to e^+e^-$ and $J/\psi \to \mu^+\mu^-$. The ratio of $\mu^+\mu^-$ to e^+e^- yields is shown in the last plot. Set 9 is the first with the drift chamber at 1960V.

for each block. A complete J/ψ branching fraction calculation (as described in Section 4.7) is performed. Four independent measurements of the inclusive $B \to J/\psi X$ branching fraction are presented in Table 4.7.

The consistency of the four measurements (combining the results gives an average of $1.037 \pm 0.017)\%$, with a χ^2/n.d.o.f. $= 1.78/3$) increases our confidence in all aspects of the analysis, particularly the handling of lepton identification efficiencies.

4.5 Lepton Identification

Lepton identification is a crucial element of this analysis. Precise knowledge of the efficiencies is necessary to verify the consistency of the branching fraction measurements obtained from electron and from muon modes. Systematic errors due to lepton identification contribute to the total systematic error of all studies presented in this thesis, and many other studies pursued in the collaboration. Thus, they need to be well understood. We consider only standard selection criteria of the cut based lepton selectors used in *BABAR*. We also investigate the

Table 4.7: Summary of $\mathcal{B}(B \to J/\psi)$ measured with each data block and lepton type. The branching fraction uncertainty includes only the statistical error on the yield and PID uncertainties.

Data Set	$N_{J/\psi}$	*Tracking Corr.*	*PID Eff*	$\mathcal{B}$*(%)*
Block 1, e^+e^-	$8,474 \pm 196$	0.965	0.941 ± 0.026	1.024 ± 0.036
Block 1, $\mu^+\mu^-$	$7,091 \pm 159$	0.965	0.738 ± 0.014	1.018 ± 0.030
Block 2, e^+e^-	$7,115 \pm 171$	0.986	0.908 ± 0.025	1.029 ± 0.038
Block 2, $\mu^+\mu^-$	$6,080 \pm 133$	0.986	0.694 ± 0.013	1.071 ± 0.031

increase in efficiency when using NoCal selector in a combination with a different one. For instance Loose *or* NoCal selects tracks passing loose electron criteria and the tracks with no calorimeter information which pass NoCal cuts.

We measure lepton identification systematic errors by comparing lepton efficiencies extracted from the inclusive J/ψ yields to the efficiencies calculated using the official electron and muon identification tables. Furthermore, we present the lepton identification efficiencies for the J/ψ mesons selected using several combinations of lepton identification criteria. Combined with the corresponding efficiencies calculated using the standard particle identification tables, these can be used to correct for the systematic shift between the tables and the inclusive J/ψ measurements.

4.5.1 Standard Lepton Identification Criteria

Lepton identification at *BABAR* is standardized to minimize duplicated efforts and allow for simple consistency checks across different analyses being conducted by different teams of *BABAR* physicists. Performance of particle selectors, such as efficiencies and misidentification levels, is studied, monitored and documented [AWG00b,

AWG00a] by the muon and electron identification analysis working groups. Several selector criteria are defined for each lepton type, providing a range of efficiencies and purities satisfactory for most physics needs.

Muon Identification

The IFR is the primary detector for muon identification. To define the variables used, we need information beyond that given in Chapter 3. Electrical signals are collected on strip-shaped electrodes along perpendicular directions to obtain a two dimensional readout for each layer. All charged tracks reconstructed in the DCH are projected into the IFR and hit strips associated with a track are grouped into a cluster. Muon identification relies on the following variables:

- the energy released in the EMC,
- the number of IFR layers hit in a cluster,
- the first IFR layer hit in a cluster,
- the last IFR layer hit in a cluster,
- the number of interaction lengths traversed by the track in the *BABAR* detector (an average of 4 interaction lengths is traversed by muons at normal incidence in the barrel region of the detector),
- the number of interaction lengths the track is expected to traverse assuming it is a muon,
- the χ^2 per degree of freedom of the IFR hit strips with respect to the track extrapolation,
- the total number of IFR strips hit in the i-th layer,

- the total number of strips hit in the cluster.

Five standard selection criteria - Minimum Ionizing Particle, VeryLoose, Loose, Tight, VeryTight - are defined by requiring that track parameters lie in a given region of the space defined by quantities listed above. The nomenclature is self-evident.

Electron Identification

The main quantity distinguishing electrons is the ratio of energy deposited in the calorimeter to the momentum of the track. Thus, EMC and DCH are crucial for electron selection. Very pure electron sample is achieved by adding information from the DIRC. Neighbouring EMC crystals passing some preset energy threshold are combined into a cluster. As the energy associated with a cluster could have originated from more than a single particle, a cluster with more than one local energy maximum is split into several bumps. Total energy of the cluster is shared between the bumps. The variables used in electron identification are:

- specific ionization of the track (dE/dx) in the DCH and the SVT,
- ratio of energy deposited in the calorimeter to the momentum of the track (E/p),
- number of crystals in the cluster,
- Lateral energy distribution, first introduced by Argus [D$^+$85],
- Zernike moments, first introduced by ZEUS [SV97],
- difference in the azimuthal angle of the shower centroid and the track extrapolated to the EMC,

- DIRC consistency with the electron hypothesis.

Standard selection criteria are VeryLoose, Loose, Tight and VeryTight. An additional selector, NoCal, is designed to select electrons outside of the calorimeter acceptance based on the dE/dx information only.

4.5.2 Methods for calculating lepton efficiencies

Efficiencies of the cut based selectors, for each of the standard modes, are calculated in two ways: using the standard particle identification tables and using the inclusive J/ψ yields. The differences between corresponding values are used to evaluate systematic errors.

Particle identification tables

Standard particle identification tables contain efficiencies of a particular selector accepting a particle of a given type, thus also containing information about purity levels. These efficiencies are extracted from high purity control *data* samples, such as the channels $e^+e^- \to \mu^+\mu^-\gamma$, $e^+e^- \to e^+e^-\mu^+\mu^-$, $\gamma\gamma \to e^+e^-e^+e^-$, photon conversions, Bhabha and radiative Bhabha events. Tables are organized according to momentum, polar angle and the azimuthal angle of the track. Each variable is divided in a fixed number of bins.

Angular distributions and the momentum spectra of the lepton daughters of the J/ψ need to be convoluted with the tables to obtain a single efficiency per lepton per selection criterion. This is done by running a script that reads the efficiency tables and the PDF containing lepton p and θ distributions and then calculates average efficiency for each mode. Flat distribution of the azimuthal angle is assumed in order to reduce granularity and thus increase statistics per bin. Distributions

of momentum and the polar angle of the lepton candidates passing the analysis selection are obtained from the Monte Carlo sample, separately for electrons and for muons. Selected tracks are required to match a true Monte Carlo track. Figure 4.15 shows the distributions for electrons and muons separately.

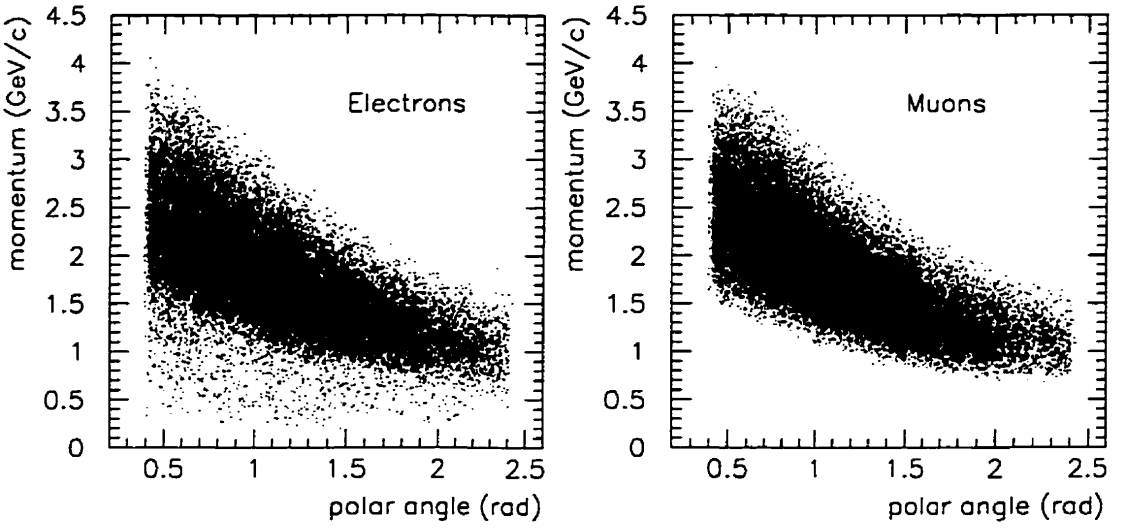

Figure 4.15: Distributions of lepton momenta plotted versus the polar angle of the track for Monte Carlo $J/\psi \to \ell^+\ell^-$ events passing selection.

Data

Inclusive yields of $J/\psi \to \ell^+\ell^-$ are calculated by fitting the invariant mass spectra of the candidates passing the analysis selection. Signal PDFs are extracted from the Monte Carlo sample, as discussed in Section 4.4.

Two methods, very similar in nature, are used to calculate lepton selector efficiencies. Comparison of the results serves as a cross-check. In both cases we distinguish the control mode from the test mode. The lepton of the specified charge must pass the test mode, which is any of the five standard selection crite-

ria. To ensure purity of the J/ψ sample the lepton of the opposite charge must pass the VeryTight control mode.

Pass-fail method involves expressing a given efficiency in terms of numbers of J/ψ candidates with lepton daughters passing or failing the appropriate selection criterion.

$$\epsilon(\text{test}, \text{control}) = \frac{N(\text{test}, \text{control})}{N(\text{test}, \text{control}) + N(\overline{\text{test}}, \text{control})} \tag{4.10}$$

N represents a number of events returned by the fit for a given combination of modes. The horizontal bar ($\overline{\text{test}}$) denotes that the lepton failed the test selection. By definition, control leptons are required to pass the VeryTight selection.

Efficiency calculated by the normalization method is the ratio of number of events passing the test mode to the number of events with no selection performed on the test lepton. Again, the other lepton must pass the control mode.

$$\epsilon(\text{test}, \text{control}) = \frac{N(\text{test}, \text{control})}{N(\text{none}, \text{control})} \tag{4.11}$$

The Jpsitoll skim requires that all muons must pass the minimum ionizing particle (MIP) selection criterion. Hence muon efficiencies are calculated by normalizing to $N(\text{MIP}, \text{control})$ rather than $N(\text{none}, \text{control})$ and then corrected for this effect. The correction factor is the MIP efficiency calculated from the tables, $\epsilon_{MIP} = 0.995$. No systematic error has been assigned to this correction.

Differences between two methods are rather subtle. If the yields were known exactly, the results of applying these two methods would be the same because the terms in the denominators are actually identical: $N(\text{none}, \text{control}) = N(\text{test}, \text{control}) + N(\overline{\text{test}}, \text{control})$. Pass-fail method requires fitting $N(\overline{\text{test}}, \text{control})$ which can have very poor signal to noise ratio. However, obtaining the full term as a sum of two independent measurements (pass-fail method) yields smaller statistical error on the calculated efficiency. All terms in Equation 4.10 are statistically independent

and the propagation of errors is trivial. Numerator and denominator in Equation 4.11 are dependent and simple error propagation overestimates the error on the efficiencies.

The agreement between the two methods increases our confidence in the fitting procedure but only results of the pass-fail method, which have correctly calculated relative error, are used in calculations of the final systematic errors.

Note that throughout the analysis charges are treated independently. That is we calculate efficiencies for selecting positive leptons separately from efficiencies for selecting negative leptons.

4.5.3 Method validation

We validate the pass-fail method described in the previous section by applying it to a cocktail Monte Carlo sample and extracting known efficiencies. The cocktail is a mixture of inclusive J/ψ events, generic $B\overline{B}$ events and continuum events, both $c\bar{c}$ and uds, scaled to the size of the full Run1 dataset. All signal events, containing $J/\psi \rightarrow \ell^+\ell^-$, have been removed from the generic sample.

The correlation between the momenta and the angles of the two lepton daughters of the J/ψ could introduce a systematic error to the measurement of the lepton efficiencies (Figure 4.16). For instance, VeryTight muon efficiency is higher in a good sector of the IFR, so high angular correlation would increase a chance of the test muon passing through the same detector region, resulting in a higher than average efficiency of the test mode being calculated. The same is true for the momentum dependence. This error is estimated by the difference in efficiencies calculated from the tables, as previously described, and the efficiencies calculated by applying pass-fail method to signal Monte Carlo sample (with PID killing using

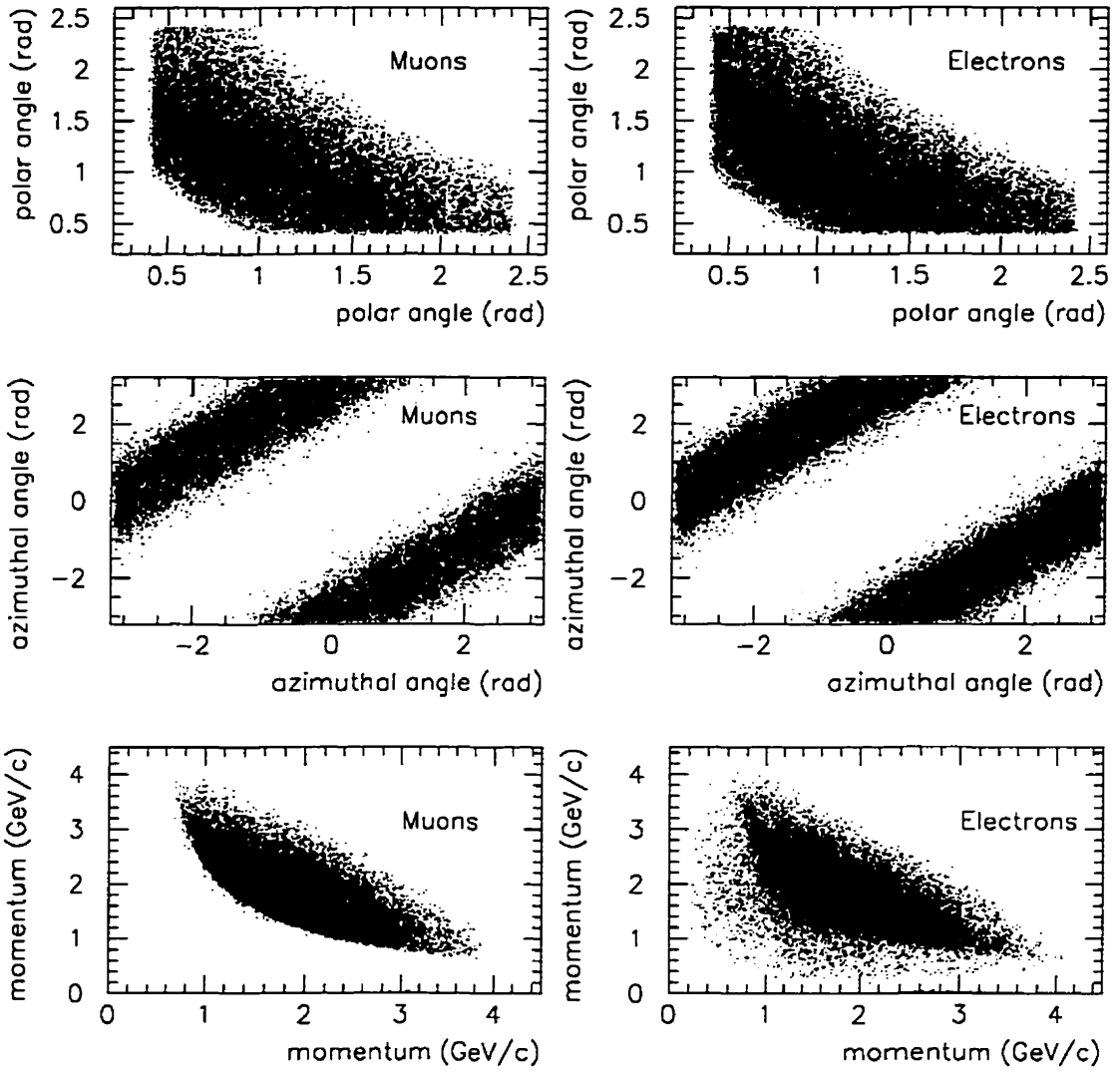

Figure 4.16: Correlation between polar angle (top), azimuthal angle (middle) and momenta (bottom) of the lepton daughters of the J/ψ. Muons are shown on the left and electrons on the right.

the same tables) by counting the truth matched candidates instead of fitting. The second method of calculating the efficiencies from the PID tables reflects the correlation of J/ψ daughters. This systematic error is 0.25% for muons and 0.26% for the electrons, and it is added in quadrature to the final lepton identification systematic error. This is a systematic effect as the efficiencies including the lepton

correlation are always smaller than those calculated directly from the tables, as described in section 4.5.2.

Applying the full pass-fail method (with fitting) to the Monte Carlo cocktail, we look at the difference between the number of signal events returned by the fit and the true number of signal events matched to Monte Carlo truth. Fits to the distribution of test leptons passing the selection have very clean signal and the fit errors are on the 1% level. Fitting the distributions with a test lepton failing the selection is more difficult because signal to background ratio is much smaller. Here some of the errors are as large as 50%. This is not a big problem because the numbers of failed test leptons do not contribute as strongly to the efficiency calculated by the pass-fail method. Muon fits predominantly overestimate the yields while electron fits predominantly underestimate the yields. We correct for this effect by calculating the additive correction factors that are added to the signal events observed in data. The correction factors are shown in Table 4.8 in the results section. A systematic error equal to the absolute value of the correction is added in quadrature to the statistical error of the data yields.

In a manner identical to the inclusive Charmonium study, we evaluate the effects of not applying the Bremsstrahlung recovery algorithm to the electron daughters of the J/ψ. We repeat the Monte Carlo cocktail analysis on a sample created with the recovery algorithm turned off. Although fits to non-Bremsstrahlung reconstructed mass spectra behave well when there is a clean signal, they show poor results when applied to the high background cases. High backgrounds occur when the test lepton fails the selection. We calculate a cumulative relative error as $(100 \sum \frac{|N_{fit}-N_{true}|}{N_{true}})$ for the 17 fits used in the analysis. Based on the error values of 34% for the non-Bremsstrahlung recovered data and 17% for Bremsstrahlung recovered data, we choose to use the latter. These errors are dominated by the errors in fitting the spectra of failed test modes, where the average errors are

44% and 23% respectively. Given these results we are confident that applying the Bremsstrahlung recovery algorithm is beneficial to the analysis. Furthermore, the effects of the Bremsstrahlung recovery are well understood and the fits to this data set yield reliable results.

4.5.4 Methods for calculating systematic errors

The results presented in Tables 4.8-4.10 include a multiplicative factor to correct the results obtained with particle identification tables to those obtained by the J/ψ sample. This factor corrects for the impact of the rest of the hadronic event, for example. The systematic error on this quantity has three components: the statistical error on the fits, the uncertainty on the additive correction and the difference between the two methods of using the PID tables. These are added in quadrature to get the total systematic error (in %) labeled 'sys err corr' in the tables.

If the correction factors are not used, an additional systematic error, equal to the 1−correction, is added in quadrature to get the value 'sys err uncorr.' For example, *not* applying a 90 % multiplicative correction results in an additional 10 % systematic error.

The lepton identification efficiencies for the J/ψ mesons are calculated as $\epsilon_{J/\psi} = \epsilon_T^+\epsilon_L^- + \epsilon_L^+\epsilon_T^- - \epsilon_T^+\epsilon_T^-$, where T and L respectively denote tighter and looser of the two lepton PID criteria, and + & − denote lepton charges.

4.5.5 Results

In Table 4.8 we present: inclusive J/ψ yields (N fit *and* N corrected), additive corrections to the yields (Corr) found from the Monte Carlo studies, lepton and

J/ψ efficiencies observed in data using pass-fail method (eff Data) and efficiencies from particle identification tables derived from full Run1 data sample (eff Table), ratios of efficiencies needed to correct the Monte Carlo particle identification efficiencies (eff D / eff T), systematic errors if the efficiency correction is applied (sys err corr) and if the correction is not applied (sys err uncorr). This is done for all electron and muon selection modes and several J/ψ selection modes. In these tables, a column of measured values is followed by a column containing the statistical uncertainties.

As mentioned, we also examine efficiencies for an analysis using NoCal criteria in conjunction with another mode. The control mode is still VeryTight but the test mode has been augmented with a NoCal selector, as discussed earlier. The effect of the NoCal selector is small. The average effect is a 0.35% increase in lepton efficiency and 0.4% increase in J/ψ efficiency. The largest observed improvement to J/ψ efficiency is 0.6%, achieved if both leptons have a NoCal selector added. Moreover, J/ψ selection with a particle identification applied only to a single leg of the J/ψ (either Tight or Loose) is virtually 100% efficient even without the NoCal selector added. This suggests that the same correction factors and systematic errors be used in the analyses which include electron candidates without the calorimeter information.

Tables 4.9 and 4.10 display identical information for the two blocks of Run 1. Block 1 corresponds to the period when data were collected with the drift chamber voltage of 1900V, and block 2 to the period when data were collected with the drift chamber voltage of 1960V. Additive corrections were scaled according to the B counting to obtain the appropriate values for each data block. To compare the results we calculate the average relative deviation from full run $(\frac{100}{N}\sum\frac{\epsilon_{l,block\ i}-\epsilon_{l,run\ 1}}{\epsilon_{l,run\ 1}})$ and the average statistical uncertainty $(\frac{100}{N}\sum\frac{\sigma_{l,block\ i}}{\epsilon_{l,block\ i}})$, separately for electron and muon channels in each block. The sums are over ten muon efficiencies or over

eight electron efficiencies shown in the tables. Muon efficiencies in block 1 are $1.3 \pm 1.5\%$ *higher* than in the full run, and in block 2 they are $1.5 \pm 1.6\%$ *lower* than in the full run. Because of the large errors, it is hard to know whether we are observing the expected efficiency decrease or a statistical fluctuation. Electron efficiencies in each block are higher than in the whole run, $1.5 \pm 2.0\%$ in block 1 and $0.3 \pm 2.5\%$ in block 2! This comes about as follows. Smaller statistics have a bigger effect on the fits with the electron failing the test mode. An underestimate in these yields results in efficiencies of both blocks being higher (with the deviation well within the statistical error) than the efficiency of the whole run. Significantly better agreement between data and PID tables is observed in block 1 than in block 2.

4.5.6 Summary

Results of the lepton identification analysis are shown in Tables 4.8-4.10. The efficiencies measured in data are labeled 'eff D'. These values will be used in all inclusive measurements. The correction factors ('eff D / eff T') are ratios of efficiencies measured in data to the efficiencies calculated from the Run1 (as specified earlier) particle identification tables. The first column of systematic errors (sys err corr) is appropriate for an analysis that either corrects the Monte Carlo efficiencies according to the correction factors, or explicitly uses the 'eff D' values. The second column of systematic errors (sys err uncorr) is for an analysis using uncorrected Monte Carlo efficiencies. Similar quantities are calculated for J/ψ mesons.

Finally, it should be emphasized that these results are used in all *BABAR* analyses involving Charmonium. Furthermore, they are suitable for all analyses of channels involving leptons with the momentum spectrum similar to the spectrum of lepton

Muons, Run1

		Pass				Fail				Results				
Mode	Q	N fit	Corr	N corrected		N fit	Corr	N corrected		eff Table	eff Data	sys err corr	eff D / eff T	sys err uncorr
Vtight	+	9151	118	36	9187 123	4641	154	-91	4550 179	0.685	0.665	1.4	0.971	3.2
Tight	+	9607	121	28	9635 124	4182	151	-91	4091 176	0.717	0.698	1.4	0.974	3.0
Loose	+	11882	136	0	11882 136	1914	136	-62	1852 149	0.865	0.860	1.1	0.994	1.3
Vloose	+	12654	148	122	12776 192	1161	125	-166	995 207	0.913	0.922	1.5	1.010	1.8
Mip	+	13724	183	15	13739 184	79	69	-57	22 89	0.994	0.993	0.7	0.998	0.7
Vtight	-	9151	118	36	9187 123	4435	156	-91	4344 180	0.683	0.675	1.5	0.989	1.8
Tight	-	9595	121	28	9623 124	3989	154	-91	3898 179	0.716	0.708	1.4	0.989	1.8
Loose	-	11748	137	0	11748 137	1859	139	-62	1797 152	0.864	0.863	1.2	0.999	1.2
Vloose	-	12431	148	122	12553 192	1163	129	-166	997 210	0.912	0.922	1.6	1.010	1.9
Mip	-	13621	187	15	13636 188	0	36	-57	-57 67	0.995	0.999	0.6	1.004	0.7

Electrons, Run1

		Pass				Fail				Results				
Mode	Q	N fit	Corr	N corrected		N fit	Corr	N corrected		eff Table	eff Data	sys err corr	eff D / eff T	sys err uncorr
Vtight	+	14602	162	131	14733 208	1737	205	232	1969 310	0.911	0.882	1.9	0.968	4.1
Tight	+	15740	171	148	15888 226	634	200	94	728 221	0.976	0.956	1.4	0.980	2.5
Loose	+	16079	178	149	16228 232	273	198	118	391 231	0.986	0.976	1.4	0.990	1.8
Vloose	+	16089	187	180	16269 260	229	189	94	323 211	0.990	0.981	1.3	0.991	1.6
Vtight	-	14602	162	131	14733 208	1734	207	232	1966 311	0.902	0.882	1.9	0.978	3.5
Tight	-	15649	170	148	15797 225	695	202	94	789 223	0.972	0.952	1.4	0.980	2.7
Loose	-	15910	176	149	16059 231	438	199	118	556 231	0.985	0.967	1.4	0.981	2.4
Vloose	-	15939	184	180	16119 258	373	192	94	467 214	0.988	0.972	1.3	0.983	2.2

J/Ψ->ee, Run1

Mode		eff Table		eff Data		eff D / eff T	sys err corr	sys err uncorr
Vtight	Vtight	0.8224	0.0007	0.778	0.021	0.946	2.7	6.0
Tight	Tight	0.9490	0.0004	0.911	0.018	0.960	1.9	4.5
Loose	Loose	0.9717	0.0003	0.944	0.019	0.971	2.0	3.5
Vloose	Vloose	0.9782	0.0003	0.953	0.018	0.974	1.9	3.2
Vtight	Tight	0.9445	0.0004	0.905	0.016	0.959	1.8	4.5
Tight	Loose	0.9715	0.0003	0.943	0.019	0.971	2.0	3.5
Tight	Vloose	0.9780	0.0003	0.952	0.017	0.974	1.8	3.2
Tight	None	0.9993	0.0000	0.998	0.001	0.999	0.1	0.2
Loose	None	0.9998	0.0000	0.999	0.001	0.999	0.1	0.1

J/Ψ->μμ, Run1

Mode		eff Table		eff Data		eff D / eff T	sys err corr	sys err uncorr
Vtight	Vtight	0.4679	0.0006	0.449	0.009	0.960	2.0	4.5
Tight	Tight	0.5128	0.0006	0.494	0.010	0.964	2.0	4.1
Loose	Loose	0.7471	0.0005	0.742	0.012	0.993	1.6	1.8
Vloose	Vloose	0.8331	0.0005	0.850	0.019	1.020	2.2	3.0
Mip	Mip	0.9891	0.0001	0.992	0.009	1.003	0.9	0.9
Tight	Loose	0.7251	0.0005	0.717	0.010	0.989	1.4	1.8
Loose	Vloose	0.8307	0.0004	0.846	0.018	1.019	2.1	2.8
Loose	Mip	0.9721	0.0001	0.974	0.008	1.002	0.8	0.8
Loose	None	0.9816	0.0001	0.981	0.004	0.999	0.4	0.4

Table 4.8: Full Run 1. Inclusive J/ψ yields (N fit *and* N corrected), additive corrections to the yields (Corr), lepton and J/ψ efficiencies observed in data (eff Data) and from particle identification tables (eff Table), correction factor (eff D / eff T), systematic errors if the efficiency correction is applied (sys err corr) and if the correction is not applied (sys err uncorr).

Muons, Block1

		Pass					Fail					Results				
Mode	Q	N fit		Corr	N corrected		N fit		Corr	N corrected		eff Table	eff Data	sys err corr	eff D / eff T	sys err uncorr
Vtight	+	4917	87	19	4936	89	2320	113	-48	2272	123	0.685	0.681	1.8	0.994	1.9
Tight	+	5181	90	15	5196	91	2056	111	-48	2008	121	0.717	0.717	1.8	1.001	1.8
Loose	+	6301	101	0	6301	101	951	100	-33	918	105	0.865	0.868	1.5	1.003	1.5
Vloose	+	6730	109	65	6795	127	528	93	-88	440	128	0.913	0.934	1.8	1.022	2.9
Mip	+	7148	134	8	7156	134	56	53	-30	26	61	0.994	0.991	0.9	0.996	1.0
Vtight	-	4917	87	19	4936	89	2286	115	-48	2238	125	0.683	0.684	1.9	1.002	1.9
Tight	-	5194	90	15	5209	91	2010	113	-48	1962	123	0.716	0.723	1.8	1.010	2.1
Loose	-	6324	102	0	6324	102	883	103	-33	850	108	0.864	0.877	1.6	1.015	2.2
Vloose	-	6638	109	65	6703	127	553	95	-88	465	130	0.912	0.930	1.8	1.020	2.7
Mip	-	7226	138	8	7234	138	0	15	-30	-30	34	0.995	0.999	0.5	1.004	0.7

Electrons, Block1

		Pass					Fail					Results				
Mode	Q	N fit		Corr	N corrected		N fit		Corr	N corrected		eff Table	eff Data	sys err corr	eff D / eff T	sys err uncorr
Vtight	+	7663	125	70	7733	143	640	163	124	764	205	0.911	0.910	2.4	0.999	2.5
Tight	+	8235	132	69	8314	154	85	176	50	135	183	0.976	0.984	2.2	1.008	2.3
Loose	+	8281	137	79	8360	158	0	98	63	63	116	0.986	0.993	1.4	1.006	1.5
Vloose	+	8275	145	96	8371	174	0	97	50	50	109	0.990	0.994	1.3	1.004	1.4
Vtight	-	7663	125	70	7733	143	811	164	124	935	205	0.902	0.892	2.4	0.989	3.0
Tight	-	8185	131	79	8264	153	285	164	50	335	172	0.972	0.961	2.0	0.988	2.5
Loose	-	8295	136	79	8374	157	177	163	63	240	175	0.985	0.972	2.0	0.987	2.5
Vloose	-	8261	143	96	8357	172	158	159	50	208	167	0.988	0.976	2.0	0.987	2.4

J/Ψ->ee, Block1

Mode		eff Table		eff Data		eff D / eff T	sys err corr	sys err uncorr
Vtight	Vtight	0.8224	0.0007	0.812	0.028	0.987	3.4	3.6
Tight	Tight	0.9490	0.0004	0.946	0.028	0.996	3.0	3.0
Loose	Loose	0.9717	0.0003	0.965	0.024	0.993	2.5	2.6
Vloose	Vloose	0.9782	0.0003	0.970	0.023	0.992	2.4	2.5
Vtight	Tight	0.9445	0.0004	0.941	0.026	0.996	2.8	2.8
Tight	Loose	0.9715	0.0003	0.965	0.024	0.993	2.5	2.6
Tight	Vloose	0.9780	0.0003	0.970	0.023	0.992	2.3	2.5
Tight	None	0.9993	0.0000	0.999	0.001	1.000	0.1	0.1
Loose	None	0.9998	0.0000	1.000	0.000	1.000	0.0	0.0

J/Ψ->μμ, Block1

Mode		eff Table		eff Data		eff D / eff T	sys err corr	sys err uncorr
Vtight	Vtight	0.4679	0.0006	0.466	0.012	0.996	2.6	2.7
Tight	Tight	0.5128	0.0006	0.518	0.013	1.011	2.6	2.8
Loose	Loose	0.7471	0.0005	0.761	0.016	1.019	2.2	2.9
Vloose	Vloose	0.8331	0.0005	0.869	0.022	1.043	2.6	5.0
Mip	Mip	0.9891	0.0001	0.990	0.010	1.001	1.0	1.0
Tight	Loose	0.7251	0.0005	0.738	0.014	1.018	1.9	2.6
Loose	Vloose	0.8307	0.0004	0.865	0.021	1.042	2.4	4.8
Loose	Mip	0.9721	0.0001	0.975	0.009	1.003	1.0	1.0
Loose	None	0.9816	0.0001	0.984	0.005	1.002	0.5	0.6

Table 4.9: Block 1 only. Inclusive J/ψ yields (N fit *and* N corrected), additive corrections to the yields (Corr), lepton and J/ψ efficiencies observed in data (eff Data) and from particle identification tables (eff Table), correction factor (eff D / eff T), systematic errors if the efficiency correction is applied (sys err corr) and if the correction is not applied (sys err uncorr).

Muons, Block2

		Pass					Fail					Results				
Mode	Q	N fit		Corr	N corrected		N fit		Corr	N corrected		eff Table	eff Data	sys err corr	eff D / eff T	sys err uncorr
Vtight	+	4216	79	17	4233	81	2310	104	-42	2268	112	0.685	0.647	1.9	0.945	5.8
Tight	+	4407	81	13	4420	82	2117	103	-43	2074	111	0.717	0.677	1.9	0.944	5.9
Loose	+	5556	93	0	5556	93	957	92	-29	928	96	0.865	0.852	1.5	0.985	2.2
Vloose	+	5897	100	57	5954	115	636	84	-77	559	114	0.913	0.909	1.8	0.995	1.9
Mip	+	6543	124	7	6550	124	25	47	-27	-2	54	0.994	0.995	0.9	1.000	0.9
Vtight	-	4216	79	17	4233	81	2138	105	-42	2096	113	0.683	0.665	1.9	0.974	3.3
Tight	-	4382	81	13	4395	82	1969	104	-43	1926	112	0.716	0.692	1.9	0.967	3.9
Loose	-	5401	92	0	5401	92	971	94	-29	942	98	0.864	0.847	1.6	0.981	2.5
Vloose	-	5769	99	57	5826	114	608	86	-77	531	116	0.912	0.912	1.9	1.000	1.9
Mip	-	6364	126	7	6371	126	24	43	-27	-3	51	0.995	0.995	0.8	1.000	0.8

Electrons, Block2

		Pass					Fail					Results				
Mode	Q	N fit		Corr	N corrected		N fit		Corr	N corrected		eff Table	eff Data	sys err corr	eff D / eff T	sys err uncorr
Vtight	+	6483	115	61	6544	130	708	152	109	817	187	0.911	0.889	2.6	0.976	3.9
Tight	+	6974	121	69	7043	139	221	153	44	265	159	0.976	0.964	2.2	0.987	2.6
Loose	+	7188	126	70	7258	144	20	204	55	75	211	0.986	0.990	2.9	1.003	2.9
Vloose	+	7195	133	84	7279	158	20	243	44	64	247	0.990	0.991	3.4	1.002	3.4
Vtight	-	6483	115	61	6544	130	802	152	109	911	187	0.902	0.878	2.5	0.973	4.3
Tight	-	6929	120	69	6998	138	346	151	44	390	157	0.972	0.947	2.2	0.974	3.6
Loose	-	7029	124	70	7099	142	241	150	55	296	160	0.985	0.960	2.2	0.975	3.4
Vloose	-	7125	131	84	7209	156	170	147	44	214	153	0.988	0.971	2.1	0.983	2.8

J/Ψ->ee, Block2

Mode		eff Table		eff Data		eff D / eff T	sys err corr	sys err uncorr
Vtight	Vtight	0.8224	0.0007	0.780	0.028	0.949	3.6	6.2
Tight	Tight	0.9490	0.0004	0.913	0.028	0.962	3.1	4.9
Loose	Loose	0.9717	0.0003	0.950	0.034	0.978	3.6	4.2
Vloose	Vloose	0.9782	0.0003	0.963	0.038	0.984	4.0	4.3
Vtight	Tight	0.9445	0.0004	0.908	0.026	0.961	2.9	4.8
Tight	Loose	0.9715	0.0003	0.950	0.034	0.978	3.6	4.2
Tight	Vloose	0.9780	0.0003	0.962	0.037	0.984	3.9	4.2
Tight	None	0.9993	0.0000	0.998	0.001	0.999	0.1	0.2
Loose	None	0.9998	0.0000	1.000	0.001	1.000	0.1	0.1

J/Ψ->μμ, Block2

Mode		eff Table		eff Data		eff D / eff T	sys err corr	sys err uncorr
Vtight	Vtight	0.4679	0.0006	0.431	0.012	0.921	2.7	8.4
Tight	Tight	0.5128	0.0006	0.468	0.012	0.913	2.7	9.1
Loose	Loose	0.7471	0.0005	0.722	0.016	0.966	2.2	4.1
Vloose	Vloose	0.8331	0.0005	0.829	0.021	0.995	2.6	2.6
Mip	Mip	0.9891	0.0001	0.990	0.012	1.001	1.2	1.2
Tight	Loose	0.7251	0.0005	0.694	0.013	0.958	1.9	4.6
Loose	Vloose	0.8307	0.0004	0.825	0.020	0.993	2.4	2.5
Loose	Mip	0.9721	0.0001	0.969	0.011	0.996	1.1	1.1
Loose	None	0.9816	0.0001	0.977	0.006	0.996	0.6	0.7

Table 4.10: Block 2 only. Inclusive J/ψ yields (N fit *and* N corrected), additive corrections to the yields (Corr), lepton and J/ψ efficiencies observed in data (eff Data) and from particle identification tables (eff Table), correction factor (eff D / eff T), systematic errors if the efficiency correction is applied (sys err corr) and if the correction is not applied (sys err uncorr).

daughters of the J/ψ.

4.6 Total Reconstruction Efficiencies

Reconstruction efficiency for each final state is presented as a product of independent component efficiencies. A systematic error is assigned to each, which simplifies the calculation of the total systematic error. To avoid double counting, systematic errors are divided into uncorrelated (different for e^+e^- and $\mu^+\mu^-$ modes of each final state) and common (the same for e^+e^- and $\mu^+\mu^-$ modes).

4.6.1 $J/\psi \to \ell^+\ell^-$

$$\epsilon_R^{J/\psi} = \epsilon_A \cdot \epsilon_M \cdot \epsilon_T \cdot \epsilon_P \cdot \mathcal{B}_{\ell^+\ell^-}. \tag{4.12}$$

ϵ_A is the acceptance efficiency, calculated from Monte Carlo. It is the fraction of $J/\psi \to \ell^+\ell^-$ events with both daughters in the angular acceptance used by the analysis. A possible source of systematic error is a difference in J/ψ center of mass momentum (p^*) distributions in data and Monte Carlo, combined with a dependence of the acceptance efficiency on p^*. By comparing data and Monte Carlo p^* distributions, convoluted with the efficiency, we observe only a negligible effect, $< 0.2\%$.

ϵ_M is the probability that the mass of the lepton pair (after Bremsstrahlung recovery, if appropriate) falls in the histogram window. For the muon mode we use the Monte Carlo value, whereas for the electron mode it is a function of the Bremsstrahlung parameters. Systematic errors are 0.1% and 0.3% respectively.

ϵ_T is the probability that both lepton tracks satisfy the tracking criteria. As this quantity is not well modeled in Monte Carlo, we apply a correction factor prescribed by the tracking group. The systematic error on the efficiency is 0.1% but the uncertainty in the correction is 2.4%. This is the dominant systematic uncertainty in the J/ψ reconstruction.

ϵ_P is the particle identification efficiency calculated in Section 4.5. Systematic error is 1.4% for muons and 1.8% for electrons.

$\mathcal{B}_{\ell^+\ell^-}$ is the PDG branching fraction for J/ψ decaying into a lepton pair. We assume that the e^+e^- and $\mu^+\mu^-$ branching fractions are the same and use the average value of $(5.91 \pm 0.10)\%$ [G+00].

4.6.2 $\psi(2S) \to \ell^+\ell^-$

Reconstruction efficiency is calculated in a manner identical to $J/\psi \to \ell^+\ell^-$. As discussed in Section 4.8, instead of increasing the statistics in $B \to \psi(2S)X$ branching fraction calculation we use the reconstructed leptonic decays of the $\psi(2S)$ to calculate $\psi(2S) \to \ell^+\ell^-$ branching fractions.

4.6.3 $\psi(2S) \to \pi^+\pi^- J/\psi$

Reconstruction efficiency is calculated starting from the J/ψ reconstruction efficiency ($\epsilon_R^{J/\psi}$) of Equation 4.12. Additional factors are included.

$$\epsilon_{\psi(2S)} = \epsilon_R^{J/\psi} \cdot \epsilon_W \cdot \epsilon_A \cdot \epsilon_{\pi\pi} \cdot \epsilon_V \cdot \epsilon_{\Delta M} \cdot \mathcal{B}_{\psi(2S)\to\pi^+\pi^- J/\psi}. \tag{4.13}$$

ϵ_W is the fraction of J/ψ in the histogram range that fall in the tighter mass window required for $\psi(2S)$ reconstruction. It is calculated by integrating the J/ψ mass PDF over the appropriate range. It has a small error, 0.5% for

electrons and 0.3% for muons, due to the uncertainty in the offset, smearing and Bremsstrahlung parameters.

ϵ_A is the probability that two pions are in the fiducial volume, given a J/ψ in the mass window. It is calculated from Monte Carlo and has a 0.5% uncertainty.

$\epsilon_{\pi\pi}$ is the probability of a pion pair being reconstructed with a mass in the required window. Monte Carlo value is compared to the $\pi\pi$ invariant mass distribution measured by the BES experiment [B+01]. We correct for the 0.7% difference and assign the systematic error of the same magnitude.

ϵ_V is the probability of the four charged tracks being successfully vertexed, with a χ^2 probability greater than 1%. The value is estimated from Monte Carlo and a 4% systematic error is assigned.

$\epsilon_{\Delta M}$ is the probability of the mass difference ($\psi(2S)$-J/ψ) falling in the histogram mass range, estimated from Monte Carlo. It has a negligible systematic error.

$\mathcal{B}_{\psi(2S)\to\pi^+\pi^- J/\psi}$ is the PDG branching fraction: 0.310 ± 0.028 [G+00].

4.6.4 $\chi_c \to \gamma J/\psi$

Again, reconstruction efficiency is calculated starting with the J/ψ component.

$$\epsilon_{\chi_c} = \epsilon_R^{J/\psi} \cdot \epsilon_W \cdot \epsilon_\gamma \cdot \epsilon_{\Delta M} \cdot \mathcal{B}_{\chi_c \to \gamma J/\psi}. \tag{4.14}$$

ϵ_W is as for $\psi(2S) \to \pi^+\pi^- J/\psi$.

ϵ_γ is the efficiency for the photon to pass the selection criteria. Monte Carlo value is corrected by a factor of 0.975, as prescribed by the neutral identification group, to account for observed differences with respect to data. A 1.6% systematic is assigned to the correction.

$\epsilon_{\Delta M}$ is the probability of the mass difference (χ_c-J/ψ) falling in the histogram mass range, estimated from Monte Carlo.

$\mathcal{B}_{\chi_c \to \gamma J/\psi}$ is the PDG branching fraction for either χ_{c1} or χ_{c2} decaying into the $\gamma J/\psi$ final state. The values are 0.273 ± 0.016 and 0.135 ± 0.011 respectively [G+00].

4.7 Branching Fractions in B Decays

4.7.1 Total Branching Fractions

The number of mesons produced in each final state is calculated using the fit yields and reconstruction efficiencies described in Section 4.6. The number of mesons produced in B decay is obtained by subtracting the off-resonance yield scaled up to the on-resonance luminosity. (Table 4.3.) Equation 4.1 is used to calculate the branching fraction for each final state. Statistically independent measurements are obtained from e^+e^- and $\mu^+\mu^-$ samples in each final state:

$$\mathcal{B}^{ee} \pm \sigma^{ee}_{\rm stat} \pm \sigma^{ee}_{\rm sys} \pm \sigma^{\rm common}_{\rm sys}, \text{ and } \mathcal{B}^{\mu\mu} \pm \sigma^{\mu\mu}_{\rm stat} \pm \sigma^{\mu\mu}_{\rm sys} \pm \sigma^{\rm common}_{\rm sys}. \tag{4.15}$$

where systematic errors common to both lepton states are kept separate from those unique to only one lepton mode. The measurements are combined using the statistical and unique systematic errors:

$$\mathcal{B} = \left(w^{ee} \cdot \mathcal{B}^{ee} + w^{\mu\mu} \cdot \mathcal{B}^{\mu\mu}\right) / \left(w^{ee} + w^{\mu\mu}\right), \tag{4.16}$$

where

$$w^{\ell^+\ell^-} = 1/\left[\left(\sigma^{\ell^+\ell^-}_{\rm stat}\right)^2 + \left(\sigma^{\ell^+\ell^-}_{\rm sys}\right)^2\right]. \tag{4.17}$$

with $\ell^+\ell^-$ standing for either e^+e^- or $\mu^+\mu^-$. Uncertainty in the combined measurement due to statistical and unique systematic errors is

$$\sigma_{\rm comb} = 1/\sqrt{w^{ee} + w^{\mu\mu}}. \tag{4.18}$$

We separate statistical and systematic components of the combined error as:

$$1/\sigma^2_{\rm stat} = 1/\left(\sigma^{ee}_{\rm stat}\right)^2 + 1/\left(\sigma^{\mu\mu}_{\rm stat}\right)^2 \text{ and} \quad (4.19)$$

$$\sigma^{\rm combined}_{\rm sys} = \sqrt{\sigma^2_{\rm comb} - \sigma^2_{\rm stat}}. \quad (4.20)$$

The total systematic error on the measured branching fraction is derived from the combined and unique systematic errors:

$$\sigma_{\rm sys} = \sqrt{\sigma^{\rm combined^2}_{\rm sys} + \sigma^{\rm common^2}_{\rm sys}}. \quad (4.21)$$

Detailed calculations, including all efficiencies and a clear break down of systematic errors, are shown in Tables 4.11 to 4.14.

4.7.2 Direct Branching Fractions

Calculated J/ψ and χ_{c1} branching fractions include contributions from decays of higher mass states, such as $\psi(2S)$. This component is called feed-down. Direct meson production, with a reconstructed Charmonium meson coming directly from the B decay, is more easily calculable within the present theoretical framework. This makes it an interesting complementary measurement to total branching fraction. Using the yields and efficiencies presented previously, we calculate direct contributions by subtracting the feed-down. The following feed-down channels are considered: $\psi(2S)$ and χ_{c1} into J/ψ, and $\psi(2S)$ into χ_{c1}:

$$N_{J/\psi} \text{ from } \chi_{c1} = N_{\chi_{c1}} \cdot \mathcal{B}(\chi_{c1} \to \gamma J/\psi)/\epsilon_R^{\chi_{c1}} \quad (4.22)$$

$$= N_{\chi_{c1}}/\epsilon_R^{J/\psi} \cdot \epsilon_W \cdot \epsilon_\gamma \cdot \epsilon_{\Delta M} \quad (4.23)$$

$$N_{J/\psi} \text{ from } \psi(2S) = N_{\psi(2S)} \cdot \mathcal{B}(\psi(2S) \to J/\psi X)/\epsilon_R^{\psi(2S)}. \quad (4.24)$$

$$N_{\chi_{c1}} \text{ from } \psi(2S) = N_{\psi(2S)} \cdot \mathcal{B}(\psi(2S) \to \gamma\chi_{c1})/\epsilon_R^{\psi(2S)}. \quad (4.25)$$

We assume that the contribution from χ_{c2} and higher charmonium states (above open charm) are negligible since their production cross-sections are expected to

Table 4.11: Summary of the calculation of the $B \to J/\psi X$ branching fraction.

Inclusive J/ψ Branching Fraction; Run 1		**Electrons** Value	Stat error	%	Sys error	%	**Muons** Value	Stat error	%	Sys error	%	Common Sys %
eff-A	acceptance	0.753					0.753					0.2
eff-m	mass window	0.941				0.2	0.973				0.1	
eff-GTL	GoodTracksLoose	0.969				0.1	0.976				0.1	
eff-P	particle ID (tight/verytight for ee, loose/tight for muons)	0.905			0.016	1.8	0.717			0.010	1.4	
eff-Tcor	tracking efficiency correction	0.975					0.975					2.4
eff-cuts		*0.606*			*0.0111*	*1.8*	*0.500*			*0.0071*	*1.4*	*2.4*
B.F.	J/ψ to leptons BF average	0.0591					0.0591					1.2
eff-J/ψ	*total efficiency*	*0.0358*			*0.0007*	*1.8*	*0.0295*			*0.0004*	*1.4*	*2.7*
N-J/ψ	after cont subtraction	15575	292	1.9		0.8	13161	208	1.6		1.0	
N-J/ψ-0	*produced J/ψ*	*435,088*	*8166*	*1.9*	*8666*	*2.0*	*446,136*	*7061*	*1.6*	*7672*	*1.7*	*2.7*
eff-BB/eff-c	ratio of event efficiency	1.023					0.993					1.1
NBB	BB events passing cuts	21260000					21260000					1.1
B.F.	*branching fractions*	*0.0105*	*0.0002*	*1.9*	*0.0002*	*2.0*	*0.0104*	*0.0002*	*1.6*	*0.0002*	*1.7*	*3.1*

Ratio of μμ and ee Branching Fractions:

	0.0105	0.0003	2.7	comb. ee error
ratio μμ/ee	**0.995**	**0.036**	**3.6**	**combined error**
	0.0104	0.0002	2.3	comb. μμ error

Combined ee and μμ Branching Fractions:

combined B.F.	0.0104	0.0002	1.8 combined
statistical part of combined error		0.0001	1.2
systematics part of combined error		0.0001	1.3
total systematic error		0.0004	3.4
Final Branching Fraction	**0.01044**	**0.00013**	**1.2** **0.00035** **3.4**

Table 4.12: Summary of the calculation of the $B \to \psi(2S)X$ branching fraction.

Inclusive ψ(2s) Branching Fraction from J/ψ ππ		**Electrons** Value	Stat error	%	Sys error	%	**Muons** Value	Stat error	%	Sys error	%	Common Sys %
pion cuts:												
eff-A	acceptance for ππ	0.533					0.533					0.5
eff-ππ	mass window: 0.45 to 0.6	0.862					0.862					0.3
corr-BES	BES correction	1.007					1.007					0.7
J/ψ cuts:												
eff-J/ψ	Total eff for J/ψ	0.036			0.001	1.8	0.029			0.000	1.4	0.6
eff-window	window: 3.05 to 3.12 for J/ψ to ee, 3.07 to 3.12 to μμ.	0.740				0.5	0.914				0.3	
addition overall cuts:												
eff-dm	delta M window	0.999					0.999					0.0
eff-V	vertexing. 1% sys per track	0.874					0.884					4.0
eff-cuts		*0.0107*			*0.0002*	*1.9*	*0.0110*			*0.0002*	*1.4*	*4.2*
B.F.	ψ(2S) to J/ψ ππ	0.310					0.310					9.0
eff- ψ(2s)	*total efficiency*	*0.0033*			*0.0001*	*1.9*	*0.0034*			*0.0000*	*1.4*	*9.9*
N-fit	from fit, cont subtraction	405	40	9.9		2.8	392	41	11		5.4	
N- ψ(2s)-0	*produced ψ(2s)*	*121,934*	*12,088*	*9.9*	*4,105*	*3.4*	*114,622*	*12,059*	*11*	*6,411*	*5.6*	*9.9*
e-BB/e-c	ratio of event efficiency	0.987					0.982					1.1
NBB	BB events passing cuts	21260000					21260000					1.1
B.F.	*branching fractions*	*0.0028*	*0.0003*	*9.9*	*0.0001*	*3.4*	*0.0026*	*0.0003*	*11*	*0.0001*	*5.6*	*10.1*

Ratio of μμ and ee Branching Fractionss:

	0.0028	0.0003	10 comb. ee error	0.0026	0.0003	12 comb. μμ error
ratio μμ/ee	**0.94**	**0.15**	**16 combined error**			

Combined ee and μμ Branching Ratios:

combined B.F.	0.0027	0.0002	8 combined		
statistical part of combined error		0.0002	7		
systematics part of combined error		0.0001	3		
total systematic error		0.0003	11		
Final Branching Fraction	**0.00274**	**0.00020**	**7.2**	**0.00029**	**10.5**

Table 4.13: Summary of the calculation of the $B \to \chi_{c1} X$ branching fraction.

Inclusive χc1 Branching Fraction		Electrons					Muons					Common
		Value	Stat error	%	Sys error	%	Value	Stat error	%	Sys error	%	Sys %
photon cuts:												
eff-A	acceptance for γ	0.833					0.833					0.3
eff-O	other γ cuts	0.552					0.552					0.6
eff-corr	γ efficiency correction	0.975					0.975					1.3
J/ψ cuts:												
eff-J/ψ	Total eff for J/ψ	0.036			0.001	1.8	0.029			0.000	1.4	0.3
eff-window	window: 3.05 to 3.12 for J/ψ to ee, 3.07 to 3.12 to μμ.	0.740				0.5	0.914				0.3	
additional overall cuts:												
eff-dm	delta M window: 0.25 to 0.65	0.994					0.994					0.1
eff-cuts		*0.0118*			*0.0002*	*1.9*	*0.0120*			*0.0002*	*1.4*	*1.5*
B.F.	χc1 to J/ψ γ	0.273					0.273					5.9
eff-χc1	*total efficiency*	*0.0032*			*0.0001*	*1.9*	*0.0033*			*0.0000*	*1.4*	*6.0*
N-fit	from fit, cont subtraction	471	71	15.2		3.3	545	60	11.0		3.5	
N-χc1-0	*produced χc1*	*146,289*	*22,186*	*15.2*	*5,514*	*3.8*	*166,154*	*18,310*	*11.0*	*6,364*	*3.8*	*6.0*
e-BB/e-c	ratio of event efficiency	1.041					1.000					1.1
NBB	BB events passing cuts	21260000					21260000					1.1
B.F.	*branching fractions*	*0.0036*	*0.0005*	*15.2*	*0.0001*	*3.8*	*0.0039*	*0.0004*	*11.0*	*0.0001*	*3.8*	*6.2*

Ratio of μμ and ee Branching Fractions:

	0.0036	0.0006	16 comb. ee error	0.0039	0.0005	12 comb. μμ error
ratio μμ/ee	**1.09**	**0.21**	**20 combined error**		

Combined ee and μμ Branching Fractions:

combined B.F.	0.0038	0.0004	9 combined		
statistical part of combined error		0.0003	9		
systematics part of combined error		0.0001	3		
total systematic error		0.0003	7		
Final Branching Fraction	**0.00378**	**0.00034**	**8.9**	**0.00026**	**6.8**

Table 4.14: Summary of the calculation of the $B \to \chi_{c2} X$ branching fraction.

Inclusive χc2 Branching Fraction		**Electrons** Value	Stat error	%	Sys error	%	**Muons** Value	Stat error	%	Sys error	%	Common Sys %
photon cuts:												
eff-A	acceptance for γ	0.842					0.842					0.3
eff-O	other γ cuts	0.563					0.563					0.7
eff-corr	γ efficiency correction	0.975					0.975					1.3
J/ψ cuts:												
eff-J/ψ	Total eff for J/ψ	0.036			0.001	1.8	0.029			0.000	1.4	0.3
eff-window	window: 3.05 to 3.12 for J/ψ to ee, 3.07 to 3.12 to μμ.	0.740				0.5	0.914				0.3	
additional overall cuts:												
eff-dm	delta M window: 0.25 to 0.65	0.994					0.994					0.1
eff-cuts		*0.0122*			*0.0002*	*1.9*	*0.0124*			*0.0002*	*1.4*	*1.5*
B.F.	χc2 το J/ψ γ	0.135					0.135					8.1
eff-χc2	*total efficiency*	*0.0016*			*0.0000*	*1.9*	*0.0017*			*0.0000*	*1.4*	*8.3*
N-fit	from fit, cont subtraction	104	56	53.5		3.3	86	59	68.3		3.5	
N-χc2-0	*produced χc2*	*63,286*	*33,870*	*53.5*	*2,385*	*3.8*	*51,454*	*35,164*	*68.3*	*1,971*	*3.8*	*8.3*
e-BB/e-c	ratio of event efficiency	1.035					0.997					1.1
NBB	BB events passing cuts	21260000					21260000					1.1
B.F.	*branching fractions*	*0.0015*	*0.0008*	*53.5*	*0.0001*	*3.8*	*0.0012*	*0.0008*	*68.3*	*0.0000*	*3.8*	*8.4*

Ratio of μμ and ee Branching Fractions:

	0.0015	0.0008	54	comb. ee error	
ratio μμ/ee	**0.78**	**0.68**	**87**	**combined error**	
	0.0012	0.0008	68	comb. μμ error	

Combined ee and μμ Branching Fractions:

combined B.F.	0.0014	0.0006	43	combined
statistical part of combined error		0.0006	42	
systematics part of combined error		0.0000	3	
total systematic error		0.0001	9	
Final Branching Fraction	**0.00137**	**0.00058**	**42.5**	**0.00012** **8.9**

be small. After the subtraction, calculations proceed similarly to those of Section 4.7.1. Details are shown in Tables 4.15 and 4.16.

4.7.3 Branching Ratios

Another quantity of interest is the inclusive branching ratio (a ratio of inclusive branching fractions) of higher charmonium mesons to the J/ψ. Finding the true error is non trivial because of common systematic errors, such as tracking and particle identification, entering individual branching fraction calculations. Treating systematic errors as independent would overestimate the total systematic error.

Calculations of $\psi(2S)$ to J/ψ branching ratio and χ_{c1} to J/ψ branching ratio are presented in Tables 4.17 and 4.18.

4.7.4 Summary of Results

A summary of inclusive B to charmonia branching fractions is presented in Table 4.19. The second column tabulates the ratio of branching fractions (or branching ratios) calculated for the $\mu^+\mu^-$ and e^+e^- modes independently. All values are, within errors, consistent with one, thus increasing our confidence in the components of reconstruction efficiencies that depend on the lepton species.

Measured $\chi_{c2} \to \gamma J/\psi$ branching fraction is not statistically significant. We convert the measurement into an upper limit with 90% confidence level. The upper limit, x_L, is the value satisfying the following condition:

$$\frac{\int_0^{x_L} G(x;\mu,\sigma)dx}{\int_0^{\infty} G(x;\mu,\sigma)dx} = \text{C.L.}, \tag{4.26}$$

where $G(x;\mu,\sigma)$ is a Gaussian with mean μ and standard deviation σ and C.L. is the desired confidence level. Values of μ and σ are the central value of the

Table 4.15: Summary of the calculation of the direct $B \to J/\psi X$ branching ratio.

Direct J/ψ Branching Fraction		**Electrons**					**Muons**					Common
		Value	Stat error	%	Sys error	%	Value	Stat error	%	Sys error	%	Sys %
eff-J/ψ	*total efficiency*	*0.0358*				*1.8*	*0.0295*				*1.4*	*2.7*
N-J/ψ	after cont subtraction	15575	292	1.9		0.8	13161	208	1.6		1.0	
N-J/ψ-0	*produced J/ψ*	*435,088*	*8166*	*1.9*	*8666*	*2.0*	*446,136*	*7061*	*1.6*	*7672*	*1.7*	*2.7*
N-fit-χc1	from fit, cont subtraction	471	71	15.2	15	3.3	545	60	11.0	19	3.5	
eff-window	window: 3.05 to 3.12 for J/ψ to ee, 3.07 to 3.12 to μμ.	0.740				0.5	0.914				0.3	
eff-dm	delta M window: 0.25 to 0.65	0.994					0.994					0.1
eff-γ	all γ cuts	0.448					0.448					0.7
N-J/ψ-FD1	*feed-down from χc1*	*39,937*	*6057*	*15.2*	*1505*	*3.8*	*45,360*	*4999*	*11.0*	*1738*	*3.8*	*2.8*
N-fit-ψ(2S)	from fit, cont subtraction	405	40	9.9	11	2.8	392	41	11	21	5.4	
B.F.	ψ(2S) to J/ψ X	0.550					0.550					9.1
eff-ψ(2S)		0.0033				1.9	0.0034				1.4	9.9
N-J/ψ-FD2	*feed-down from ψ(2S)*	*67,064*	*6648*	*9.9*	*2258*	*3.4*	*63,042*	*6632*	*10.5*	*3526*	*5.6*	*13.5*
N-J/ψ-DIR	*direct*	*328,087*	*12148*	*3.7*	*9081*	*2.8*	*337,734*	*10901*	*3.2*	*8621*	*2.6*	*4.4*
eff-BB/eff-c	ratio of event efficiency	1.023					0.993					1.1
NBB	BB events passing cuts	21260000					21260000					1.1
B.F.	*branching fractions*	*0.0079*	*0.0001*	*1.9*	*0.0002*	*2.8*	*0.0079*	*0.0001*	*1.6*	*0.0002*	*2.6*	*4.7*

Ratio of μμ and ee Branching Fractions:

	0.0079	0.0003	3.3	comb. ee error	0.0079	0.0002	3.0	comb. μμ error
ratio μμ/ee	**0.999**	**0.045**	**4.5**	**combined error**				

Combined ee and μμ Branching Fractions:

combined B.F.	0.0079	0.0002	2.2	combined
statistical part of combined error		0.0001	1.2	
systematics part of combined error		0.0001	1.9	
total systematic error		0.0004	5.1	
Final Branching Fraction	**0.00789**	**0.00010**	**1.2**	**0.00040**	**5.1**

Direct χc1 Branching Fraction		Electrons					Muons					Common
		Value	Stat error	%	Sys error	%	Value	Stat error	%	Sys error	%	Sys %
eff-χc1	*total efficiency*	*0.0032*			*0.0001*	*1.9*	*0.0033*			*0.0000*	*1.4*	*6.0*
N-fit	from fit, cont subtraction	471	71	15.2		3.3	545	60	11.0		3.5	
N-χc1-0	*produced χc1*	*146,289*	*22,186*	*15.2*	*5,514*	*3.8*	*166,154*	*18,310*	*11.0*	*6,364*	*3.8*	*6.0*
N-fit-ψ(2S)	from fit, cont subtraction	*405*	*40*	*9.9*	*11*	*2.8*	*392*	*41*	*10.5*	*21*	*5.4*	
B.F.	ψ(2S) to χc1 γ	*0.0870*					*0.0870*					*9.2*
eff-ψ(2S)		*0.0033*				*1.9*	*0.0034*				*1.4*	*9.9*
N-χc1-FD	*feed-down from ψ(2S)*	*10,608*	*1,052*	*9.9*	*357*	*3.4*	*9,972*	*1,049*	*10.5*	*558*	*5.6*	*13.5*
N-χc1-DIR	*direct*	*135,681*	*22,211*	*16.4*	*5,525*	*4.1*	*156,181*	*18,340*	*11.7*	*6,389*	*4.1*	*6.5*
e-BB/e-c	ratio of event efficiency	1.041					1.000					1.1
NBB	BB events passing cuts	21260000					21260000					1.1
B.F.	*branching fractions*	*0.0033*	*0.0005*	*16.4*	*0.0001*	*4.1*	*0.0037*	*0.0004*	*11.7*	*0.0002*	*4.1*	*6.2*

Ratio of μμ and ee Branching Fractions:

	0.0033	0.0006	17	comb. ee error	0.0037	0.0005	12 comb. μμ error
ratio μμ/ee	**1.11**	**0.23**	**21**	**combined error**			

Combined ee and μμ Branching Fractions:

combined B.F.	0.0035	0.0004	10	combined
statistical part of combined error		0.0003	10	
systematics part of combined error		0.0001	3	
total systematic error		0.0002	7	
Final Branching Fraction	**0.00353**	**0.00034**	**9.6**	**0.00024** **6.9**

Table 4.16: Summary of the calculation of the direct $B \to \chi_{c1} X$ branching ratio.

Table 4.17: Summary of the calculation of the $B \to \psi(2S)X$ to $B \to J/\psi X$ branching ratio.

ψ(2S) to J/Ψ Branching Ratio		**from ee**					**from μμ**					Common Sys %
		Value	Stat error	%	Sys error	%	Value	Stat error	%	Sys error	%	
eff-w	window: 3.05 to 3.12 for J/ψ to ee, 3.07 to 3.12 to μμ.	0.740				0.5	0.914				0.3	
eff-A	acceptance for ππ	0.533					0.533					0.5
eff-m	mass window: 0.45 to 0.6	0.862					0.862					0.3
corr-BES	BES correction	1.007					1.007					0.7
eff-dm	delta M window: 0.5 to 0.7	0.999					0.999					0.0
eff-V	vertexing. 1% sys per track	0.874					0.884					4.0
eff- ψ (2s)J/ ψππ		*0.299*			*0.0014*	*0.5*	*0.374*			*0.0010*	*0.3*	*4.1*
eff-J/ψ/eff-ψ(2S	ratio of event efficiency	0.965					0.989					
B.F.	ψ(2S) to J/ψ ππ	0.310					0.310					9.0
N-Fit	J/ψ to ll, continuum subtracted	15575	292			0.8	13161	208			1.0	
N-Fit	ψ(2S) to J/ψ ππ, cont. subtracted	405	40	9.9		2.8	392	41	10.5		5.4	
B.R.	*ψ (2S) to J/ψ branching ratios*	*0.2703*	*0.0268*	*9.9*	*0.0079*	*2.9*	*0.2541*	*0.0267*	*10.5*	*0.0140*	*5.5*	*9.9*

Ratio of μμ and ee Branching Ratios:

	0.2703	0.0279	10 comb. ee error	0.2541	0.0302	12 comb. μμ error
ratio μμ/ee	**0.94**	**0.15**	**16 comb error**			

Combined ee and μμ Branching Ratios:

combined B.R.	0.2628	0.0205	7.8 combined		
statistical part of combined error		0.0189	7.2		
systematics part of combined error		0.0079	3.0		
total systematic error		0.0272	10.4		
Final Branching Ratio	**0.263**	**0.019**	**7.2**	**0.027**	**10.4**

Table 4.18: Summary of the calculation of the $B \to \chi_{c1} X$ to $B \to J/\psi X$ branching ratio.

χc1 to J/Ψ Branching Ratio		**from ee**					**from μμ**					Common Sys %
		Value	Stat error	%	Sys error	%	Value	Stat error	%	Sys error	%	
eff-w	window: 3.05 to 3.12 for J/ψ to ee, 3.07 to 3.12 to μμ.	0.740				5.0	0.914				0.3	
eff-A	acceptance for γ	0.833					0.833					0.3
eff-O	other γ cuts	0.552					0.552					0.6
eff-corr	γ efficiency correction	0.975					0.975					1.3
eff-dm	delta M window: 0.25 to 0.65	0.994					0.994					0.1
eff-χc1		*0.329*			*0.0165*	*5.0*	*0.407*			*0.0011*	*0.3*	*1.4*
eff-J/ψ/eff-χc	ratio of event efficiency	1.018					1.007					
B.F.	χc1 to J/ψ γ	0.273					0.273					5.9
N-Fit	J/ψ to ll, continuum subtracted	15575	292			0.8	13161	208			1.0	
N-Fit	χc1 to J/ψ γ, cont. subtracted	471	71	15.2		3.3	545	60	11.0		3.5	
B.R.	*χc1 to J/ψ γ branching ratios*	*0.3421*	*0.0519*	*15.2*	*0.0206*	*6.0*	*0.3751*	*0.0413*	*11.0*	*0.0138*	*3.7*	*6.0*
Ratio of μμ and ee Branching Ratios:												
		0.3421	0.0558		16 comb. ee error		0.3751	0.0436		12 comb. μμ error		
	ratio μμ/ee	**1.10**	**0.22**		**20 comb error**							
Combined ee and μμ Branching Ratios:												
	combined B.R.	0.3626	0.0344		9.5 combined							
	statistical part of combined error		0.0323		8.9							
	systematics part of combined error		0.0116		3.2							
	total systematic error		0.0248		6.8							
	Final Branching Ratio	**0.363**	**0.032**		**8.9**	**0.025**	**6.8**					

Table 4.19: Summary of the inclusive B branching fractions (percent) to charmonium mesons calculated in this thesis. $\mu^+\mu^-/e^+e^-$ is the ratio of branching fractions (or branching ratios) calculated for the $\mu^+\mu^-$ and e^+e^- modes independently. Results are compared to the 2000 edition of the Particle Data Group results [G+00]. Quantities preceded by "<" are 90% upper confidence limits.

Meson	$\mu^+\mu^-/e^+e^-$	*Value*	*Statistical*	*Systematic*	*PDG2000*
J/ψ	0.995 ± 0.036	1.044	0.013	0.035	1.15 ± 0.06
J/ψ direct	0.999 ± 0.045	0.789	0.010	0.040	0.80 ± 0.08
$\psi(2S)$	0.93 ± 0.15	0.274	0.020	0.029	0.35 ± 0.05
$\psi(2S)/J/\psi$	0.95 ± 0.15	0.263	0.019	0.027	0.30 ± 0.05
χ_{c1}	1.09 ± 0.21	0.378	0.034	0.026	0.42 ± 0.07
χ_{c1} direct	1.11 ± 0.23	0.353	0.034	0.024	0.37 ± 0.07
$\chi_{c1}/J/\psi$	1.10 ± 0.22	0.363	0.032	0.025	0.32 ± 0.06
χ_{c2}	0.78 ± 0.68	0.137	0.058	0.012	-
χ_{c2} limit		< 0.21			< 0.38

measured χ_{c2} branching ratio and its total (statistical and systematic added in quadrature) error.

All measured branching fractions are consistent with current world averages, for each final state. The total error of our analysis is superior to the PDG value. The upper limit on the inclusive χ_{c2} production improves the PDG value.

4.8 $\psi(2S) \to \ell^+\ell^-$ Branching Fractions

Current errors on the PDG [G+00] values of the $\psi(2S) \to \ell^+\ell^-$ branching fractions are rather large: 14.7 % for $\mathcal{B}_{\psi(2S)\to e^+e^-}$ and 34.0 % for $\mathcal{B}_{\psi(2S)\to\mu^+\mu^-}$. There

exist more accurate measurements of the electron branching ratio done by E-760 [A+97b] and E-835 [A+00] experiments. PDG does not consider these measurements as independent and, therefore, does not include them in the world average. Using the inclusive $\psi(2S)$ sample we can measure the electron branching fraction to a precision comparable to the present world average. And we can make a significant improvement in the muon measurement.

Measurements of the $\psi(2S) \to \ell^+\ell^-$ are done by equating the number of produced $\psi(2S)$ mesons calculated from the observed $\psi(2S) \to \pi^+\pi^- J/\psi$ decays to the number calculated from the observed $\psi(2S) \to \ell^+\ell^-$ decays, and then solving for the two branching fractions. We do not require that a $\psi(2S)$ meson originate from a B decay. Therefore we use on-resonance yields (Table 4.3) before continuum subtraction. Two statistically independent measurements of the $\psi(2S) \to e^+e^-$ branching fraction (e^+e^- mode is used as an example, but the same applies to the $\mu^+\mu^-$ mode) are calculated according to:

$$\mathcal{B}_{\psi(2S)\to e^+e^-} = \mathcal{B}_{\psi(2S)\to\pi^+\pi^- J/\psi} \cdot \frac{N_{ee}}{N_{\pi\pi ee}} \cdot \frac{\epsilon_E^{\pi\pi ee}}{\epsilon_E^{ee}} \cdot \frac{\epsilon_C^{\pi\pi ee}}{\epsilon_C^{ee}} \tag{4.27}$$

$$\mathcal{B}_{\psi(2S)\to e^+e^-} = \mathcal{B}_{\psi(2S)\to\pi^+\pi^- J/\psi} \cdot \frac{N_{ee}}{N_{\pi\pi\mu\mu}} \cdot \frac{\epsilon_E^{\pi\pi\mu\mu}}{\epsilon_E^{ee}} \cdot \frac{\epsilon_C^{\pi\pi\mu\mu}}{\epsilon_C^{ee}}, \tag{4.28}$$

where N are fit yields, ϵ_E are event efficiencies and ϵ_C are cut efficiencies. Cut efficiencies are related to previously defined reconstruction efficiencies as:

$$\epsilon_R^{\psi(2S)\to\text{mode}} = \mathcal{B}_{\psi(2S)\to\text{mode}} \cdot \epsilon_C^{\psi(2S)\to\text{mode}}, \tag{4.29}$$

with the label 'mode' signifies any of the e^+e^-, $\mu^+\mu^-$, $e^+e^-\pi^+\pi^-$ or $\mu^+\mu^-\pi^+\pi^-$ channels.

B counting and tracking systematic errors cancel in all measurements, whereas particle identification systematic errors cancel in Equation 4.27 but not in Equation 4.28. The calculation is presented in Table 4.20. Note that in combining the results of Equations 4.27 and 4.28 we separate unique statistical errors (from $\psi(2S) \to \ell^+\ell^-$ fits) from the common statistical errors (from $\psi(2S) \to \pi^+\pi^- J/\psi$

Table 4.20: Summary of the calculation of the $\psi(2S) \to \ell^+\ell^-$ branching fractions.

ψ(2S) to ll Branching Fractions		**Electrons**					**Muons**					Common Sys %	Common Stat %
		Value	Stat error	%	Sys error	%	Value	Stat error	%	Sys error	%		
eff-ll	event efficiency	0.912					0.945						
eff-ππll	event efficiency	0.967					0.972						
eff-C-ll	cut efficiency	0.602				1.8	0.536				1.4		
eff-C-ππllxBF	cut efficiency x B.F.	0.0033				1.9	0.0034				1.4	9.9	
N-Fit	ψ(2S) to ll	552	50	9.1		3.6	437	44	10.1		8.2		
N-Fit	ψ(2S) to J/ψ ππ	405	37	9.1		2.8	400	34	8.5		5.4		
B.F.	*branching fractions ψ(2S) to ee*	*0.0080*	*0.0007*	*9.1*	*0.0002*	*2.8*	*0.0084*	*0.0007*	*8.5*	*0.0005*	*5.9*	*10.6*	*9.1*
B.F.	*branching fractions ψ(2S) to μμ*	*0.0068*	*0.0006*	*9.1*	*0.0003*	*3.7*	*0.0072*	*0.0006*	*8.5*	*0.0004*	*5.4*	*12.9*	*10.1*

Ratio of μμππ and eeππ Branching Fractions:

	branching fraction ψ(2S) to ee			**branching fraction ψ(2S) to μμ**		
	0.0080	0.0008	10 comb. ee error	0.0068	0.0007	10 comb. ee error
	0.0084	0.0009	10 comb. μμ error	0.0072	0.0007	10 comb. μμ error
ratio μμππ/eeππ	**1.05**	**0.15**	**14 comb error**	**1.05**	**0.15**	**14 comb error**

Combined eeππ and μμππ Branching Fractions:

	branching fraction ψ(2S) to ee					**branching fraction ψ(2S) to μμ**				
combined B.F.	0.0081	0.0006	7			0.0070	0.0005	7		
statistical part of combined error		0.0005	6				0.0004	6		
systematics part of combined error		0.0003	3				0.0002	3		
total statistical error		0.0009	11				0.0008	12		
total systematic error		0.0009	11				0.0009	13		
Final Branching Fraction	**0.00815**	**0.00090**	**11.0**	**0.00090**	**11.0**	**0.00700**	**0.00083**	**11.8**	**0.00093**	**13.3**

fits). Just as with systematic errors, this treatment avoids overestimating the total error.

Finally, we obtain the following values:

$$\mathcal{B}(\psi(2S) \to e^+e^-) = (0.815 \pm 0.090 \pm 0.090)\% \quad [(0.88 \pm 0.13)\ \%] \quad (4.30)$$

$$\mathcal{B}(\psi(2S) \to \mu^+\mu^-) = (0.700 \pm 0.083 \pm 0.093)\% \quad [(1.03 \pm 0.35)\ \%], \quad (4.31)$$

where the first error is statistical and the second is systematic. Current PDG values and their combined errors are shown in square brackets. Our combined error in the electron mode, 0.13 %, is comparable to the PDG value, but in the muon case our measurement, again with a 0.13 % combined error, is clearly superior.

4.9 Properties of Charmonium Mesons From B Decays

4.9.1 Momentum Distributions of Charmonium Mesons

We determine the center of mass momentum (p^*) distribution of J/ψ mesons by dividing the signal sample into p^* ranges and fitting mass distributions in each range. This procedure is more reliable than sideband subtraction as it does not depend on the background shape being the same in signal and sideband regions.

J/ψ momentum in the B frame would be a more interesting quantity but, as B mesons are not reconstructed in the inclusive analysis, this information is not available to us. The difference between p^* and the J/ψ momentum in the B frame is up to roughly 250 MeV/c, which is the average momentum of the B meson in the center of mass frame. Most of the interesting structure in the momentum

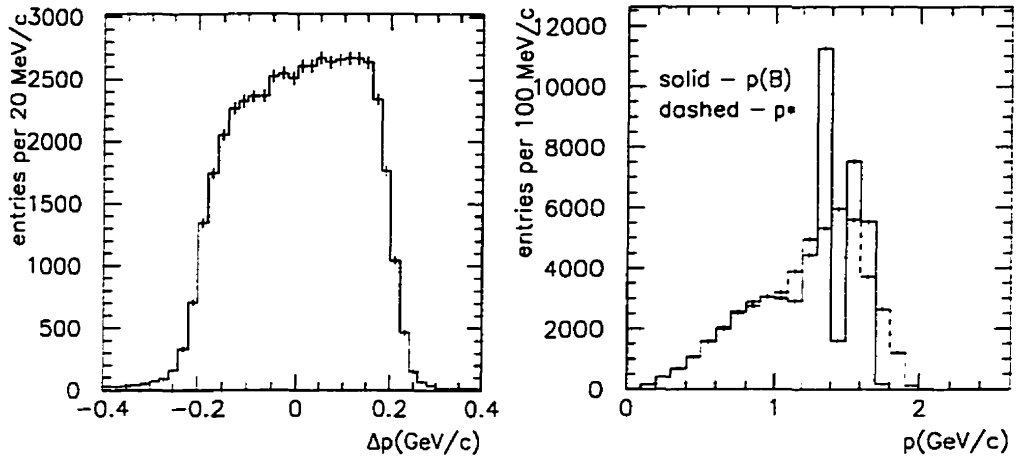

Figure 4.17: (a) difference between center of mass J/ψ momentum and the J/ψ momentum in the B rest frame, and (b) momentum in the B frame (solid histogram) overlaid with the p^* distribution (dashed histogram).

distribution, such as peaks from $B \to J/\psi K$ and $B \to J/\psi K^*$, is lost because of this 'resolution' factor. Figure 4.17 shows the difference between p^* and the J/ψ momentum in the B frame, as well as both distributions.

The on-resonance sample is divided in 200 MeV/c wide bins, limited by the p^* 'resolution' and not the statistics. The off-resonance sample, having much lower statistics, is divided in 600 MeV/c bins. Fits to each range are performed by allowing the number of signal events and the background parameters to float, while keeping all other parameters fixed. Signal yield in each p^* bin is corrected for reconstruction efficiency. As some efficiency components (acceptance and particle identification in particular) vary with p^*, we use the inclusive $B \to J/\psi X$ Monte Carlo sample (as before, corrected for the differences with respect to data) to model this dependence. Normalized efficiencies - that is efficiency of each p^* bin divided by the average efficiency - are shown in Figure 4.18. Efficiencies in the $p^* > 2$ GeV/c range are inaccessible to the J/ψ from B decays and, therefore, cannot be obtained from this Monte Carlo. We estimate their values by linearly

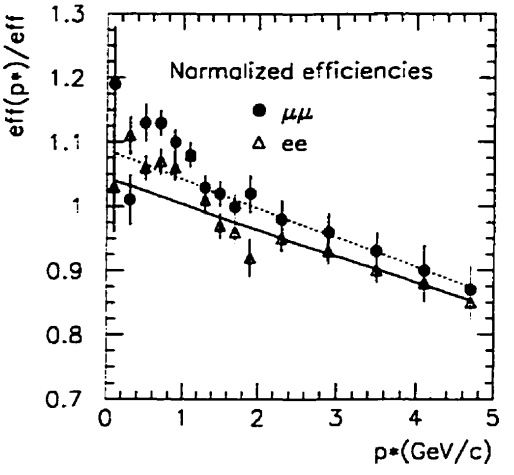

Figure 4.18: Electron and muon normalized reconstruction efficiencies. Linear extrapolation to the high p^* region is used.

extrapolating the $p^* < 2$ GeV/c region.

Plots of measured p^* distributions of J/ψ mesons are presented in Figure 4.19. On-resonance data and off-resonance data (scaled to the on-resonance luminosity) are shown in the two top plots. We can see that the off-resonance distribution saturates the on-resonance distribution in the $p^* > 2$ GeV/c range, as is expected because any difference could only be caused by the J/ψ coming from B decays. This cannot affect the $p^* > 2$ GeV/c region. However, this agreement shows there are no problems with fitting data samples much smaller than in Figure 4.10. The third plot shows the combined distribution ($\mu^+\mu^-$+e^+e^-) and the difference of two lepton modes ($\mu^+\mu^-$-e^+e^-), after continuum subtraction. Note that the difference in e^+e^- and $\mu^+\mu^-$ distributions is consistent with zero. Although it appears that might be a slight excess of electrons in the $p^* < 2$ GeV/c region, adding up the bin contents yields 52870 ± 543 events in the sum and -497 ± 543 events in the difference, yielding a muon to electron ratio of 0.981 ± 0.020, consistent with one. Therefore we can conclude that there are no problems with particle identification, including the extrapolation into the high p^* region. The last plot

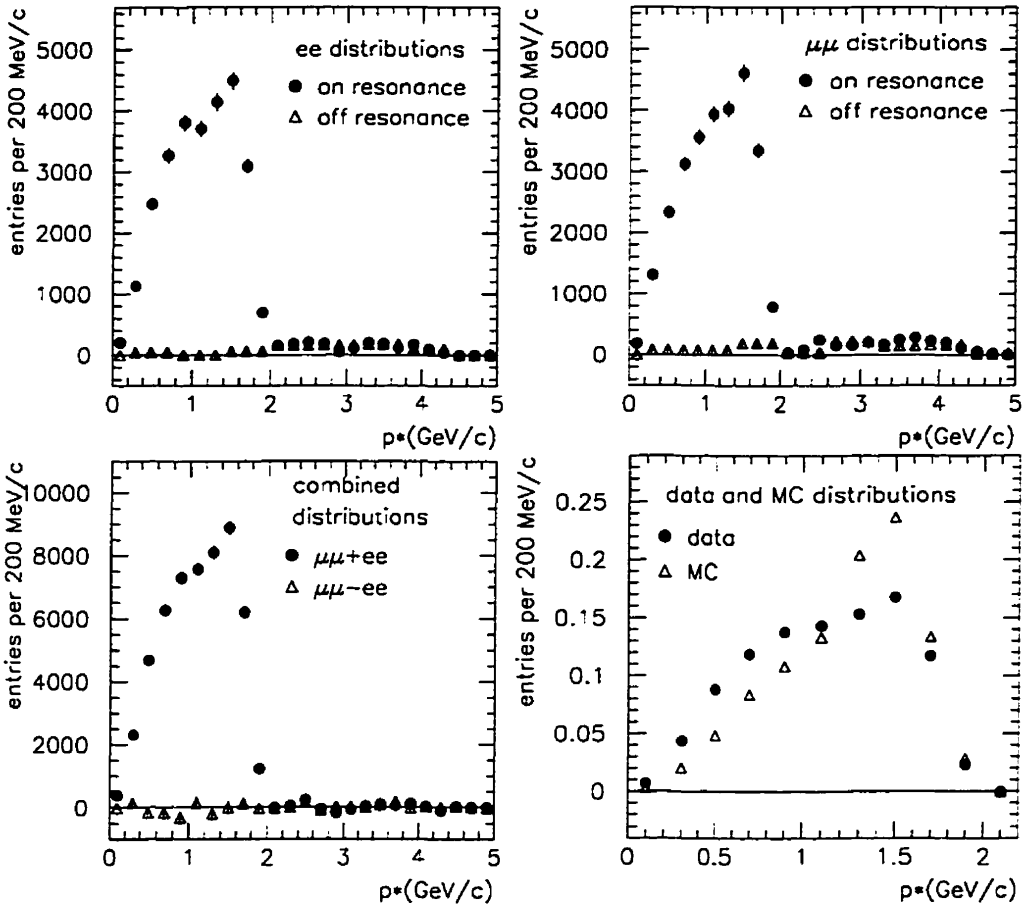

Figure 4.19: p^* distributions of reconstructed J/ψ for (a) e^+e^- only, (b) $\mu^+\mu^-$ only, (c) combined sample, and (d) comparison of data and Monte Carlo distributions in the p^* region accessible to B decays.

shows the difference between data and Monte Carlo distributions.

Differences between Monte Carlo and data p^* distributions, combined with the dependence of the reconstruction efficiency on p^*, could lead to incorrect calculation of the average efficiency used in the branching fraction calculation. However, convoluting the Monte Carlo and data distributions with the efficiency curve yields average efficiencies which agree to within 0.5%.

4.9.2 Measurements of J/ψ Polarization

The helicity angle of a J/ψ candidate is the angle (measured in the rest frame of the J/ψ) between the positively charged lepton and the direction of the J/ψ in the B rest frame. In principle, the positive lepton and a virtual particle traveling in the J/ψ direction are boosted from the B frame into the J/ψ rest frame, and the resulting angle is the helicity angle. We do not know the B rest frame so the $\Upsilon(4S)$ rest frame is used instead. The lepton and a J/ψ candidate are boosted from the lab frame into a $\Upsilon(4S)$ frame. Then the lepton is boosted into a J/ψ rest frame using a method that aligns the z axis with the J/ψ flight direction. Resulting polar angle of the lepton is the J/ψ helicity angle. Monte Carlo measured resolution (difference between J/ψ helicity in B and $\Upsilon(4S)$ rest frame) is 0.085 in $\cos\theta_H$. Cosine of the helicity angle ($\cos\theta_H$) is used in the analysis because J/ψ polarization is defined in terms of $\cos\theta_H$.

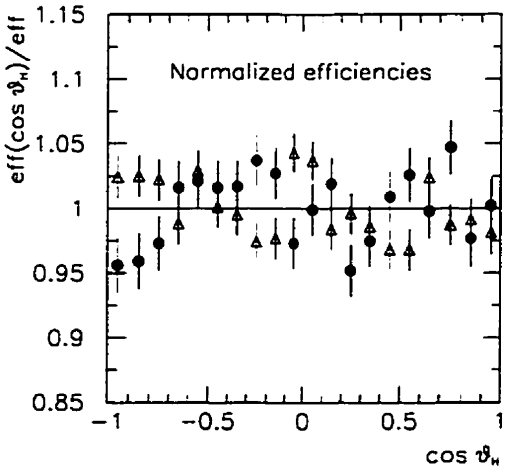

Figure 4.20: Variation of the reconstruction efficiency with J/ψ helicity.

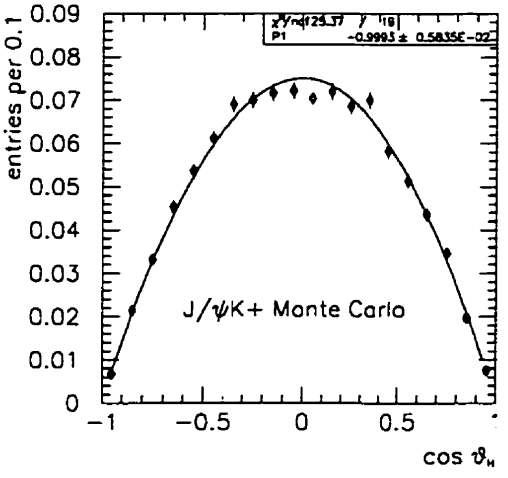

Figure 4.21: Fit to the helicity distribution of Monte Carlo $B \to J/\psi K^+$ events.

The analysis proceeds in a manner similar to the p^* analysis. On and off-resonance data are divided in $\cos\theta_H$ bins and invariant mass distributions are fit to extract

the yields. Off-resonance binning is four times coarser than the on-resonance binning. The variation of the reconstruction efficiency with $\cos\theta_H$ is obtained from inclusive J/ψ Monte Carlo (Figure 4.20), and no dependence is observed. Therefore, no additional efficiency corrections are applied to data. Note that we still apply particle identification, tracking and mass window corrections.

The probability density function (PDF) for $u = \cos\theta_H$ can be written in terms of the PDFs for the transverse ($h_T(u) = 3(1+u^2)/8$) and longitudinal ($h_L(u) = 3(1-u^2)/4$) polarizations as:

$$h(u) = f_T \cdot h_T(u) + f_L \cdot h_L(u), \tag{4.32}$$

where f_T and f_L are the fractions of mesons that are transversely and longitudinally polarized ($f_T + f_L = 1$). This expression can be reduced to a (normalized) function of a single polarization parameter, $A = (f_T - 2f_L)/(f_T + 2f_L)$, where $A = 0$ indicates unpolarized distribution, $A = 1$ indicates transversely polarized and $A = -1$ indicates longitudinally polarized:

$$h(u) = \frac{3}{2(A+3)}\left(1 + A \cdot u^2\right). \tag{4.33}$$

All $\cos\theta_H$ distributions are normalized to unit area and then fit to this PDF to extract the polarization parameter A.

The method is tested on Monte Carlo sample of $B \to J/\psi K^+$ events, in which the J/ψ is created as fully longitudinally polarized. The fit (Figure 4.21) returns $A = -0.9993 \pm 0.0058$, fully consistent with the expected value of -1. Another test is performed by adding a multiplicative normalization constant to the PDF in Equation 4.33 and redoing the fit with one additional parameter. The same value of A was found, with the normalization constant of $N = 0.9977 \pm 0.0073$.

On and off-resonance $\cos\theta_H$ distributions of $J/\psi \to e^+e^-$ and $J/\psi \to \mu^+\mu^-$ candidates are shown in the top two plots of Figure 4.22. The J/ψ polarization is

extracted from the combined ($e^+e^-+\mu^+\mu^-$) sample, after continuum subtraction. These are shown in the bottom two plots of Figure 4.22. To distinguish polarization in the two body inclusive J/ψ B decays (such as $B \to J/\psi K^{(*)}$) and the three body decays (such as $B \to J/\psi K\pi$) we divide the data into two p^* regions. A kinematic limit for center of mass momentum of the J/ψ from a two body B decay is roughly $p_{\rm CM} > 1.3$ GeV/c. As the observed p^* differs by up to about 200 MeV/c, we use the p^* of 1.1 GeV/c as the boundary of the two regions. Another justification for making this distinction is the momentum dependence of the theoretical predictions of J/ψ polarization.

Our measured polarization of the J/ψ mesons coming from B decays is: $A = -0.561 \pm 0.024$ for the J/ψ in the $p^* > 1.1$ GeV/c region, and, $A = -0.174 \pm 0.040$ for the J/ψ in the $p^* < 1.1$ GeV/c region. Smaller value of the polarization parameter in the high p^* region is reasonable, given the fact that $p^* > 1.1$ GeV/c is dominated by $B \to J/\psi K$ decays, which have longitudinally polarized J/ψ mesons.

4.10 J/ψ Production in Continuum

Meson selection and fitting procedure are identical to the ones described for the study of charmonia in B decays. Continuum production of J/ψ is observed in two data sets: off-resonance data and on-resonance data with a J/ψ center of mass momentum (p^*) above 2 GeV/c (beyond the kinematic limit for J/ψ mesons from B decays).

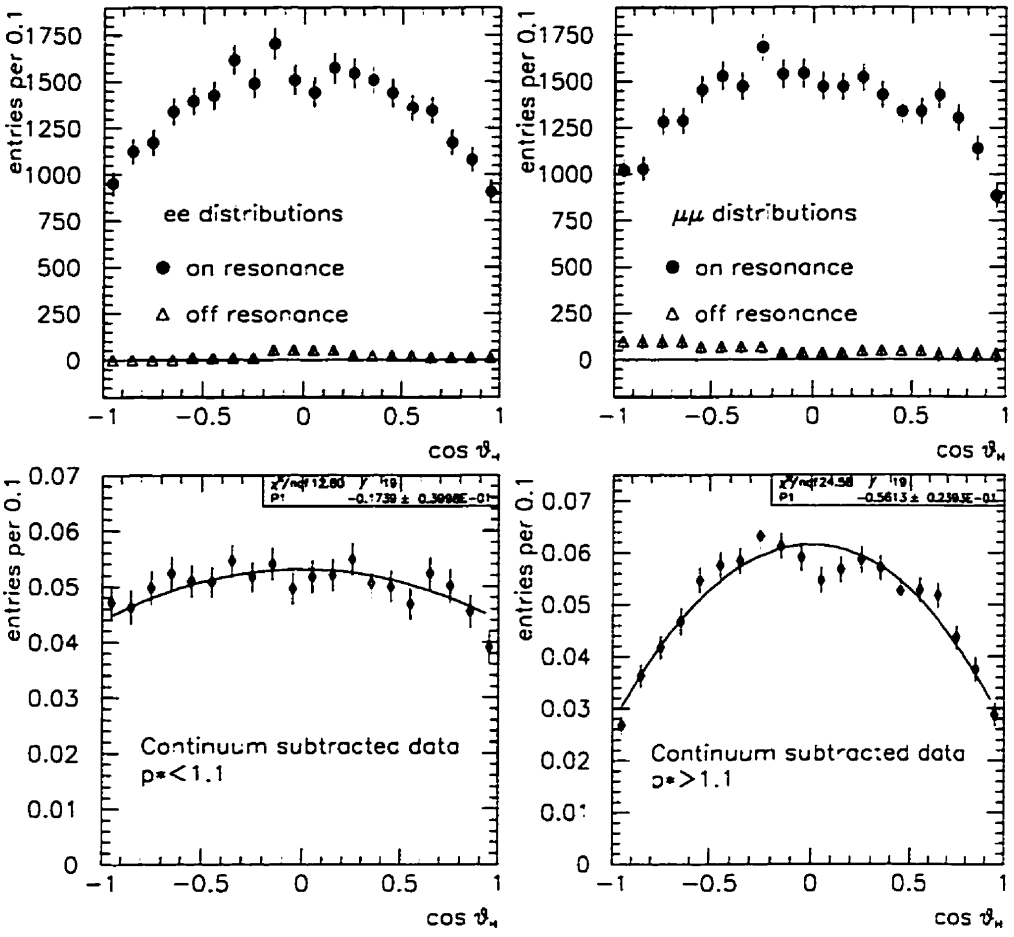

Figure 4.22: Helicity distributions of $J/\psi \to e^+e^-$ (a) and $J/\psi \to \mu^+\mu^-$ (b) candidates in on-resonance and off-resonance data. Fits to continuum subtracted combined ($e^+e^-+\mu^+\mu^-$) helicity distributions for $p^* < 1.1$ GeV/c (c) and $p^* > 1.1$ GeV/c (d) candidates.

4.10.1 Event Selection

In this part of the analysis we use a loosened version of the event selection described in Section 4.2. By relaxing two cuts, $ETotFid > 4$ GeV and $R2All < 0.95$ (as defined in Section 4.2), we are able to study backgrounds in the regions rejected by the standard selection.

Distributions of event quantities for signal J/ψ are obtained by sideband subtraction. A distribution obtained from background events in the mass sideband region, $3.14 < m < 3.3$ GeV/c^2, is subtracted from the distribution obtained from signal candidates in the $3.06 < m < 3.12$ GeV/c^2 mass region. Because of different selection and different background sources, this is done separately for e^+e^- and $\mu^+\mu^-$ modes. Luminosity scaled Monte Carlo prediction of the ISR contribution (which is the main background source in this analysis) is overlaid on data. All quantities are plotted after all other selection criteria have been applied. Generic $B\overline{B}$ and $c\bar{c}$ distributions, without any selection, are shown for comparison.

To reduce $e^+e^-e^+e^-$ background from radiative Bhabhas with the photon converting to e^+e^-, we tighten the selection by requiring at least 5 ChargedTracks within fiducial volume in events with a reconstructed $J/\psi \to e^+e^-$. This clearly biases the electron distribution shown in Figure 4.23.

Distributions of the total energy detected in fiducial volume (Figure 4.24) show that the cut at 5 GeV/c^2 is effective in removing the ISR. However, a discrepancy in the lowest energy bin indicates that the amount of background passing the selection is underestimated in Monte Carlo. All J/ψ candidates in this energy region are in the backward direction, with the center of mass production angle above $\approx 130°$. This is consistent with the ISR topology, where the photon often escapes through the beam pipe. The observed difference is caused by the low amount of material assumed in the simulation, particularly in the forward direction. ISR photons in data are thus more likely to convert and produce a number of tracks required by event selection. Thus, we correct the Monte Carlo estimate of the ISR background contribution to achieve agreement with the data. The e^+e^- component is increased by 78%, and the $\mu^+\mu^-$ by 53%. The effect on the measured cross-section is minor because the ISR background, after the scaling, equals only 7% of the total signal.

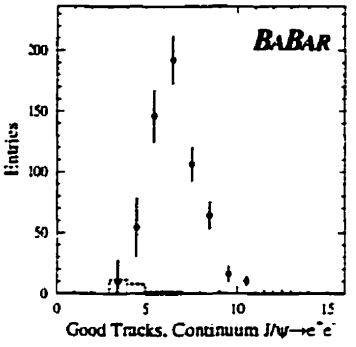

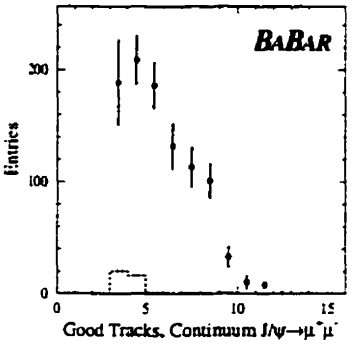

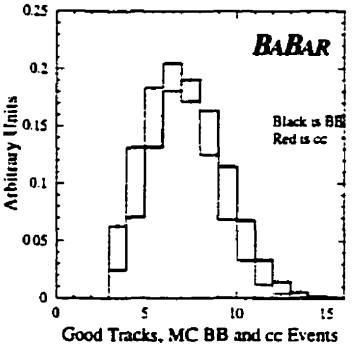

Figure 4.23: Number of GoodTracksLoose in the sideband subtracted e^+e^- sample (top) $\mu^+\mu^-$ sample (middle) and in generic Monte Carlo (bottom). Overlaid histograms are luminosity scaled ISR Monte Carlo.

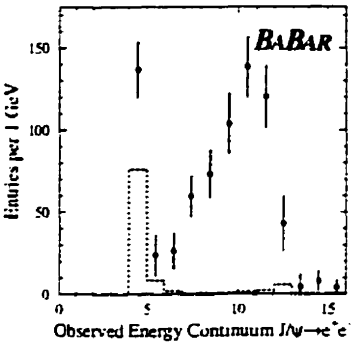

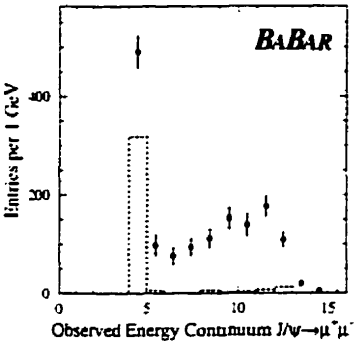

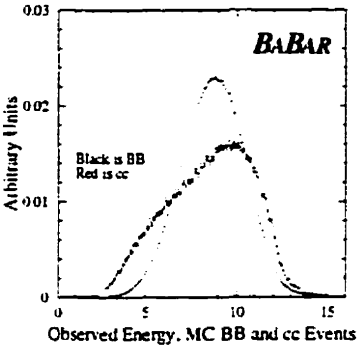

Figure 4.24: Total energy in the fiducial volume in the sideband subtracted e^+e^- sample (top) $\mu^+\mu^-$ sample (middle) and in generic Monte Carlo (bottom). Overlaid histograms are luminosity scaled ISR Monte Carlo.

Distributions of the ratio of second to zeroth Fox-Wolfram moment ($R2All$), calculated from combined list of charged and neutral candidates, are shown in Figure 4.25. As signal events reside at low R2 values and the ISR background is predominantly at high values we use $R2All < 0.5$ as our final event selection criterion. In all cases ISR background almost completely saturates the sideband subtracted R2 distribution above the selected cut value of 0.5. There is a significant fraction of Bhabha events in the signal mass region, as indicated by the high content in the upper R2 region present in the electron channel but not in the muon channel. These are all removed by sideband subtraction. R2 distributions in the signal and sideband regions are not quite the same, as subtracted histograms show that sideband candidates tend to slightly higher R2 values. The effect of the 5 charged tracks requirement on the ISR background is studied by adding the cut to the muon mode as well. As expected, a significant reduction in ISR is observed.

4.10.2 J/ψ Yields

Signal plots are shown in Figure 4.26. The yields extracted from the fits, total efficiency (a product of the event efficiency, complete reconstruction efficiency and the $J/\psi \to \ell^+\ell^-$ branching fraction) and the numbers of produced J/ψ mesons for the four categories are listed in Table 4.21. Calculation of reconstruction efficiencies is performed in Section 4.10.5.

4.10.3 Backgrounds

The first background source we study is the initial state radiation. There are potential contributions from several radiative processes: $e^+e^- \to \gamma\psi(2S) \to \pi^+\pi^- J/\psi$, $e^+e^- \to \gamma J/\psi$, $e^+e^- \to \gamma\Upsilon(1S)$, $e^+e^- \to \gamma\Upsilon(2S)$ and $e^+e^- \to \gamma\Upsilon(3S)$.

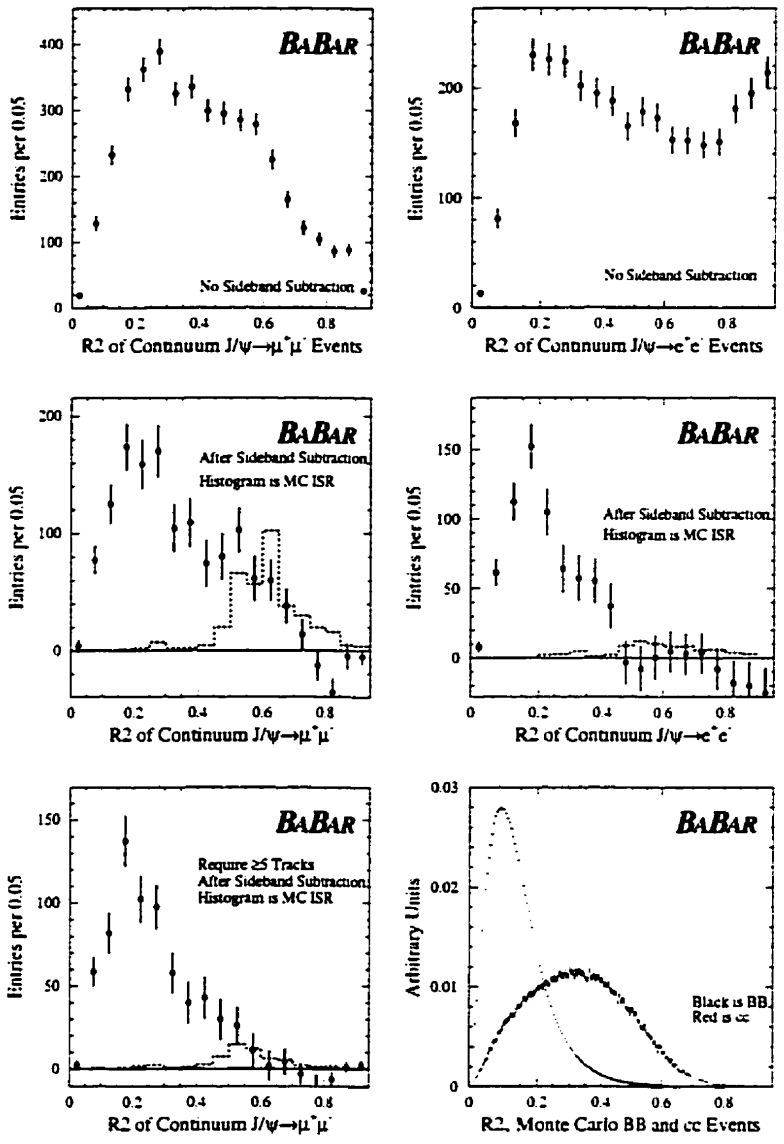

Figure 4.25: R2 distributions for signal events (top row). sideband subtracted events (middle row). sideband subtracted $J/\psi \to \mu^+\mu^-$ with the additional 5 charged track cut (bottom left) and for generic MC (bottom right). Overlaid histograms are luminosity scaled ISR Monte Carlo.

Based on Monte Carlo sample equivalent to 61 fb^{-1} of integrated luminosity. we estimate the contribution from the ISR production of $\psi(2S)$ at 64 ± 9 in the

Table 4.21: $J/\psi \to e^+e^-$ and $J/\psi \to \mu^+\mu^-$ yields of various fits. Bottom part of the table contains yields used for efficiency calculations. $\Upsilon(4S)$ denotes data on and off-resonance. N_t refers to the number of charged tracks in fiducial volume.

mode	$\Upsilon(4S)$	p^* cut	N_t cut	$N_{J/\psi}$
e^+e^-	on	> 2	≥ 5	799 ± 62
$\mu^+\mu^-$	on	> 2	–	879 ± 52
e^+e^-	off	–	≥ 5	121 ± 26
$\mu^+\mu^-$	off	–	–	156 ± 25
e^+e^-	off	> 2	≥ 5	115 ± 21
e^+e^-	off	–	< 5	68 ± 54
e^+e^-	on	> 2	< 5	449 ± 140
$\mu^+\mu^-$	off	> 2	–	88 ± 16
$\mu^+\mu^-$	off	–	≥ 5	103 ± 20
$\mu^+\mu^-$	off	–	< 5	52 ± 14
$\mu^+\mu^-$	on	> 2	≥ 5	563 ± 38
$\mu^+\mu^-$	on	> 2	< 5	319 ± 25

$\mu^+\mu^-$ mode and 71 ± 10 in the e^+e^- mode for the full Run1 sample. Expected number of ISR events is subtracted from the appropriate $p^* - \cos\theta^*$ bins, as per Monte Carlo prediction of the ISR J/ψ distributions. ISR background lies almost exclusively in the highest p^* bin. $\cos\theta^*$ distribution for electrons is enhanced at extreme values. This is expected as the ISR photon must convert into e^+e^- to pass the 5 track criterion, and there is more detector material in the high $|\cos\theta^*|$ region. Note that the photon direction is anti-correlated with the J/ψ direction. Studying direct ISR J/ψ production Monte Carlo shows a negligible contribution to the backgrounds from this mode. On the sample comparable to Run 1 we see one $J/\psi \to e^+e^-$ and zero $J/\psi \to \mu^+\mu^-$ events passing the selection.

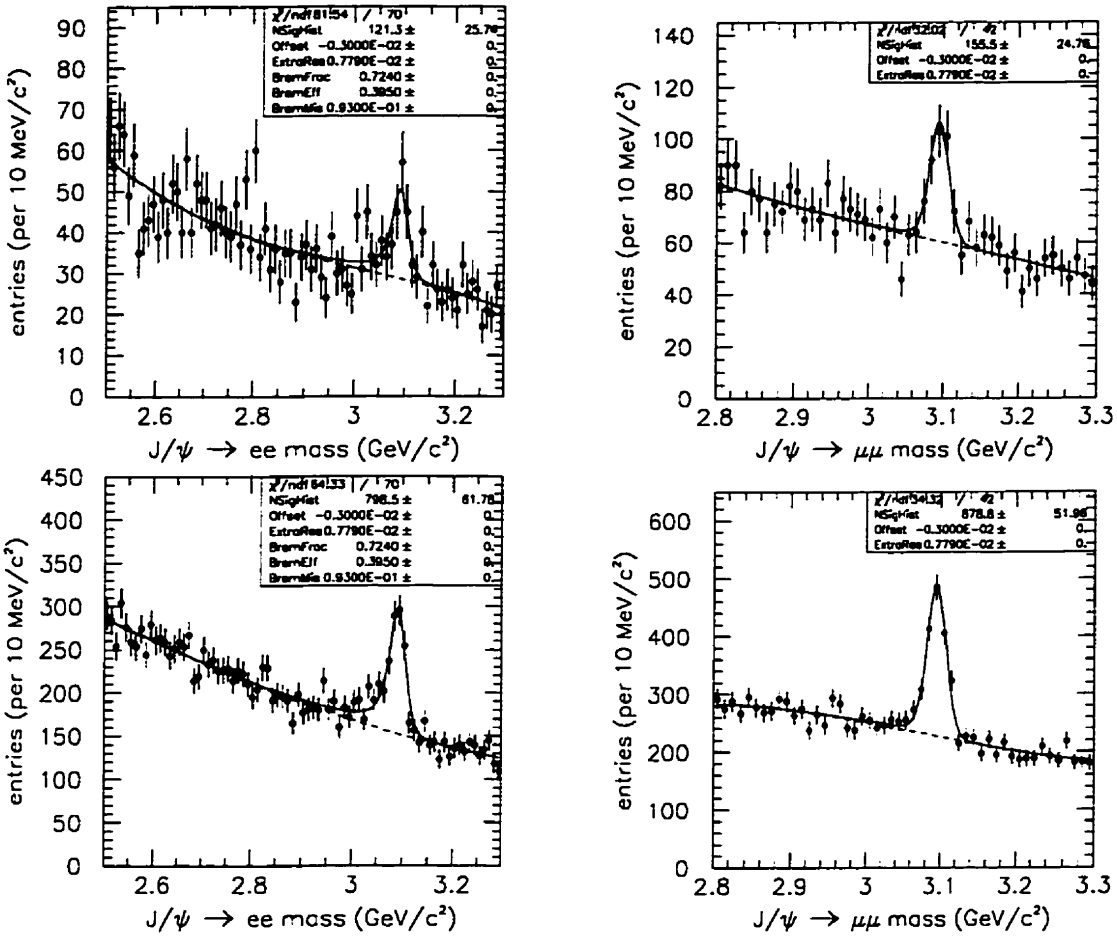

Figure 4.26: Inclusive J/ψ yields in the off-resonance data (top) and in the on-resonance data with p^* >2.0 GeV/c (bottom). Clean signal is observed in both dielectron spectra (left) and dimuon spectra (right).

Starting with the calculation of the cross-sections for ISR production of $\Upsilon(1S)$ (19 pb), $\Upsilon(2S)$ (14 pb) and $\Upsilon(3S)$ (30 pb) and using the branching fractions for their decays into final states containing a J/ψ, we estimate background levels, for the full Run 1, of ≈ 4 events from $\Upsilon(1S)$, < 12 events from $\Upsilon(2S)$ and < 26 events from $\Upsilon(3S)$. Cascading of higher $b\bar{b}$ resonances to $\Upsilon(1S)$, as well as $J/\psi \to \ell^+\ell^-$ branching fraction and reconstruction efficiency are taken into account. The last two numbers are estimates based on the upper limit for the inclusive rate of

$\Upsilon(2S) \to J/\psi$. As the only well determined background is negligible, we do not subtract it from the signal.

Using a recent CLEO measurement of two photon width of χ_{c2}, we estimate that roughly 1100 $\gamma\gamma \to \chi_{c2} \to \gamma J/\psi \to \gamma \ell^+ \ell^-$ events are produced in *BABAR* Run 1. The topology of these events is similar to that of direct ISR J/ψ production. Hence the acceptance should also be similar. However, the cross-section is much smaller, making this process a negligible background source.

4.10.4 Event Selection Efficiency

Our continuum Monte Carlo does not include J/ψ production. So the efficiency of a modified B counting procedure has been estimated using generic $B\overline{B}$ and $c\bar{c}$ events. The efficiency of all cuts but the R2 is 0.833 for $c\bar{c}$ events and 0.960 for $B\overline{B}$ events. We average the two values and assign a systematic error equal to half the difference to obtain: 0.896 ± 0.064. The efficiency of the R2 cut is estimated from the $B\overline{B}$ events only, which closely resemble the R2 distribution of the signal events. The efficiency of this cut is 0.996. This yields the total efficiency of the event selection of 0.892 ± 0.064.

The five charged track requirement significantly reduces background in the $J/\psi \to e^+e^-$ events. The presence of a high center of mass J/ψ candidate decreases the energy available for creation of other particles. Therefore, we cannot evaluate the efficiency of 5 charged tracks cut on generic $c\bar{c}$ Monte Carlo sample, which does not include J/ψ production. We divide the events with a reconstructed J/ψ into two statistically independent samples, the events passing the cut and the events failing the cut. Two mass distributions are fit to extract the yields. These are listed in Table 4.21. The efficiency is calculated as: $\epsilon_{\mathrm{nChgTrk}} = N_{\mathrm{nChgTrk}\geq 5}/(N_{\mathrm{nChgTrk}<5} + N_{\mathrm{nChgTrk}\geq 5})$. Errors on two yields are independent and

their propagation is trivial. Cut efficiencies are calculated independently for the off-resonance sample and for the $p^* > 2$ GeV/c on-resonance sample and then combined according to the statistical weight. Although the cut is applied only to the $J/\psi \to e^+e^-$ candidates, the efficiency was studied for both electrons and muons. As the results for different lepton channels agree within the statistical errors, they are combined to decrease the systematic error on the selection efficiency. Measured efficiencies are $\epsilon_{\text{off res}} = 69 \pm 8\%$ and $\epsilon_{\text{on res},p^*>2} = 67 \pm 4\%$, yielding a weighted average value of $67.3 \pm 3.8\%$. Note that this efficiency is calculated after the ISR background is properly subtracted. The subtraction is done according to the fraction of ISR events with fewer than 5 charged tracks, as presented in Figure 4.23.

4.10.5 Reconstruction Efficiencies

$N^{\epsilon}_{J/\psi}$, the number of J/ψ corrected for the MC reconstruction efficiency, is calculated independently for electron and muon modes. To properly account for the efficiency variation with p^* and $\cos\theta^*$, including the correlations, we break the data sample in 15 bins, five in $\cos\theta^*$ and three in p^*, producing a two dimensional distribution of yields. Invariant mass histograms (for e^+e^- and $\mu^+\mu^-$) of candidates in each bin are fit to extract the signal. Combining the yields in 15 bins gives results fully consistent with those obtained by single fits. Summing over the bins yields 1041 ± 58 $\mu^+\mu^-$ events and 929 ± 67 e^+e^- events in the combined on and off-resonance sample. Adding the entries from the first four rows of Table 4.21 results in 1035 ± 58 muon and 920 ± 67 electron events. Reconstruction efficiencies for each of the 15 bins are extracted from single particle J/ψ Monte Carlo. Results are presented in Table 4.22.

Additional efficiency correction (including the common corrections) of each signal

Table 4.22: Monte Carlo reconstruction efficiencies and fit results for the 15 p^*-$\cos\theta^*$ bins. Ranges for each bin are marked in the top row (p^*) and first two columns ($\cos\theta^*$) of each sub table, with the lower bound followed by the upper bound. Within the table body, each value is followed by its error. $p^* < 2\,\mathrm{GeV}/c$ yields are from off-resonance data only, scaled up (by a factor of 8.99) the total luminosity. ISR backgrounds are subtracted from the appropriate bins, according to Monte Carlo distributions.

Muons	**Rows are cos(θ*) bins**		**Columns are p* bins**					
			0.0	**2.0**	**2.0**	**3.5**	**3.5**	**5.0**
efficiencies	**0.6**	**1.0**	0.486	0.016	0.294	0.017	0.201	0.027
	0.2	**0.6**	0.537	0.016	0.446	0.019	0.466	0.035
	-0.2	**0.2**	0.533	0.016	0.521	0.020	0.530	0.035
	-0.6	**-0.2**	0.545	0.017	0.563	0.019	0.591	0.032
	-1.0	**-0.6**	0.551	0.017	0.458	0.019	0.442	0.032
Combined On+Off resonance yields	**0.6**	**1.0**	35	63	133	20	29	10
	0.2	**0.6**	108	72	96	19	50	10
	-0.2	**0.2**	198	81	105	20	55	10
	-0.6	**-0.2**	90	72	116	22	73	12
	-1.0	**-0.6**	162	81	137	24	117	17

Electrons	**Rows are cos(θ*) bins**		**Columns are p* bins**					
			0.0	**2.0**	**2.0**	**3.5**	**3.5**	**5.0**
efficiencies	**0.6**	**1.0**	0.588	0.017	0.415	0.019	0.319	0.031
	0.2	**0.6**	0.680	0.016	0.617	0.019	0.606	0.035
	-0.2	**0.2**	0.705	0.015	0.725	0.017	0.640	0.034
	-0.6	**-0.2**	0.707	0.015	0.727	0.017	0.654	0.032
	-1.0	**-0.6**	0.702	0.015	0.627	0.019	0.528	0.035
Combined On+Off resonance yields	**0.6**	**1.0**	0	63	110	25	44	15
	0.2	**0.6**	52	63	83	22	41	14
	-0.2	**0.2**	45	63	135	23	32	13
	-0.6	**-0.2**	35	63	139	24	61	15
	-1.0	**-0.6**	-1	9	179	28	24	21

mode, $\epsilon_{J/\psi}$, has following components:

$$\epsilon_{J/\psi} = \epsilon_{PID} \cdot \epsilon_{T}, \tag{4.34}$$

where

- ϵ_{PID} is the particle identification correction of 0.989 (1.4% systematic) for $J/\psi \to \mu^+\mu^-$ and 0.959 (1.8% systematic) for $J/\psi \to e^+e^-$ corrects for differ-

ences between particle killing tables and efficiencies observed in hadronic events (Section 4.5);

- ϵ_T is the tracking efficiency correction calculated from the tables provided by the tracking group, its value is 0.975, with a 2.4% systematic error.

4.10.6 Production Cross-Section

The cross-section for the production of J/ψ mesons in the continuum is calculated from both the e^+e^- and $\mu^+\mu^-$ final states from the off-resonance sample and the on-resonance sample with $p^* > 2$ GeV/c using:

$$\sigma_{e^+e^-\to J/\psi X} = N^{\epsilon}_{J/\psi}/\epsilon_E \cdot \epsilon_{J/\psi} \cdot \mathcal{B}_{\ell^+\ell^-} \cdot \mathcal{L}, \tag{4.35}$$

where

- $N^{\epsilon}_{J/\psi}$ is the number of reconstructed mesons found by the fits, corrected for MC reconstruction efficiency;
- ϵ_E is the probability of a continuum event that contains a J/ψ meson to satisfy the event selection criteria;
- $\epsilon_{J/\psi}$ is the correction to the MC reconstruction efficiency, as discussed in section 4.10.5;
- $\mathcal{B}_{\ell^+\ell^-}$ is the average of the $J/\psi \to e^+e^-$ and $J/\psi \to \mu^+\mu^-$ branching fractions;
- $\mathcal{L}$ is the integrated luminosity. This study uses 2.59 fb^{-1} of off-resonance data and 20.70 fb^{-1}of on-resonance data. Systematic error on luminosity measurement is 1.5%.

As the J/ψ production mechanism and the background sources are the same, on and off-resonance samples are added. Only the off-resonance sample is available in

the $p^* < 2$ GeV/c region, so it is scaled up to the total luminosity of 23.29 fb^{-1}. The cross-sections measured in the two final states are combined according to the method described in Section 4.7.1. Again, particular care is taken to isolate common systematic errors and avoid double counting them. This calculation is presented in Table 4.23.

Details of the cross-section calculation for the J/ψ production in the continuum is presented in Table 4.23.

Combining the efficiencies discussed in previous sections with the signal yields we calculate two statistically independent cross-section measurements, their statistical errors, uncorrelated systematic errors and common systematic errors. Statistical errors in either mode dominate the uncorrelated errors. Leading source of systematic uncertainty is the error on events efficiency, common to both lepton modes. Combining the measurements, which are consistent within the errors, we obtain the following J/ψ production cross-section:

$$\sigma_{e^+e^- \to J/\psi} = (2.47 \pm 0.21 \pm 0.20) \text{ pb}, \tag{4.36}$$

where the first error is statistical (8.4%) and the second error is systematic (8.3%). This cross-section is consistent with the production mechanism dominated by color octet production, as calculated in reference [Sch99].

4.10.7 Signal Properties

Center of mass momentum distribution, center of mass production angle distribution and the polarization of the observed J/ψ mesons are studied in this section.

Table 4.23: Summary of the calculation of the J/ψ production cross-section in the continuum.

J/ψ Cross section in Continuum		Electrons					Muons					Common
		Value	Stat error	%	Sys error	%	Value	Stat error	%	Sys error	%	Sys %
B.F.	J/ψ to leptons BF average	0.059					0.059					1.2
eff-event	event selection efficiency	0.892					0.892					7.2
corr-T	Tracking correction	0.975					0.975					2.4
corr-PID	PID correction	0.959				1.8	0.989				1.4	
eff-mass	mass window correction for ee mode	0.986				0.7						
eff-nChgTrk	efficiency of nChgTrk>4 cut for ee mode	0.673				5.6						
eff-total	*total*	*0.033*				*5.9*	*0.051*				*1.4*	*7.7*
N-eff-J/ψ	efficiency corrected and luminosity scaled	1644	225	13.7		0.8	3224	342	10.6		1.0	
N-J/ψ-0	Produced	50337	6903	13.7			63499	6729	10.6			
L-on+off	Total luminosity	23,290					23,290					1.5
σ	*Cross section*	*2.16*	*0.30*	*13.7*	*0.13*	*6.0*	*2.73*	*0.29*	*10.6*	*0.05*	*1.7*	*7.8*

Ratio of μμ and ee Cross sections:

	2.16	0.32	15.0 comb. ee err		2.73	0.29	10.7 comb. μμ error
ratio μμ/ee	**1.26**	**0.23**	**18.4 combined error**				

Combined ee and μμ Cross sections:

combined B.F.	2.4720	0.2170	8.8 combined		
statistical part of combined error		0.2069	8.4		
systematics part of combined error		0.0656	2.7		
total systematic error		0.2043	8.3	significance	
Final Cross Section	**2.47**	**0.21**	**8.4**	**0.20**	**8.3**	**8.5 σ**

p^* Distribution

Reconstruction efficiency for J/ψ mesons decreases with increasing p^*. Investigating different components shows that mass efficiency, tracking efficiency and PID efficiency do not change with p^*. J/ψ acceptance decreases in both modes because leptons from low p^* candidates have high angular correlation. Given a lepton in the angular acceptance, it is likely that the other lepton will be in the acceptance as well. This is not true for high p^* J/ψ mesons, thus resulting in a drop in efficiency as a function of the CM momentum. Event efficiency shows a slight decrease in $J/\psi \to e^+e^-$ mode only. This is due to the 5 charged tracks cut, as increasing J/ψ p^* leaves less energy to produce charged tracks. Variation of the reconstruction efficiency with p^* is shown in Figure 4.27.

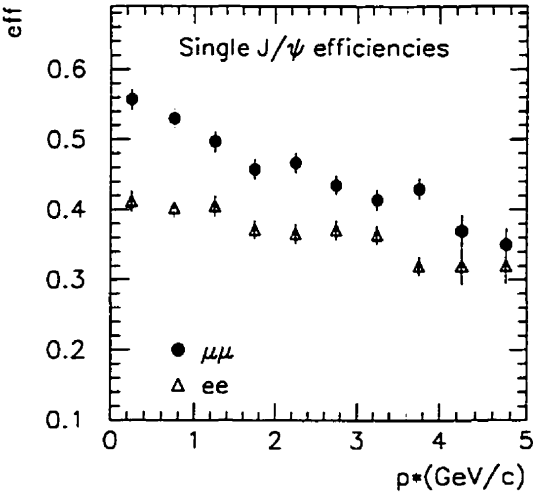

Figure 4.27: J/ψ reconstruction efficiencies for e^+e^- (triangle) and $\mu^+\mu^-$ (dots) modes, calculated from single J/ψ Monte Carlo and corrected for tracking efficiency, PID efficiency, mass efficiency and efficiency of the 5 charged tracks requirement.

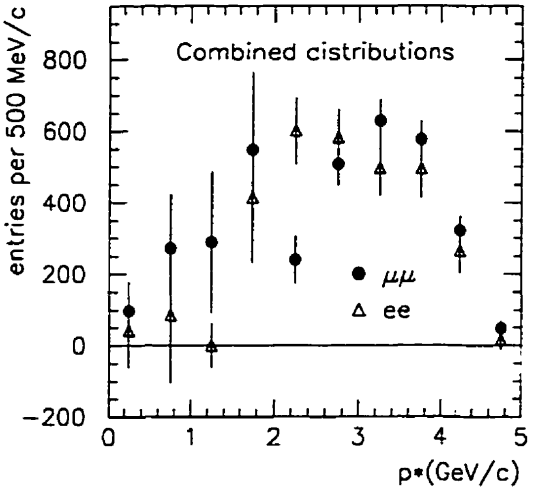

Figure 4.28: Center of mass momentum distribution of $J/\psi \to e^+e^-$ candidates (triangles) and $J/\psi \to \mu^+\mu^-$ candidates (dots). Note that e^+e^- and $\mu^+\mu^-$ yields are consistent, indicating that calculated reconstruction efficiencies are sensible.

Reconstruction efficiency is calculated from the sample of single J/ψ Monte Carlo events. Flat distributions of the center of mass momentum (p^*) and cosine of the center of mass production angle ($\cos\theta^*$) are generated. At the present time only J/ψ with $p^* < 4$ GeV/c are available. Efficiency in the last two bins (Figure 4.27) was extrapolated from the lower bins. 9.9% of the efficiency corrected yield falls in those two p^* bins. Monte Carlo efficiencies are corrected for known differences with respect to data (tracking, mass efficiency and PID). Efficiency of the additional ($N_{\mathrm{ChgFid}} \geq 5$) requirement for electron events, as discussed in Section 4.10.4, is 67.3%, with a 5.6% systematic uncertainty.

J/ψ candidates in both samples are divided in 500 MeV/c bins in p^* and mass distributions of the candidates in each bin are fit to extract the number of reconstructed candidates in a given range. The numbers of produced J/ψ per p^* range are obtained by dividing individual yields by the reconstruction efficiency appropriate for that bin. Entries in the $p^* < 2$ GeV/c range are from off-resonance data only, scaled up to the full luminosity. High momentum range includes the off-resonance and the on-resonance samples and thus has much smaller statistical errors. Center of mass momentum distribution of the J/ψ candidates is shown in Figure 4.28. Reasonable agreement between e^+e^- and $\mu^+\mu^-$ yields increases our confidence in the calculated efficiencies as a function of p^*. The excess of muons over electrons is on a 10% level, consistent with the cross-section calculations. p^* distribution verifies that direct initial state radiation production of the J/ψ ($e^+e^- \rightarrow \gamma J/\psi$) is not a significant source of background. These (ISR) events have a J/ψ p^* distribution strongly peaking at ≈ 4.5 GeV/c. We observe only a weak signal in the last momentum bin, slightly under 1% of the total yield, indicating an absence of considerable direct J/ψ ISR background.

J/ψ Polarization

Applying the method of Section 4.9.2 to continuum data we obtain $A = -0.730 \pm 0.093$ for the combined on and off-resonance sample. (Figure 4.29.)

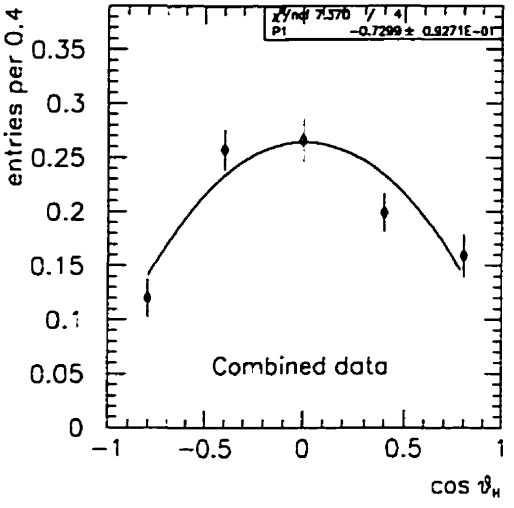

Figure 4.29: Helicity distribution and the fit used to extract the J/ψ polarization for the combined on and off-resonance data.

θ^* Distribution

J/ψ reconstruction efficiency as a function of the production angle (measured in the center of mass) is obtained from single particle J/ψ Monte Carlo and then corrected for tracking, PID, mass efficiency and the 5 charged tracks efficiency. Independent values are calculated for the J/ψ with center of mass momentum below 3.5 GeV/c and for the J/ψ with energy above 3.5 GeV/c. (Figure 4.30.) Electron and muon distributions are divided by the efficiency, normalized and combined. Estimated ISR background (Section 4.10.3) has been subtracted from the appropriate $\cos\theta^*$ bins. On and off-resonance samples are merged and a

single fit to the distribution of Equation 4.33, where $u = \cos\theta^*$, is performed (Figure 4.31). The extracted value of the coefficient is $A = 0.37 \pm 0.22$.

To test the NRQCD predictions versus the colour singlet model, data is divided into two center of mass momentum (p^*) bins so that center of mass energy dependence of A can be observed. As indicated in Chapter 2, the color-singlet model predicts $A \approx -0.84$, where adding the color-octet production changes the calculated value to $A \geq +0.62$. For the high energy region, $p^* > 3.5$ GeV/c, we obtain $A = 1.37 \pm 0.60$. Positive value of A indicates that the color-octet production is the dominant process.

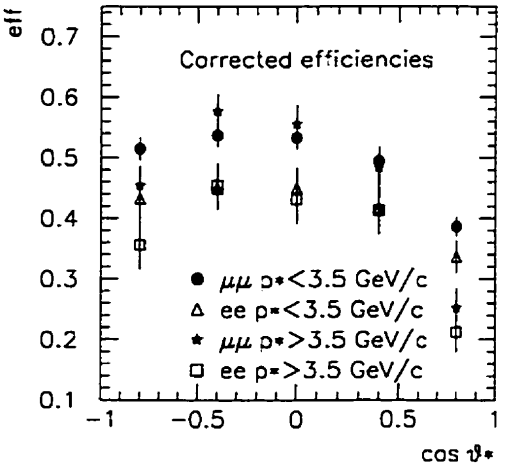

Figure 4.30: J/ψ reconstruction efficiencies for e^+e^- (triangle) and $\mu^+\mu^-$ (dot) modes in the low p^* range, and for e^+e^- (square) and $\mu^+\mu^-$ (star) modes in the high p^* range, calculated from single J/ψ Monte Carlo and corrected for tracking efficiency, PID efficiency, mass efficiency and efficiency of the 5 charged tracks requirement.

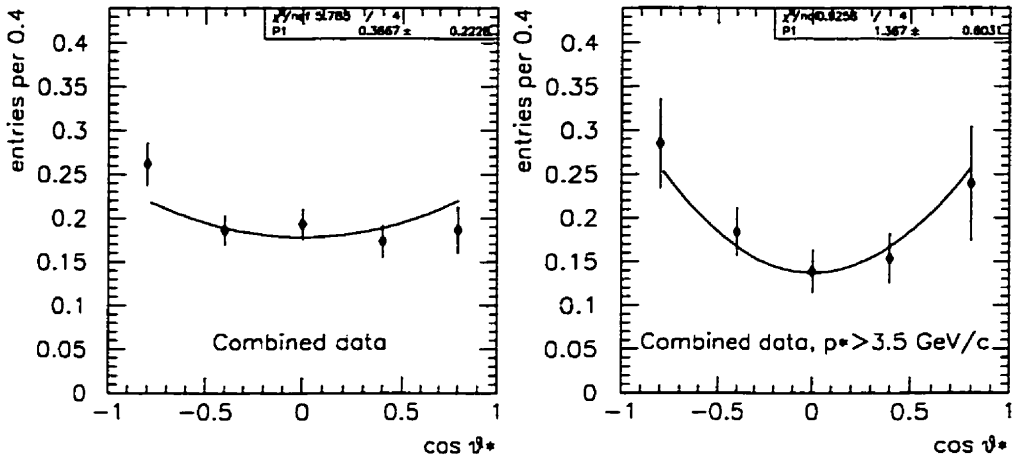

Figure 4.31: Center of mass production angle distribution of $J/\psi \to e^+e^-$ and $J/\psi \to \mu^+\mu^-$ candidates in the full p^* region (left) and the $p^* > 3.5$ GeV/c region (right). Off-resonance and on-resonance $p^* > 2$ GeV/c samples are combined.

4.11 Limit on the inclusive J/ψ decays of $\Upsilon(4S)$

An early measurement by the CLEO experiment, based on 212 pb^{-1} of on-resonance data and 102 pb^{-1} of off-resonance data, claims an observation of inclusive $\Upsilon(4S) \to J/\psi + X$ production via non-$B\overline{B}$ channels [A$^+$90]. Using a method similar to one presented in the previous section, CLEO observed an excess production of J/ψ candidates in the on-resonance sample with respect to the off-resonance sample. They attributed the difference to the non-$B\overline{B}$ decays of the $\Upsilon(4S)$ and calculated a branching fraction of $\mathcal{B}_{\Upsilon(4S)\to\psi X} = (0.22 \pm 0.06 \pm 0.04)$ % (a 3σ significance); for ψ momentum above 2 GeV/c.

Using a 75 times larger data sample we observe no excess in the production of $p^* > 2$ GeV/c mesons on-resonance with respect to off-resonance. On-resonance $p^* > 2$ GeV/c sample contains 799 ± 62 $J/\psi \to e^+e^-$ and 879 ± 52 $J/\psi \to \mu^+\mu^-$. Fitting the off-resonance sample *with* the $p^* > 2$ GeV/c cut yields 115 ± 21 $J/\psi \to e^+e^-$ candidates and 88 ± 16 $J/\psi \to \mu^+\mu^-$ candidates. Subtracting the luminosity scaled

off-resonance yields from the on-resonance yields we obtain a number consistent with zero, -120 ± 179 e^+e^- events and 176 ± 138 $\mu^+\mu^-$ events. Thus we see no evidence of the non-$B\overline{B}$ decays of the $\Upsilon(4S)$ containing J/ψ mesons with a center of mass momentum above 2 GeV/c. Average efficiencies, assuming flat p^* and $\cos\theta^*$ distributions, are used to convert the number of reconstructed J/ψ into the number of produced J/ψ. We calculate a 90 % confidence upper limit by the method defined in Section 4.7.4. Details are presented in Table 4.24. The

Table 4.24: Summary of the calculation of the $\Upsilon(4S) \to J/\psi$, $p^*_{J/\psi} > 2.0$ GeV/c upper limit.

Upsilon(4S) to J/ψ upper limit		**Electrons**			Sys		**Muons**			Sys	
		Value	Stat error	%	error	%	Value	Stat error	%	error	%
N-J/ψ-On	On resonance, p*>2.0	799	62			0.8	879	52			1.0
N-J/ψ-Off	Off resonance, p*>2.0	115	21			0.8	88	16			1.0
L-on / L-off	luminosity ratio	7.99					7.99				
N-J/y-On-Off	On-Off, p*>2, reconstructed	-120	179				176	138			
eff	total efficiency	0.0197				5.9	0.0230				1.4
N-J/y-0-On-Off	On-Off, p*>2, produced	-6086	9073	149.0	*368*	6.0	7642	6006	78.6	*150*	2.0

Combined ee and μμ yields:			
combined yield	3462	5011	144.7
common systematic		266	7.7
BB events passing cuts	21260000		
BranchingFraction	0.00016	0.00024	
Final Upper Limit	**0.00051**		

measured upper limit on this branching fraction is:

$$\mathcal{B}_{\Upsilon(4S)\to J/\psi X} < 5.1 \times 10^{-4}, \tag{4.37}$$

for J/ψ with a center of mass momentum above 2 GeV/c.

Chapter 5

Conclusions and Summary

Using the full data sample of *BABAR* Run 1 we performed a comprehensive study of the inclusive charmonium production near the center of mass energies of 10.58 GeV. 23.3 fb^{-1} of integrated luminosity were collected in e^+e^- collisions around the $\Upsilon(4S)$ resonance during the time period between October 1999 and October 2000.

As mentioned in Chapter 2, existing next to leading order theoretical calculations of the inclusive Charmonium branching fractions are uncertain up to a factor of 2 or 3.

The number of reconstructed mesons was obtained from the fits to invariant mass distributions of $\psi \to \ell^+\ell^-$ decays and to mass difference distributions of $\psi(2S) \to \pi^+\pi^- J/\psi$ and $\chi_c \to \gamma J/\psi$, with the J/ψ subsequently decaying into a lepton pair. Continuum contribution was removed by subtracting luminosity weighted off-resonance contribution.

In addition to the branching fractions, we presented center of mass momentum distributions, center of mass production angle distributions and helicity distributions of reconstructed J/ψ mesons.

All of these measurements are in the process of being published in Physical Review Letters and Physical Review D.

5.1 $B \rightarrow$ Charmonium

Several B meson branching fractions were measured using the known number of B pairs produced in the sample. We found no inconsistencies with the current world averages, as compiled by the Particle Data Group [G+00], but we achieved a precision exceeding that of previously existing measurements, and a more stringent 90% confidence level upper limit on the inclusive χ_{c2} production was set:

- $\mathcal{B}_{B\rightarrow J/\psi X} = (1.044 \pm 0.013 \pm 0.035)\%$,
- $\mathcal{B}_{B\rightarrow \psi(2S) X} = (0.274 \pm 0.020 \pm 0.029)\%$,
- $\mathcal{B}_{B\rightarrow \chi_{c1} X} = (0.378 \pm 0.034 \pm 0.026)\%$,
- $\mathcal{B}_{B\rightarrow \chi_{c2} X} < 0.21\%$,

where the first errors are statistical and the second are systematic. (See Table 4.19.)

5.2 $\psi(2S) \rightarrow \ell^+\ell^-$

By equating the number of $\psi(2S)$ mesons produced in $\pi^+\pi^- J/\psi$ and $\ell^+\ell^-$ final states we calculated the $\psi(2S) \rightarrow \ell^+\ell^-$ branching fractions, significantly reducing the existing error [G+00] in the muon mode:

- $\mathcal{B}_{\psi(2S)\rightarrow e^+e^-} = (0.815 \pm 0.090 \pm 0.090)\%$,

- $\mathcal{B}_{\psi(2S)\to\mu^+\mu^-} = (0.700 \pm 0.083 \pm 0.093)\%$,

5.3 Continuum J/ψ Production

We studied J/ψ production in the *continuum* by observing the signal in the off-resonance data, collected 50 MeV below the $\Upsilon(4S)$ resonance, and in the on-resonance data looking at the center of mass momentum range inaccessible to J/ψ coming from B decays. Using the known luminosity of our data, we measured the continuum J/ψ production cross section of:

- $\sigma_{e^+e^-\to J/\psi X} = (2.47 \pm 0.21 \pm 0.20)$ pb,

a value favoring a production mechanism dominated by the color octet contributions.

5.4 $\Upsilon(4S)$ Direct J/ψ Production

In the upper region of the center of mass momentum spectrum, $p^* > 2$ GeV/c, We observed no excess of J/ψ mesons produced in the on-resonance data with respect to the off-resonance data. Therefore, we set a 90% confidence level upper limit on the J/ψ production in direct $\Upsilon(4S)$ decays (that is, not via a $B\overline{B}$ state) at:

- $\mathcal{B}_{\Upsilon(4S)\to J/\psi X} < 5.1 \times 10^{-4}$ (non-$B\overline{B}$).

We also presented center of mass momentum distributions, center of mass production angle distributions and helicity distributions of reconstructed J/ψ mesons.

5.5 Future Inclusive Charmonium Analyses

The *BABAR* data sample is expected to roughly triple in size within the next year, increasing the integrated luminosity to 90-100 fb^{-1}.

A decrease in statistical errors will be sufficient to obtain a significant measurement of the inclusive $B \to \chi_{c2}X$ branching fraction, about $3.8\sigma_{comb}$ given present systematic errors. The understanding of the detector performance gained through the analyses of the Run 1 data, combined with the improvements in the simulation which are underway, will reduce the systematic errors. However, it is hard to perceive a drastic reduction in some of the leading sources of errors, such as tracking, PID or B counting. Therefore, all other inclusive B measurements will be dominated by systematic errors.

It is very likely that, in the near future, a very precise measurement of the $\psi(2S) \to \ell^+\ell^-$ branching fractions will be made by the BES collaboration. The Bejing accelerator has already produced a clean sample of roughly 4 million of $\psi(2S)$ mesons. Similar measurement would be expected from CLEOC, operating as a Charm factory.

The continuum J/ψ production analysis will greatly benefit from increased data sample. A more precise measurement of the production cross-section and the production angle distribution will definitely resolve the issue of colour-singlet and colour-octet contributions. Including the J/ψ production mechanism into the continuum Monte Carlo will enable a more robust analysis of the efficiencies.

Glossary

- AWG - analysis working group
- $\mathcal{B}$ - branching fraction
- *BABAR* - particle detector at SLAC and the name of the collaboration
- $B\overline{B}$ events - events in which a pair of B mesons is created
- $c\bar{c}$ events - events in which a pair of c quarks is created
- Charmonium - any of the $c\bar{c}$ mesons
- CKM - Cabbibo-Kobayashi-Maskawa matrix
- CP - inversion of both C and P
- DCH - drift chamber
- DIRC - detector of internally reflected Čerenkov light
- EMC - electromagnetic calorimeter
- GEANT - detector description and simulation tool written at CERN, Switzerland
- IFR - instrumented flux return
- ISR - initial state radiation

- MINUIT - function minimization and error analysis software written at CERN, Switzerland
- MC - Monte Carlo
- NIM - 'Nuclear Instruments and Methods in Physics Research'
- NRQCD - non-relativistic quantum chromodynamics
- PEP-II - asymmetric e^+e^- storage ring at SLAC
- PDF - probability density function
- PDG - particle data group
- PID - particle identification
- PL - 'Physics Letters'
- PRD - 'Physical Review D'
- PRL - 'Physical Review Letters'
- p^* - center of mass momentum
- QCD - quantum chromodynamics
- SLAC - Stanford Linear Accelerator Center
- SVT - silicon vertex tracker
- θ_H - helicity angle
- θ^* - center of mass production angle

Bibliography

[A+74a] G. S. Abrams et al. *PRL*, 33:1453, 1974.

[A+74b] J.-E. Augustin et al. *PRL*, 33:1406, 1974.

[A+87a] C. Albajar et al. *PL*, B186, 1987.

[A+87b] H. Albrecht et al. *PL*, B192, 1987.

[A+90] J. Alexander et al. *PRL*, 64:2226, 1990.

[A+92] F. Abe et al. *PRL*, 69:3704, 1992.

[A+97a] S. Abachi et al. *PRL*, 79, 1997.

[A+97b] Armstrong et al. *PRD*, 55, 1997.

[A+98] F. Abe et al. *PRL*, 80, 1998.

[A+00] Ambrogliani et al. *PRD*, 62, 2000.

[AWG00a] Electron Identification AWG. Cut-based electron identification. *BABAR* Analysis Document 90, 2000.

[AWG00b] Muon Identification AWG. Muon identification in the *BABAR* experiment. *BABAR* Analysis Document 60, 2000.

[B+01] J. Z. Bai et al. *PRD*, 63, 2001.

[BBL95] G. T. Bodwin, E. Braaten, and G. P. Lepage. *PRD*, 51:1125, 1995.

[BMR99] M. Beneke, F. Maltoni, and I. Z. Rothstein. *PRD*, 59:054003, 1999.

[Bra96] E. Braaten. *PRL*, 76:730, 1996.

[Bur97] C. P. Burgess. A primer on the standard model of elementary particle physics. Course Notes, McGill University, 1997.

[Cab63] N. Cabibbo. *PRL*, 10:531, 1963.

[CCFT64] J. Christenson, J. Cronin, V. Fitch, and R. Turlay. *PRL*, 13:138, 1964.

[CK84] L. L. Chau and W. Y. Keung. *PRL*, 53, 1984.

[CL96] P. Cho and A. K. Leibovich. *PRD*, 54:6690, 1996.

[col99] OPAL collab. *PL*, B384, 199.

[Col95] *BABAR* Collaboration. *BABAR Technical Design Report.* Stanford Linear Accelerator Center, Stanford, California, March 1995.

[Col98] *BABAR* Collaboration. *The BABAR Physics Book.* Stanford Linear Accelerator Center, Stanford, California, October 1998.

[Col00] *BABAR* Collaboration. The first year of the *BABAR* experiment at PEP-II. SLAC-PUB-8539, Contributed to 30th International Conference on High-Energy Physics (ICHEP 2000), Osaka, Japan, 2000.

[Col01a] *BABAR* Collaboration. Draft: A study of time-dependent ***CP***-violating asymmetries in b^0 decays to charmonium final states. *PRD*, 2001.

[Col01b] *BABAR* Collaboration. Draft: The *BABAR* detector. *NIM*, 2001.

[D+85] A. Drescher et al. *NIM A*, 237, 1985.

[Dc+94] P. Abreu DELPHI collab. et al. *PL*, B341, 1994.

[F+83] E. Fernandez et al. *PRL*, 51, 1983.

[F+01] R. Faccini et al. Measurement of exclusive charmonium branching ratios using data from babar's first run. *BABAR* Analysis Document 113, 2001.

[G+00] D. E. Groom et al., editors. *The Review of Particle Physics*. C15. The European Physical Journal, 2000.

[GG74] H. Georgi and S. L. Glashow. *PRL*, 32:438, 1974.

[GM61] Gell-Mann. *The Eightfold Way: A Theory of Strong Interaction Symmetry*. CTSL-20, Caltech, 1961.

[Gri87] D. Griffiths. *Introduction to Elementary Particles*. John Wiley & Sons, Inc., 1987.

[H+75] G. Hanson et al. *PRL*, 35, 1975.

[H+77] S. W. Herb et al. *PRL*, 39, 1977.

[Hea00] C. Hearty. Measurement of the number of $\Upsilon(4S)$ mesons produced in run 1 (b counting). *BABAR* Analysis Document 134, 2000.

[KM73] M. Kobayashi and T. Maskawa. *Prog. Theor. Phys.* 49:652, 1973.

[Lue57] G. Lueders. *Annals Phys.*, 2:1–15, 1957.

[MP99a] M. Milek and P. M. Patel. *NIM A*, 425, 1999.

[MP99b] M. Milek and P. M. Patel. Continuum background suppression using various selectors. *AIP Conference Proceedings*, 488, 1999. Presented at High Energy Physics at the Millennium, Ottawa, 1999.

[Ne'61] Y. Ne'eman. *Nucl. Phys.*, 26:222–229, 1961.

[Odd87] P. Oddone. *in Proceedings of the UCLA Workshop: Linear Collider $B\bar{B}$ Factory Conceptual Design, ed. D. Stork (World Scientific)*, page 243, 1987.

[Ram82] N. F. Ramsey. *Rep. Prog. Phys.*, 45:95, 1982.

[Sak67] A. D. Sakharov. *JETP Letters*, 5:24, 1967.

[Sch99] G. A. Schuler. *Eur. Phys. J.*, 8:273–281, 1999.

[SV97] R. Sinkus and T. Voss. *NIM A*, 391, 1997.

[W+57] C. S. Wu et al. *Phys. Rev.*, 105:1413, 1957.

[Wol83] L. Wolfenstein. *PRL*, 51:1945, 1983.